4-19-2013

A NEW APPROACH TO CHARACTERIZING FRACTURE NETWORKS: AN ANALYSIS OF NATURAL FRACTURES WITHIN THE STILLWELL ANTICLINE, WEST TEXAS

Luciana De la Rocha
Trinity University, ldelaroc@trinity.edu

A NEW APPROACH TO CHARACTERIZING FRACTURE NETWORKS: AN ANALYSIS OF NATURAL FRACTURES WITHIN THE STILLWELL ANTICLINE, WEST TEXAS

Luciana de la Rocha

A departmental senior thesis submitted to the Department of Geosciences at Trinity University.

April 19, 2013

__________________________ __________________________

Thesis Advisor Department Chair

TABLE OF CONTENTS

ACKNOWLEDGMENTS

I am sincerely thankful to my thesis advisor, Dr. Benjamin Surpless, whose excellent guidance, patience and support, from the initial to the final stages of this project, enabled me to complete this research. I would also like to thank Dr. Kathleen Surpless for encouraging me to start this project and for making helpful editorial suggestions as I completed this work.

This research was funded by NSF award # 1220235 and the Murchison Summer Research Fellowship from Trinity University. I would like to give special thanks to Mike Pittman and Travis Smith of the Black Gap Wildlife Management Area for logistical aid and Dr. Julia Gale from the Bureau of Economic Geology and Dr. Diane Saphire for their intellectual support. In addition, special thanks to Rob Reed for his assistance in gathering data on the Scanning Electron Microscope (SEM) at the Bureau of Economic Geology.

I would also like to thanks my friends Lauren Mercado and Nathan Tinker for their support in the field and in the late nights in the Geosciences computer lab.

List of Figures

List of Tables

ABSTRACT

In the past twenty years, the fracture research field has experienced exponential growth, but there is still debate about how to best sample and characterize natural fracture networks. A vast majority of studies lack a comprehensive evaluation of variables that control fracture behavior, and few studies take into account either fracture aperture or observational bias in the characterization of fracture systems. In addition, most fracture research has been limited to either the microscopic or macroscopic scale. I investigated fracture networks at the transition between the micro- and macroscopic scale at the well-exposed Stillwell anticline in west Texas. The excellent cross-sectional exposure of the asymmetric anticline provided the opportunity to analyze fracture systems within a single limestone bed at different structural positions, including the forelimb, the forelimb hinge, the middle limb, the backlimb hinge, and the backlimb. At each structural position, I measured fractures' orientation, fill, morphology, length, and aperture within a rectangular observation area. Because observational bias can strongly affect outcrop data, I used a new multi-step method to account for the unequal probability of encountering fractures based on each fracture's orientation relative to the observation plane and the orientation of each fracture within the rectangular shape of observation area. Based on these relative orientations, I weighted each fracture, assigning an integer-based correction factor. Optical imagery showed that these fracture systems are mostly composed of calcite veins with multiple generations of fracture fill. Statistical data suggest that fracture intensity, aperture, and fracture length data are significantly different at each structural position, and fracture intensity appears to be directly related to strain. In fold hinges, where bed curvature is

greatest, fracture intensities are highest and fracture lengths are lowest. In contrast, in the forelimb, where shear strain is at a maximum, fracture intensity is lowest and fracture lengths are highest. This suggests that fracture initiation and propagation are strongly affected by structural position, which is likely controlled by the how stresses are applied to limestone beds throughout the formation of the fold system. These results demonstrate that analysis of fracture networks at a transitional scale can provide significant insight about fracture systems and their evolution at different positions in a fold system. In many low porosity oil and gas reservoirs, natural fractures control the permeability of the system, so these results might also help predict permeability changes in similar subsurface fold systems.

I. INTRODUCTION

Natural fractures and their geologic characteristics control the hydraulic behavior of both hydrologic and petroleum reservoirs. A better understanding of fracture systems would help optimize the recovery of natural resources from fracture reservoirs (e.g., Hennings et al., 2000). Therefore, it is imperative to develop a reliable detection and characterization model of fracture systems for the quantification of permeability. Fracture network evolution can be affected by lithology, bed thickness, mechanical stratigraphy, proximity to faults, structural position, the presence or absence of interlayer slip, recrystallization, cataclasis and dissolution-reprecipitation processes (e.g., Price, 1959; Stearns, 1968; Stearns and Friedman, 1972; Ladeira and Price, 1981; Nelson, 2001; Naar, 1996; Couples and Lewis, 1998; Underwood et al., 2003; Smart et al., 2009), so developing transferable models for fracture network development has been an ongoing challenge in structural geology.

In the past twenty years, the fracture research field has experienced exponential growth, with many studies focused upon the relationships between fracture intensity, orientation, fill, and length (e.g., Lonergan, 1999; Marrett et al., 1999; Nelson 2001; Casey and Butler, 2004). Most of these studies have been scale-dependent, focusing either on the microscopic or macroscopic scale (e.g., Ortega et al., 2006). Although fracture intensity is one of the key parameters that determine fluid flow in low permeability lithologies (e.g., Ortega et al., 2006; Hooker et al., 2009; Ortega et al., 2010), few studies take into account fracture aperture in their measurements of fracture intensity, a quantity that varies across at least six orders of magnitude in natural systems (Ortega et al., 2006; Hooker et al., 2009;

Marrett, 1996). Since fluid flow is fundamentally controlled by the percentage of void space in a rock, fracture aperture will have a significant and quantifiable effect on permeability.

In addition, there is still debate in the literature about the relationship between fracture intensity and fold development. Many outcrop-based studies support a positive correlation between fracture intensity and layer curvature (e.g., Murray, 1968; Lisle, 1994: Stewart and Podolski, 1998). However, other workers posit that a significant number of factors affect fracture intensity, demonstrating that the positive correlation does not hold true in all cases (e.g., Hennings et al., 2000, Bergbauer, 2007; Keating and Fischer, 2008). In order to perform a comprehensive analysis of fracture systems at different structural positions in a fold system (e.g., forelimb, forelimb hinge, middle limb, backlimb hinge, and backlimb), I have performed statistical analyses that take into account most important factors that affect permeability. A better understanding of fracture intensity at different structural positions would improve the prediction of changes in permeability within a specific reservoir.

Although there have been thousands of studies of fracture systems, there is still no reliable method to collect fracture data in outcrop that can be easily transferred to the subsurface (e.g., Terzaghi, 1965, Palmstrom and Stromme, 1996). Observational sampling bias in outcrop data collection is a problem that can introduce significant error. The likelihood of a fracture intersecting a sampling domain depends on many factors, such as the relative orientation of the fracture with respect to the observational plane, the shape and length of the fracture, and the size and shape of the observational plane (e.g., Palmstrom and Stromme, 1996). In order to accurately calculate fracture intensity, to analyze fracture systems, and to provide accurate analogs for subsurface studies, all outcrop data must be corrected for known sampling biases.

I studied fractures at the macro-microscopic (intermediate) transitional scale within the well-exposed Stillwell anticline, a Laramide-age fold system hypothesized to have formed due to the propagation of an en echelon blind thrust fault system (e.g., Surpless and Quiroz, 2010; Surpless et al., 2012). Previous workers showed that different segments of the fold system preserve geometrically different but well-defined fold geometries related to variations in thrust fault propagation displacements (Surpless and Quiroz, 2010; Surpless et al., 2012). The dissection of the fold by a significant creek system provides easy access to the different structural positions from a geometrically simple segment of the anticline (Fig. 1). This excellent exposure permitted investigation of fractures from a single limestone bed at different structural positions, including the backlimb, middle limb, forelimb, and the hinges between those limbs (Fig. 1), thus providing the opportunity to evaluate fracture characteristics (i.e., intensity, aperture, fill, and length) relative to structural position.

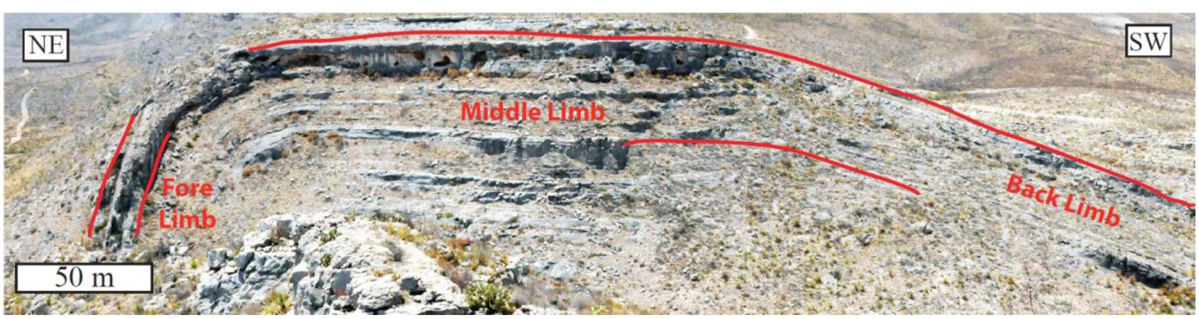

Figure 1. Cross-sectional view of the Stillwell anticline, looking towards the southeast. A creek has dissected the fold, permitting access to limestone beds at all structural positions.

The analysis of fracture systems was guided by several key questions:

1. Can fracture analysis at the intermediate scale provide insights about the evolution of fracture systems in the subsurface?

2. Are there quantifiable relationships between fracture orientation, fracture aperture, fracture length, and fracture intensity?

3. How do fracture characteristics vary at different structural positions within a fold system?

4. Can outcrop observational biases be reduced to the point that the information provided by outcrop studies provides accurate baselines for subsurface analysis?

To answer my research questions, I collected fracture data from nearly identical limestone beds in five different structural positions of the Stillwell anticline, and I collected hand samples from each location for subsequent analysis. For each *in situ* fracture, I measured aperture (width), orientation, morphology, fill, and x-y position (relative to an established position within the bed). I used thin section petrography, optical cathodoluminescence (CL) analysis, and scanning electron microscopy (SEM) elemental detection spectrometry (EDS) and backscattered electron (BSE) imagery to document the fracture systems present. In order to account for potential observational biases, I used a new weighting method to correct the sampled data. I used these data to perform fracture intensity analysis and to complete a range of statistical analyses to obtain information about relationships between fracture variables and the implications of these relationships for fracture network evolution.

II. BACKGROUND

<u>Tectonic Setting</u>

The Stillwell anticline is a northwest-trending, asymmetric fold located along the southeast margin of the Trans-Pecos region of west Texas, to the east of Big Bend National Park (Fig. 2). The anticline was formed during the Laramide Orogeny in the Late Cretaceous - Early Tertiary, but it is likely that previous tectonic events influenced its evolution (Surpless and Quiroz, 2010; Surpless et al., 2012). Figure 3 is a tectono-stratigraphic column that relates regional geologic units to the significant tectonic events that affected the Trans-Pecos region.

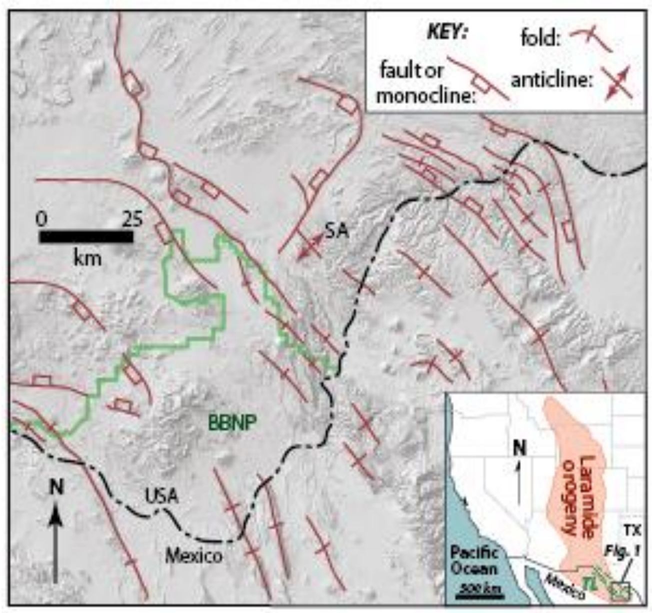

Figure 2. Shaded relief map with major Laramide-age faults and folds of the Big Bend region (in red), with inset (lower right) showing distribution of deformation associated with the Laramide orogeny (red shading, inset) and the approximate boundaries of the Texas Lineament (TL, inset). Big Bend National Park (BBNP) is outlined in green and the Stillwell anticline is labeled SA. For most Laramide age folds, fold type is not differentiated. Distribution of Laramide-age faults and folds modified from Muehlberger and Dickerson (1989). Extent of Laramide orogeny modified from Miller et al. (1992). Approximate boundaries of the Texas Lineament modified from Muehlberger (1980). Figure modified from Surpless and Quiroz (2010).

The major structural trends in the Trans - Pecos region are hypothesized to be the result of the reactivation of pre-existing zones of weakness (e.g., Muehlberger and Dickerson, 1989). These trends, best defined by fault and fold systems of Laramide and younger age, are collectively known as the Texas lineament (Fig. 2; e.g., Muehlberger, 1980). This northwest-trending zone is hypothesized to be controlled by deep structures that initially formed during rifting events in the late Proterozoic (e.g., Muehlberger and Dickerson, 1989; Page et al., 2008). Following early rifting and subsequent marine deposition, the Late Paleozoic Ouachita orogeny resulted in faulting and folding of the deep-water ocean basin rocks of the Trans-Pecos region (e.g., Page et al., 2008). Despite north-directed collision, the structures created by the orogeny formed sub-parallel to the present-day Texas lineament (e.g., Muehlberger and Dickerson, 1989; Page et al., 2008).

In the late Triassic, rifting between the North and South American Plates began to form the Gulf of Mexico (e.g., Muehlberger, 1989; Page et al., 2008). By Cretaceous time, the Trans-Pecos region had become a shallow marine environment, resulting in deposition of both shale and more resistant limestone formations such as the Glen Rose limestone, the Del Carmen limestone, the Sue Peaks Formation, the Santa Elena limestone, the Del Rio claystone, and the Buda limestone (e.g., St. John, 1965; 1966; Moustafa, 1988; Page et al., 2008).

From the Late Cretaceous through the Early Tertiary, the relatively shallow subduction of the Farallon plate under the North American Plate affected much of the Western U.S., including the Trans-Pecos region (e.g., Dickinson, 1981; Muehlberger, 1989; Page et al., 2008). The east-directed compression resulted in the thick skinned Laramide Orogeny (Fig. 2, inset), with deformation characterized by basement-core uplifts of pre-fractured anisotropic basement blocks (e.g., Miller et al., 1992; Liu et al., 2010). In the Trans-Pecos region, this tectonic event formed northwest trending monoclines and anticlines sub parallel to the Texas Lineament and at an oblique angle relative to the maximum stress (Fig. 2; e.g., Moustafa, 1983; 1988; Maler, 1990; Surpless and Quiroz, 2010). Most basement-involved, fault-related anticlines of the Laramide Orogeny are characterized by narrow, steeply-dipping forelimbs and expanded, gently dipping backlimbs (e.g., Stone, 1993), features shared by the Stillwell anticline (St. John, 1965; Moustafa, 1983; 1988; Surpless and Quiroz, 2010).

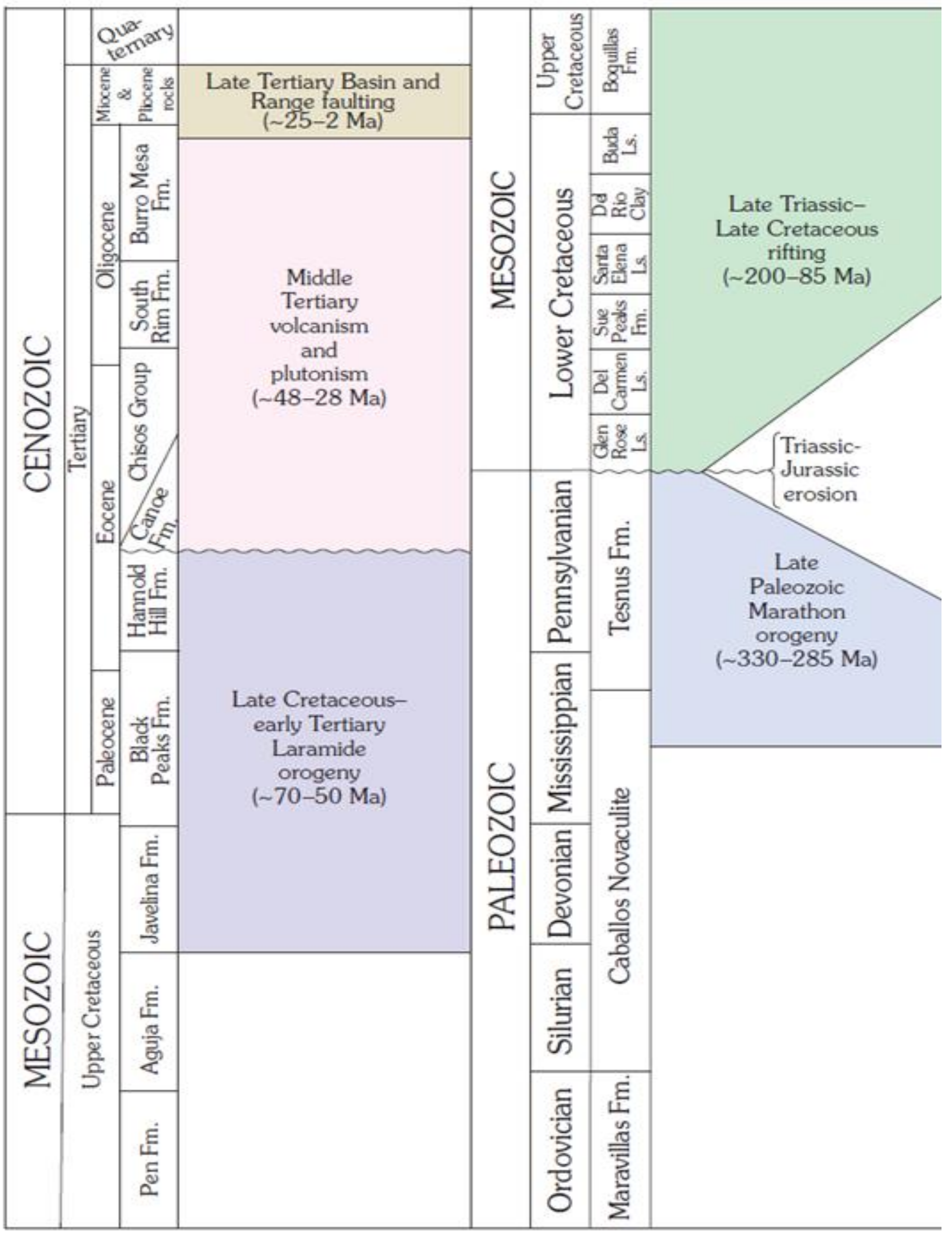

Figure 3. Tectono-stratigraphic column of the Trans-Pecos region. The column relates geologic rock units to the major tectonic events that have affected the region (from Page et al., 2008).

By middle to late Cenozoic time, collision of the North American and South American Plates ceased and Basin and Range extensional faulting affected the Trans-Pecos region (e.g., Page et al., 2008). During this time, the Trans-Pecos region was subject to volcanic and plutonic activity. However, there is no evidence that any post-Laramide tectonic events affected the Stillwell anticline (St. John, 1965; Surpless and Quiroz, 2010; Mays et al., 2012; Surpless et al., 2012).

The Stillwell anticline fold system

The Stillwell anticline is an 8000 m long, 550 m wide and 250 m high asymmetric, northeast-vergent fold best defined by the resistant Cretaceous Santa Elena limestone (St. John, 1965; 1966; Surpless and Quiroz, 2010; Mays et al., 2012). The fold axis trends about N40°W and is divided into a North segment, a South segment and a transition zone that displays three prominent left steps within a 2 km zone between segments (Fig. 4; Surpless and Quiroz, 2010; Mays et al., 2012; Surpless et al., 2012). This map-view fold geometry was most likely created by a shallow, subsurface en echelon thrust fault system, with complex interactions at depth (Mays et al., 2012; Surpless et al., 2012).

Previous studies suggest that the Stillwell anticline is likely a classic fault-propagation fold (Surpless and Quiroz, 2010; Mays et al., 2012; Surpless et al., 2012), with cross-sectional geometries that can be related to stages of ramp-flat fault propagation. Although most locations along the anticline system reveal a shallowly dipping backlimb to the southwest and a steeply dipping forelimb to the northeast (Mays et al., 2012), perhaps the best-exposed cross-sectional view of the system, shown in Figure 1, displays a geometry that includes a backlimb, middle limb, and a forelimb.

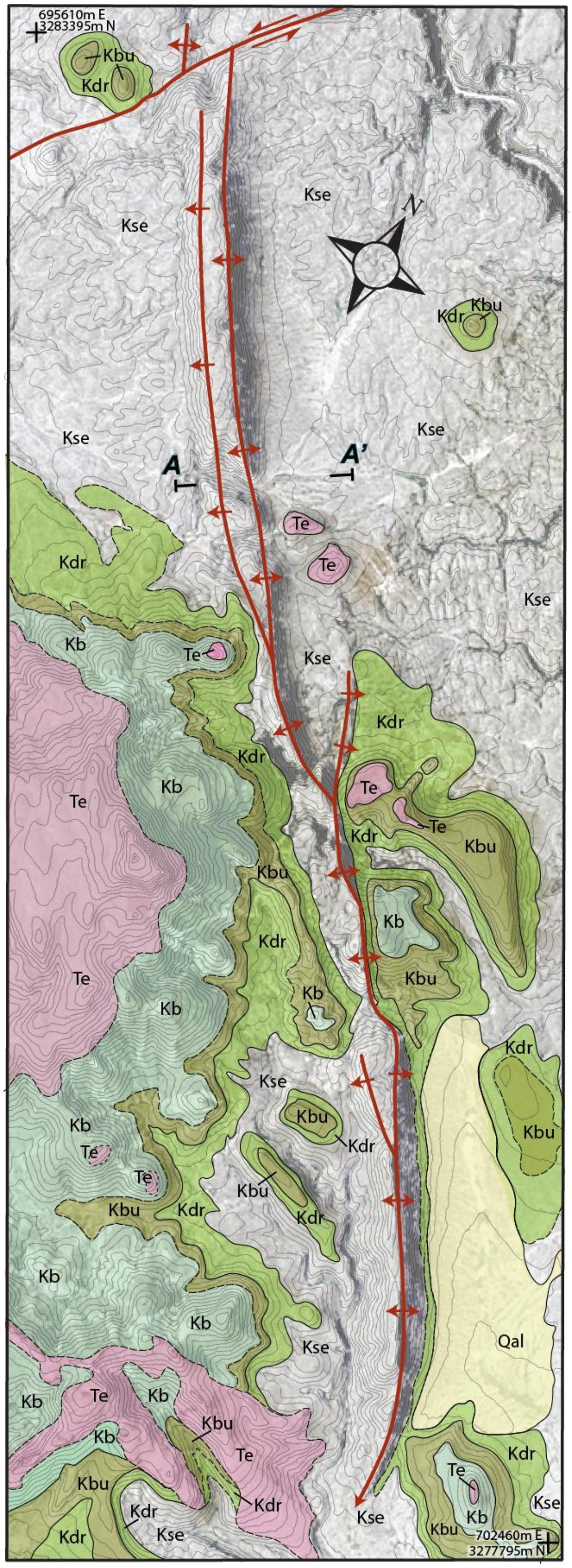

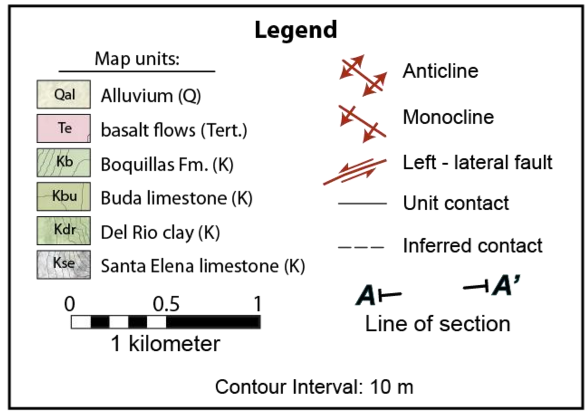

Figure 4. Geologic map of the Stillwell anticline. The northwest trending anticline consists of a north and south segments with a transition zone that displays left en echelon fold axis geometry (Surpless and Quiroz, 2010; Mays et al., 2012).

Kinematic analysis by Mays et al. (2012) indicated a total flat-ramp propagation of approximately 200 meters, with slip accommodated primarily along a decollement within the underlying Sue Peaks Formation that propagated upward to the northeast along a ramp segment within the Santa Elena limestone. The results of this two-dimensional modeling also suggest that the forelimb and adjacent hinge zone of the anticline are the areas of greatest shear strain (Mays et al., 2012). Related to this work, other workers have shown that strain within the anticline is likely accommodated by deformation mechanisms such as ductile thickening, intra-bed faulting, and interlayer slip, in addition to fracturing (Hoin et al., 2012; Surpless et al., 2012), which may have implications for fracture analyses based on structural position.

In the north segment of the Stillwell Anticline, a stream has dissected the fold systems across the A – A' line, providing an excellent cross-sectional view of the Stillwell anticline (Fig. 1). At this location the anticline is asymmetric, with a shallowly-dipping backlimb and a steep forelimb (Surpless and Quiroz, 2010; Mays et al., 2012). Individual limestone beds and mechanical layers can be traced along the entire cross-sectional view. Therefore, this location was subject to many macro-scale structural studies, as well as detailed analysis of the mechanical stratigraphy of the Santa Elena limestone (Mays et al., 2012; Hoin et al., 2012; Surpless et al., 2012; Tinker et al., 2013).

The Santa Elena limestone

The 56 meter thick cross-sectional exposure of the Stillwell anticline is characterized by relatively resistant Santa Elena limestone beds (Tinker et al., 2013). The massive 1-3 meters thick limestone beds interbedded with thinner 1 meter thick shale beds suggest a neritic shallow reef depositional environment (Hoin et al., 2012). Previous studies of the exposed stratigraphy have documented bed thickness, lithology, compressive strength, macroscopic fracture intensity, and joint orientations for each exposed limestone bed (Mercado and Surpless, 2012; Tinker et al., 2013). These workers concluded that a majority of the exposed beds are composed of a light tan to light grey, fine to medium grained limestone and have no significant variation in compressive strength. Figure 5 shows the exposed Santa Elena stratigraphy in the middle limb of the anticline. Tinker et al (2013) suggest that mechanical units with thinner average bed thickness are less resistant to weathering. However, thinner beds display significantly greater fracture intensity relative to thicker beds. Tinker et al. (2013) suggest that topographic profile within this section of the Santa Elena limestone is controlled by relative fracture intensity and bed thickness (Tinker et al., 2013).

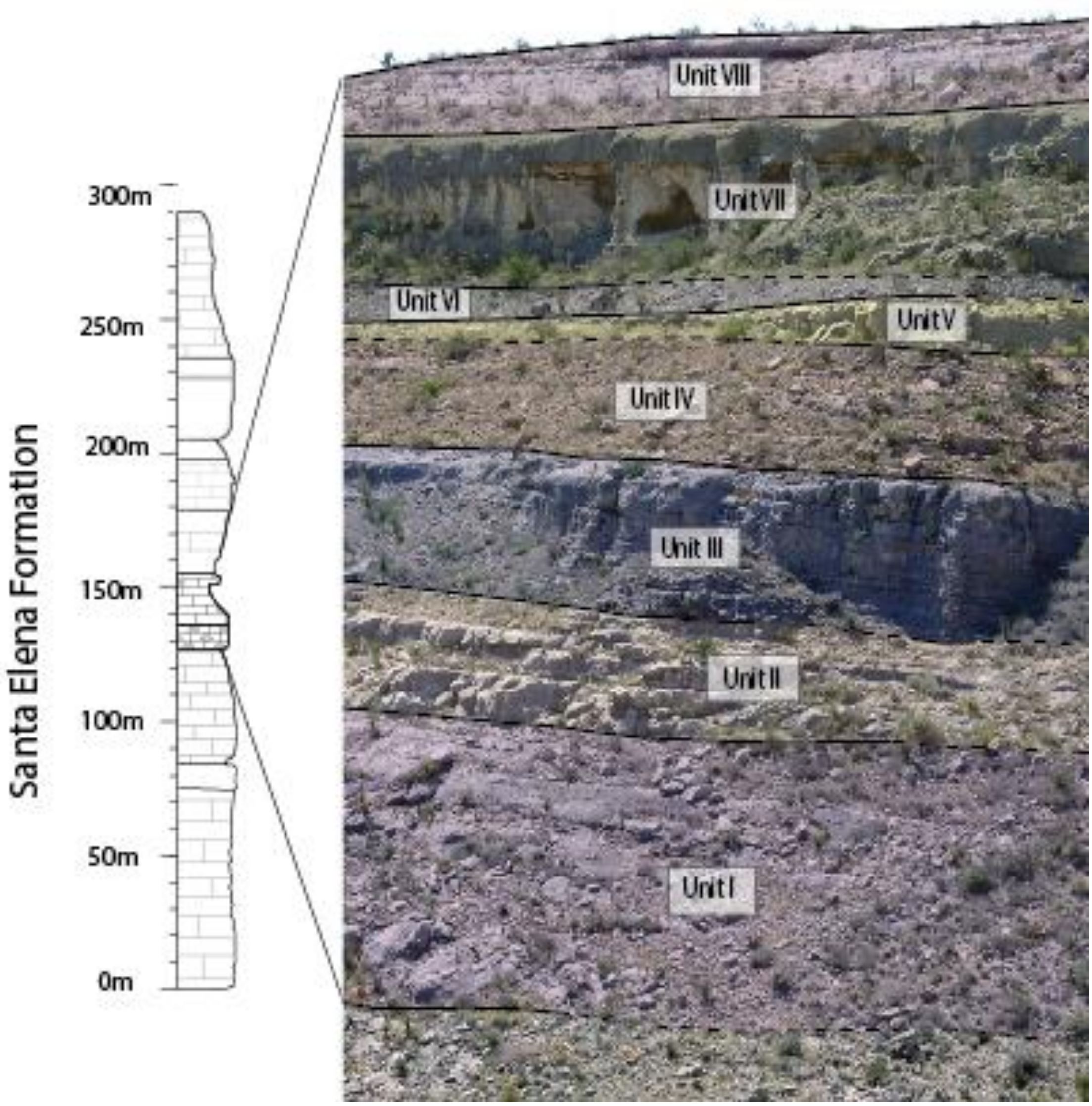

Figure 5. Units of the Santa Elena limestone that are exposed in the Stillwell anticline. Units were divided based on slope profiles (Mercado and Surpless, 2012).

Fracture Formation

Fractures are a type of brittle deformation in which rocks or minerals break due to applied stress (e.g., Twiss and Moores, 1992). Fractures form as a result of applied differential stress exceeding the strength of the rock, which is primarily controlled by composition. Each rock type has an experimentally-determined failure envelope that describes the critical strength of the material over a range of differential stresses (e.g., Twiss and Moores, 1992). However, the failure envelope can be shifted by changes in temperature, strain rate, confining pressure, and pre-existing weaknesses (e.g., Fossen, 2010).

Fractures are classified by the relative motion that occurs during fracture formation. Shear fractures are defined by a nearly parallel displacement of the fracture surface relative to the principal stress. In contrast, extension fractures display a displacement perpendicular to the maximum principal stress (e.g., Paterson and Wong, 2005). Therefore, classifying different types of fractures in a formation gives information about the state of stress and strain during fracture formation.

It is important to note that failure is the culmination of a progressive development of cracking during loading, rather than catastrophic spread of a single crack at a peak stress (Paterson and Wong, 2005). Analyses of rock failure and fracture propagation must take into account several factors: (1) the location and orientation of micro-crack initiation; (2) subsequent growth of individual micro-cracks with increased loading; (3) the increased number of micro-cracks with increased loading; (4) the interactions between growing micro-cracks as their lengths and numbers increase; and (5) the stability of the crack proliferation process and the possibility of its localization, leading to macroscopic failure (Paterson and Wong, 2005). Understanding such microfracturing mechanisms of initiation and spread is crucial for the understanding of porosity and permeability in rocks.

Fracture Intensity

Fluid flow through rocks depends on the number of fractures present, their aperture width, and their connectivity (e.g., Ortega et al., 2006; Tran, 2007). Fracture intensity, defined as the amount of fractures per unit of length, is one of the key parameters used to quantify permeability of rocks. There are many challenges that scientists face when trying to measure fracture intensity in the subsurface. For example, fracture data are commonly obtained from boreholes, but large fractures are commonly widely spaced, so the probability of encountering such fractures is low (Laubach, 2003; Laubach et al., 2004). Research has shown that small-scale fractures can be treated as proxies for the occurrence of larger fractures (Ortega et al., 2010). Therefore, a systematic measurement of fractures across scales allows scientists to compare fracture systems and intensity to geological controls such as structural position, texture, composition and stratigraphic position (e.g., Nelson and Serra, 1995; Ortega et al., 2006).

In addition, previous studies of fracture intensity have failed to account for fracture aperture size (Ortega et al., 2006). Opening size of fractures in the sub-surface vary across at least six orders of magnitude (Gillespie et al., 1993; Marret et al., 1999). The total volume of fractured rock relative to intact rock can be dramatically different within formations with equal number of fractures but different aperture ranges. Therefore, it is much less accurate and meaningful to quantify fracture intensity without including fracture aperture as part of any calculation (Ortega et al., 2006).

Observational Bias in Outcrop Studies

Rock fractures typically cannot be observed in a complete three dimensional form, but rather as traces on the surface of an outcrop, rock core, or mine wall (e.g., Mauldon et al., 2001). Characteristics of fracture systems are commonly inferred from fracture trace parameters, such as fracture trace intensity and length (e.g., Mauldon et al., 2001). The measurement and subsequent analysis of fracture features may be subject to significant error due to unintentional censoring and length bias on an observational plane (e.g., Terzaghi, 1965; Palmstrom, 1996). The orientation of a surface of observation strongly influences the number of fractures sampled (e.g., Terzaghi, 1965; Palmstrom and Stromme, 1996). It is known that fractures perpendicular to the plane of observation have a higher probability of intersecting such a plane. Therefore, fractures with an acute angle relative to the observational plane will be less likely to be observed (Figs. 6A and 6B).

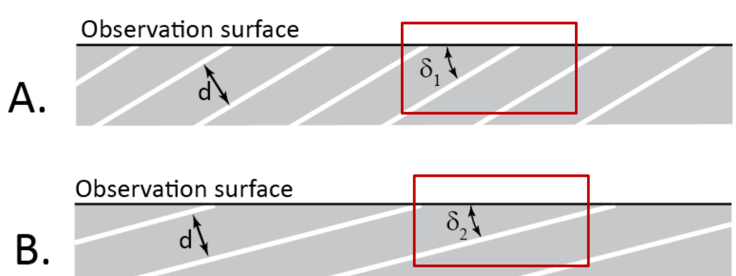

Figure 6. Diagram illustrating the influence of intersection angle, δ, on the number of fractures counted on a given observation surface. In both A. and B., the fracture spacing, d, is the same. **A.** demonstrates a relatively large angle of intersection and a correspondingly large number of fractures that intersect the surface, while the fractures shown in **B.** have a smaller angle of intersection and a correspondingly small number of fractures that intersect the surface. (Surpless, 2013).

In order to account for this observational bias, many geologists like Palmstrom (1995) developed a weighted joint density (**wJd**) method which includes a rating factor (***f_i***) to account for the bias. To simplify use of this rating factor, Palmstrom (1995) divided the angles of intersection into four ranges (Table 1). With this scheme, each fracture is weighted according to the corresponding rating factor, which accounts for differences in the angle of intersection.

Table 1. Angle intervals and rating factors
(Palmstrom, 1995)

Angle (δ) between fracture and observation surface	**Rating factor (f_i)**
>60°	1
31 - 60°	1.5
16 - 30°	3.5
<16°	6

Fracture data obtained from outcrops should also be corrected for the error related to the shape of the observational plane. As with the angle of intersection between the fracture planes and the observation plane, the two-dimensional angle of intersection between the fracture-plane line of intersection and the shape of the rectangle also affects the number of fractures that can be observed. Figure 7 shows the orientations of four different fracture orientations on the observation plane and where the fracture plane and the observation plane intersect at a line. As Surpless (2013) explains, fractures oriented similar to fracture 1 (red fracture in Fig. 7) have the lowest probability of being observed, based on the length along which fractures of that orientation can intersect (λ_1, dashed red line perpendicular to fracture 1). Fractures oriented at a position of either example of fracture 3 (green fracture in Fig. 7) have the highest probability of being observed, based on the length along which fractures of that orientation can intersect the area of observation (λ_3, dashed green lines perpendicular to either fracture 3). Intermediate between those orientations are fractures oriented like fracture 2 (blue, Fig. 7), which would intersect the area of observation along length λ_2 (dashed blue line perpendicular to fracture 2; Surpless, 2013).

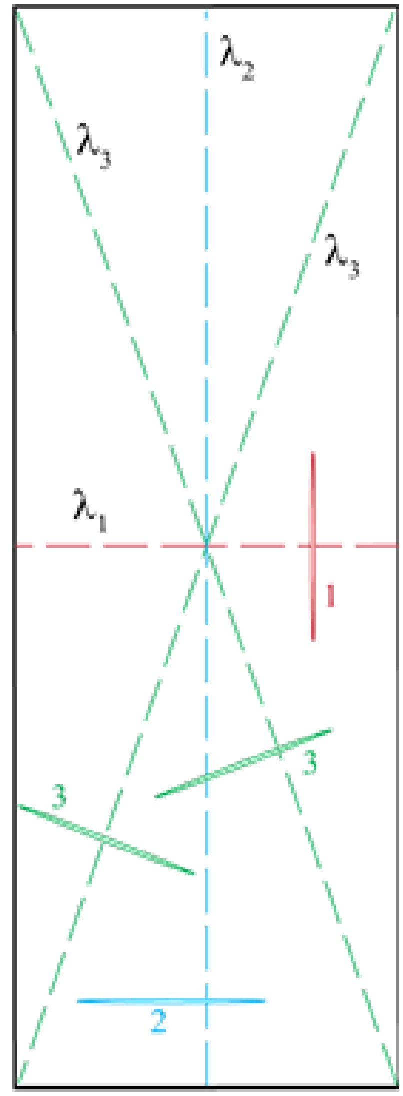

Figure 7. Rectangular observational plane and possible fracture orientations. Solid lines represent possible fracture orientations (from Surpless, 2013).

In order to avoid this type of observational bias, geologists try to use circular observational surface areas, so that the probability of observing a fracture in any orientation is equal for all fractures (Mauldon et al., 2001). In a circular observational plane, λ_1, λ_2, and λ_3 would all be equal to the radius of the circle. With equal observational lengths, the probability of encountering fractures at any location and orientation would be the same, so an observational bias related to the dimensions of the observational surface can be avoided.

III. RESEARCH METHODS AND DATA

To answer my research questions, I collected data from fracture systems at five different structural positions within nearly identical limestone beds of the Stillwell anticline. I also used field photography, thin section petrography, Optical Cathodoluminescence (CL) imagery and Scanning Electron Microscopy (SEM) to document characteristics of the fracture systems present. Moreover, I performed statistical analyses with the goal of quantifying the relationships between the fracture variables measured.

Field Methods and Data

I collected data about fracture systems from transitional – scale within a Santa Elena limestone beds at different structural positions within the Stillwell Anticline. These structural positions included the forelimb (location 1), the middle-forelimb hinge (location 2), the middle limb (location 3), the middle-backlimb hinge (location 4), and the backlimb (location 5; Fig. 8). Limiting sampling to different structural locations within the same limestone beds enabled me to keep composition, stratigraphic position, depositional environment and bed thickness constant.

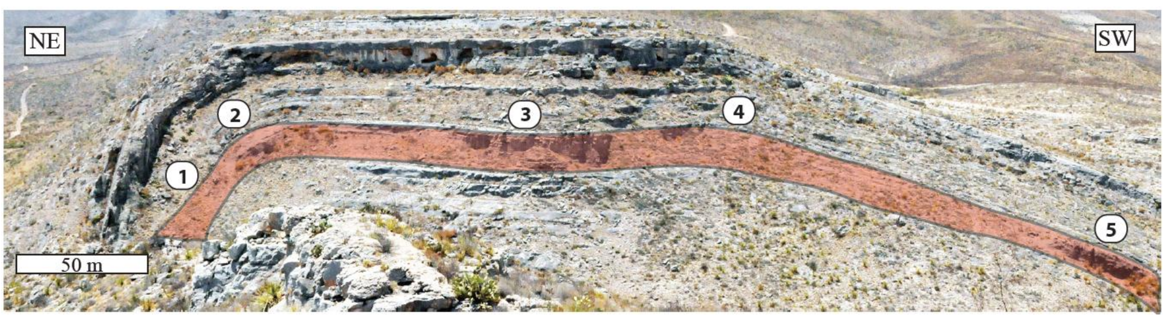

Figure 8. Cross-sectional view of the Stillwell anticline, indicating the Santa Elena unit (Unit III in Figure 5) chosen for measurements and the locations of fracture observations. Numbers indicate different structural positions. Location 1 is the forelimb. Location 2 is the forelimb hinge. Location 3 is the middle limb. Location 4 is the backlimb hinge. Location 5 is the backlimb.

For this transitional – scale analysis, I documented five fracture characteristics, including the position of the fracture within the observational area, fracture orientation, fracture aperture, fracture length, fracture morphology and fracture fill. I chose observation locations with significant surface relief in order to best observe the three-dimensional orientation of each fracture. Below, I define the five fracture variables measured in the field:

X-Y position: I measured the relative horizontal location of each fracture by making the left-most fracture horizontal position 0 (zero). I labeled all fractures by hand and took digital images of each location. I obtained the vertical location of each fracture using bed scale photographs. The lower bedding plane was used as vertical reference point 0 (zero).

Orientation: I measured dip azimuth and dip of each fracture.

Fracture Aperture: I measured opening displacements of fractures using the logarithmically graduated fracture-aperture comparator of Ortega et al. (2006; Fig. 9). I used this tool with a hand lens to measure fractures in the range from 0.05 to 5 mm aperture. The comparator contains lines with increasing width starting at 0.005 mm and ending at 5 mm. Because fracture aperture has a logarithmic relationship with fracture intensity, increments measured by the comparator are evenly spaced on a logarithmic scale (Ortega et al., 2006).

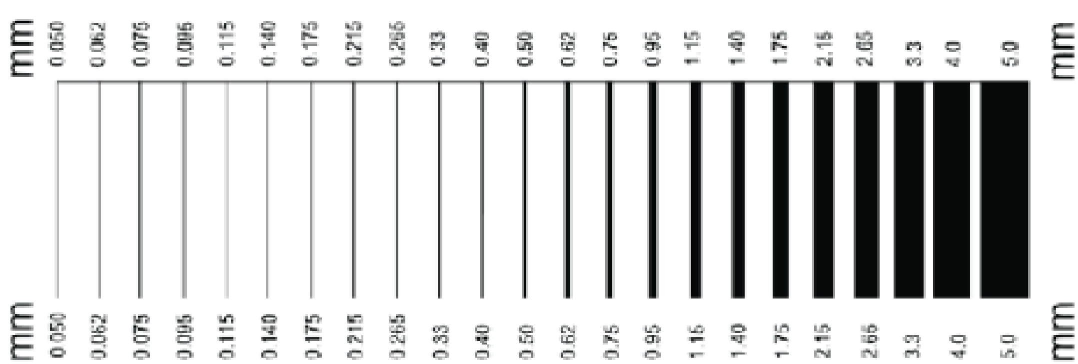

Figure 9. Fracture-aperture comparator (from Ortega et al., 2006; not to scale).

Fracture Length: I measured the length of each fracture with a ruler.

Fracture Fill*:* I described each fracture as filled, not filled, or partially filled.

Fracture Morphology*:* I classified each fracture as planar, sub-planar, or sinuous (Fig. 10).

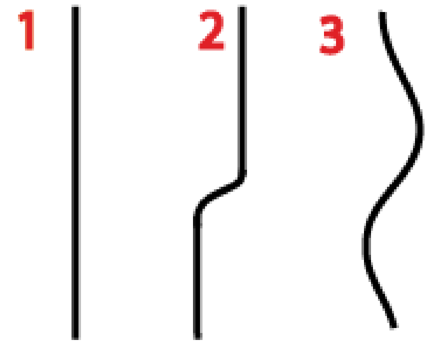

Figure 10. Classification of fraction morphology. 1 is planar; 2 is sub-planar; 3 is sinuous.

Because previous research indicates that fracture intensity changes very little above one hundred measurements (Ortega et al., 2006), I measured a minimum of two hundred fractures at each location. In addition, I took field photographs at the outcrop scale, as well as detailed fracture photographs with a Bodelin Proscope HR with a 50X macroscopic lens.

All data were collected from a dense, uniform, light gray lithographic limestone bed in Unit III of the mechanical stratigraphy that was traced at throughout the fold formation (Fig. 8). This unit consists of limestone layers with discontinuous nodular chert interbeds (Fig. 11). Within unit III, the limestone bed selected at each structural position had approximately the same thickness and nearly identical lithological characteristics. I measured 5 variables for each of 1025 fractures (including all structural positions). Results are in Appendix A. Figure 12 shows the marked fractures from the outcrop at each structural position. The average bed thickness was 12 cm, and although the average stratigraphic position above the base of Unit III varied, the bed lithologies from the five structural positions were nearly identical. Table 2 shows the characteristics of the bed at each structural position.

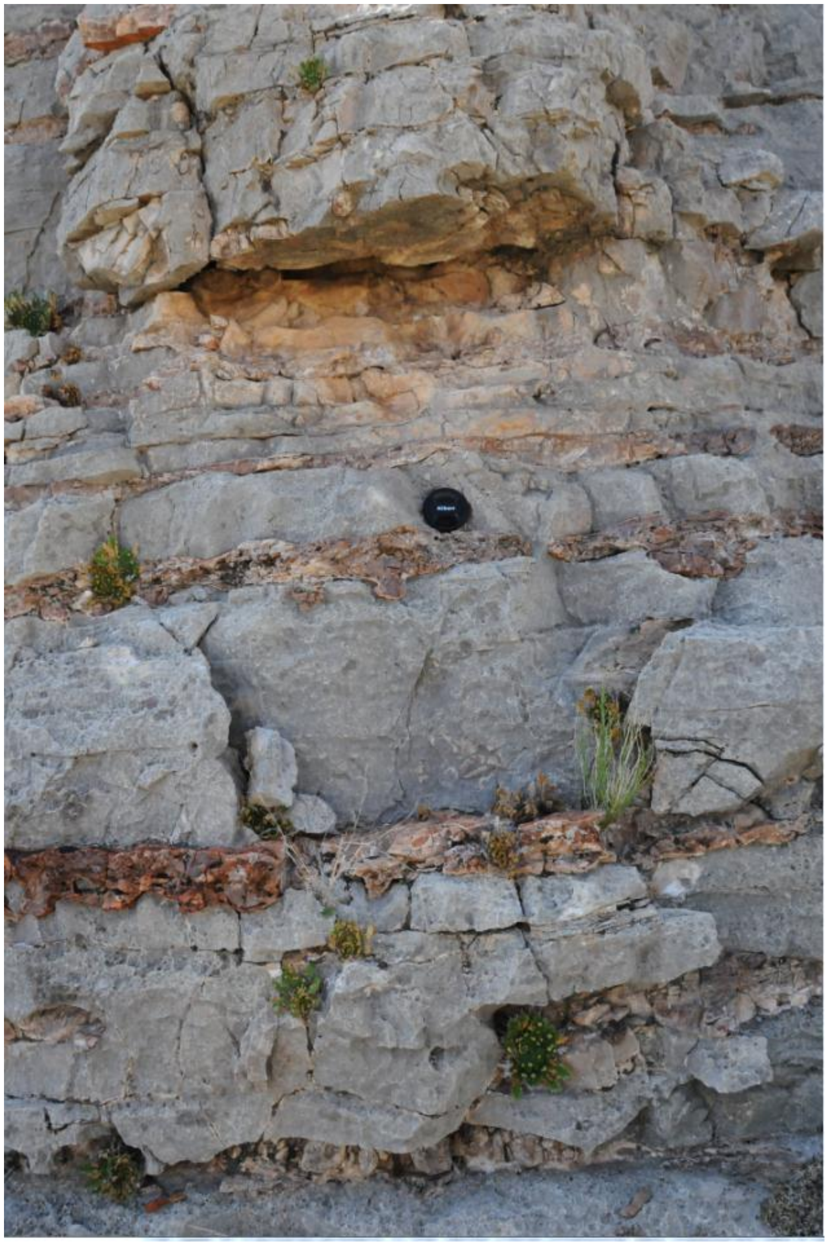

Figure 11. Unit III of the mechanical stratigraphy of the Stillwell Anticline (shown in fig. 5). Santa Elena Limestone beds are interbedded with discontinuous chert beds.

Figure 12. Fracture measurements at each location. Location 1 is within the forelimb, location 2 is within the mid-forelimb hinge, location 3 is within the middle limb, location 4 is within the mid-back limb hinge, and location 5 is within the middle-back limb.

Table 2. Characteristics of beds at each structural position

Structural Position	Stratigraphic Position Above Base (m)	Thickness of Bed (cm)	Bed Orientation (azimuth, dip)	Observation Plane Orientation (azimuth, dip)	Systematic Joints (azimuth, dip)	Easting (m) UTM Zone 13	Northing (m) UTM Zone 13
1. Forelimb	1.75	13	052, 39	171,60	(312, 82) (266, 61)	697901	3281928
2. Mid-Forelimb Hinge	2.05	12	041, 29	288,56	(135, 89) (230, 86)	697985	3281815
3. Middle Limb	1.55	9	147, 06	316,65	(333, 75) (087, 90)	697896	3281814
4. Mid-Backlimb Hinge	6.04	13	278, 14	115,62	(343, 75) (086, 69)	697694	3281978
5. Backlimb	5.77	13	228, 27	178,66	(123, 85) (032, 84)	697757	3281808

The types of fractures present in the Santa Elena limestone have a variety of textural characteristics. Fracture fill had different color and texture than the grey lithographic limestone. The vast majority of fractures present had a white to tan calcite fill (Fig. 13a). Surfaces on the host rock and a significant number of fractures displayed brown/black organic growth (Figs. 13b and 13c). Some fractures present were filled with both calcite and organic material, commonly making the fractures more visible in outcrop. Figures 13d and 13e show that not all fractures contained fill. Some open fractures showed evidence of euhedral calcite crystallization on fracture walls (Figs. 13e and 13g).

Fractures observed in outcrop had three primary morphologies. Planar fractures were common as both filled and non-filled fractures (Figs. 13d, 13e, and 13f). Other morphologies observed were sinuous fractures (Fig. 13g) and sub-planar fractures (Fig. 11), with sub-planar fractures most common at all structural positions.

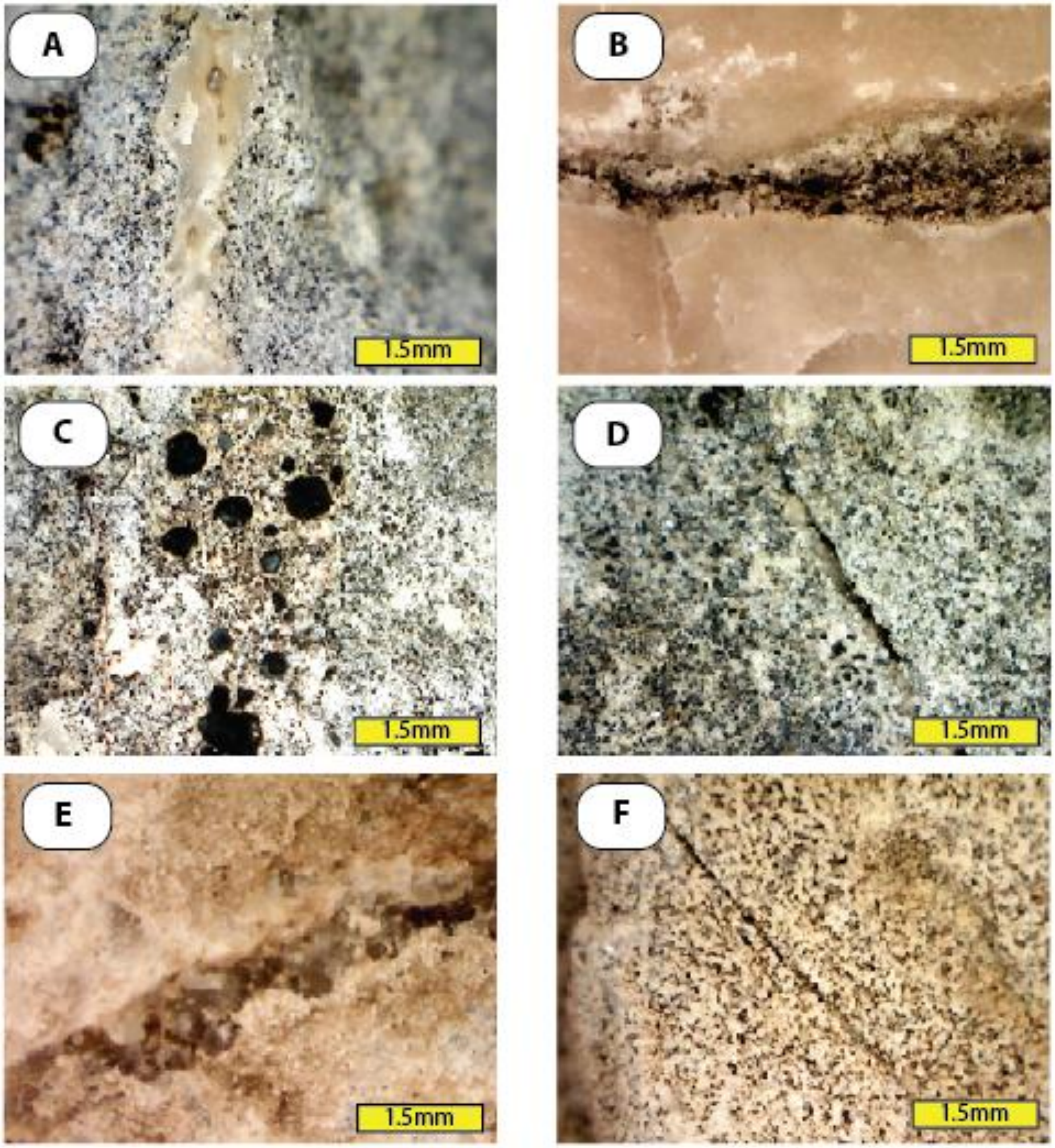

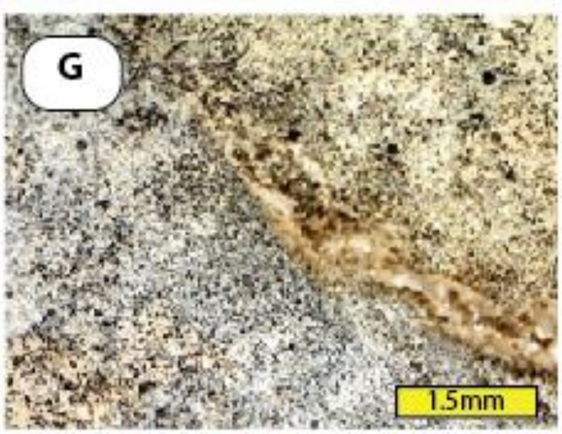

Figure 13. Field photos of fractures in the Santa Elena Limestone of the Stillwell Anticline. (a) Fracture with calcite fill; (b) Fresh limestone surface with fracture containing organic material; (c) Limestone with organic material in host rock; (d) Planar open space fracture; (e) Fresh limestone surface with open space fracture; (f) Planar, opened space fracture; and (g) Sinuous fracture with calcite fill.

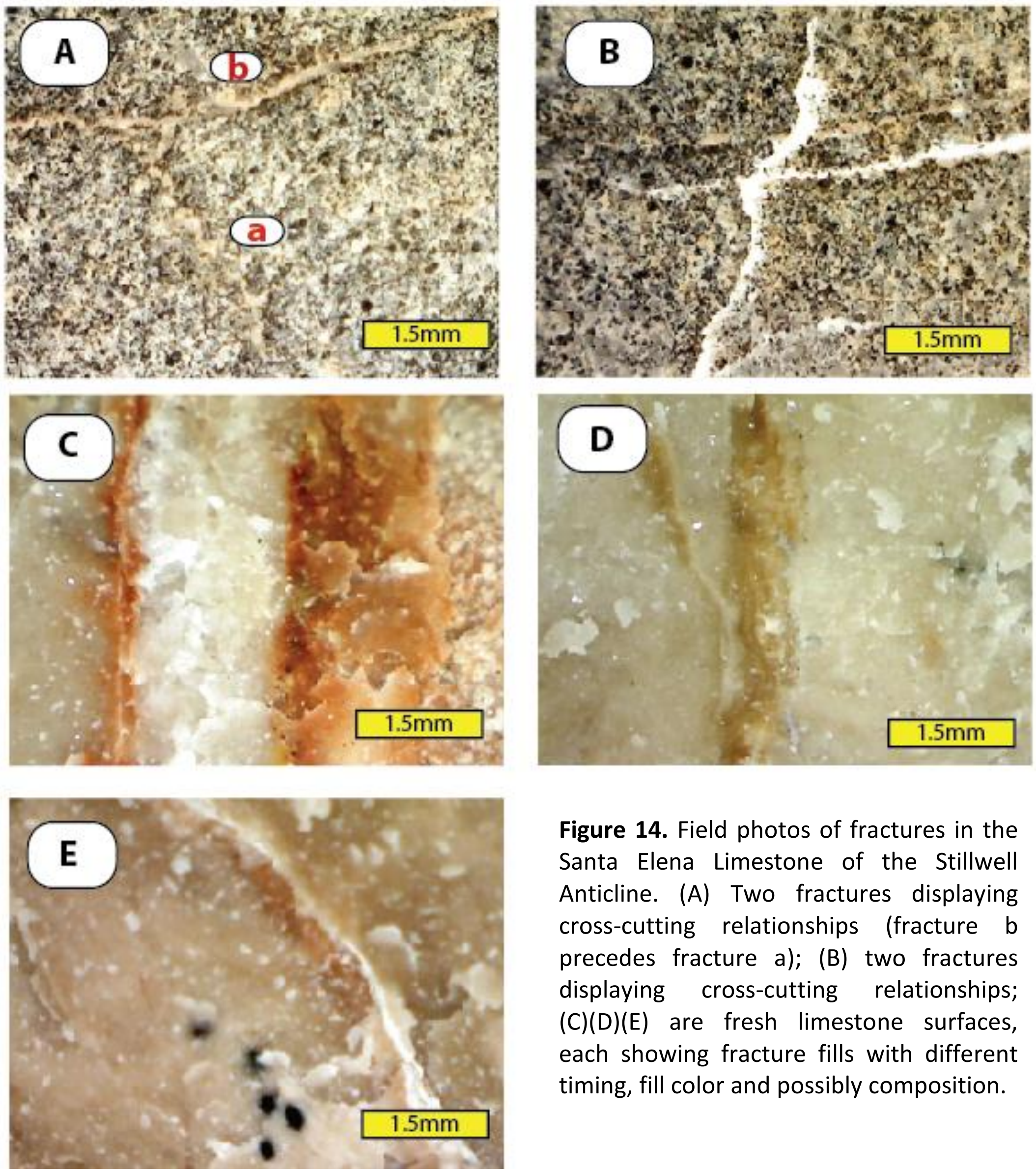

Figure 14. Field photos of fractures in the Santa Elena Limestone of the Stillwell Anticline. (A) Two fractures displaying cross-cutting relationships (fracture b precedes fracture a); (B) two fractures displaying cross-cutting relationships; (C)(D)(E) are fresh limestone surfaces, each showing fracture fills with different timing, fill color and possibly composition.

Fracture orientations and fills at all structural positions display evidence for multiple generations of fracture formation, including cross-cutting relationships (Figs. 14A and 14B). Moreover, fresh surfaces show zonation in fracture fill that is highlighted by sharp changes in fill color. Figure 14C shows a fracture with a brown to red calcite fill on the outer margins of the fracture, with white material bound between those margins; this pattern suggests a temporal change in fluid composition, with the red/brown calcite precipitating in the fracture prior to the later white calcite. These relatively sharp color changes suggest abrupt changes in fluid composition following fracture propagation and opening events (Figs. 14C, 14D, and 14E).

The characteristics of fractures measured at each structural position appear to vary between locations (Table 3). The average fracture aperture measured at all five locations was 0.102 mm (Table 3). The highest average aperture was found in the fore limb and middle limb and lowest in the backlimb hinge. The average fracture length observed at all five structural positions was 3.84 cm, with the longest average fracture length at the forelimb location and the shortest average fracture length at the fore-limb hinge location (Table 3). At all five locations, fractures were usually filled and sub-planar.

Table 3. Summary of Field-based Fracture Data

Location	Area of observation cm^2	Total number of fractures measured	Average aperture (mm)	Average length (cm)	fill mode	morphology mode	Fracture Intensity (fractures/cm^2)	Percent of Open Pore Space
Fore-limb hinge	239	204	0.086	2.81	filled	Sub-planar	0.85	20.72
Fore limb	932	203	0.151	5.02	filled	planar	0.23	17.34
Middle limb	1223	211	0.106	4.84	filled	planar	0.17	8.73
Back-limb hinge	234	204	0.076	2.77	filled	Sub-planar	0.88	18.51
Back limb	372	203	0.091	3.75	filled	Sub-planar	0.55	18.45
Final Average		**205**	**0.102**	**3.84**	**filled**	**Sub-planar**	**0.54**	**16.75**

Table. 4 Orientation of high density fracture sets

Location	Sets	Azimuth Range	Dip Range
Fore-limb hinge	1a	34	53
		26	62
	1b	355	46
		348	44
	1c	354	58
		343	71
Fore limb	2a	112	59
		125	49
Middle limb	3a	71	85
		76	90
	3b	73	57
		78	52
	3c	151	69
		156	66
	3d	165	46
		183	75
	3e	211	85
		216	78
Back-limb hinge	4a	21	75
		12	88
	4b	305	44
		276	58
	4c	272	48
		258	60
Back limb	5a	119	60
		146	39
	5b	169	48
		182	38

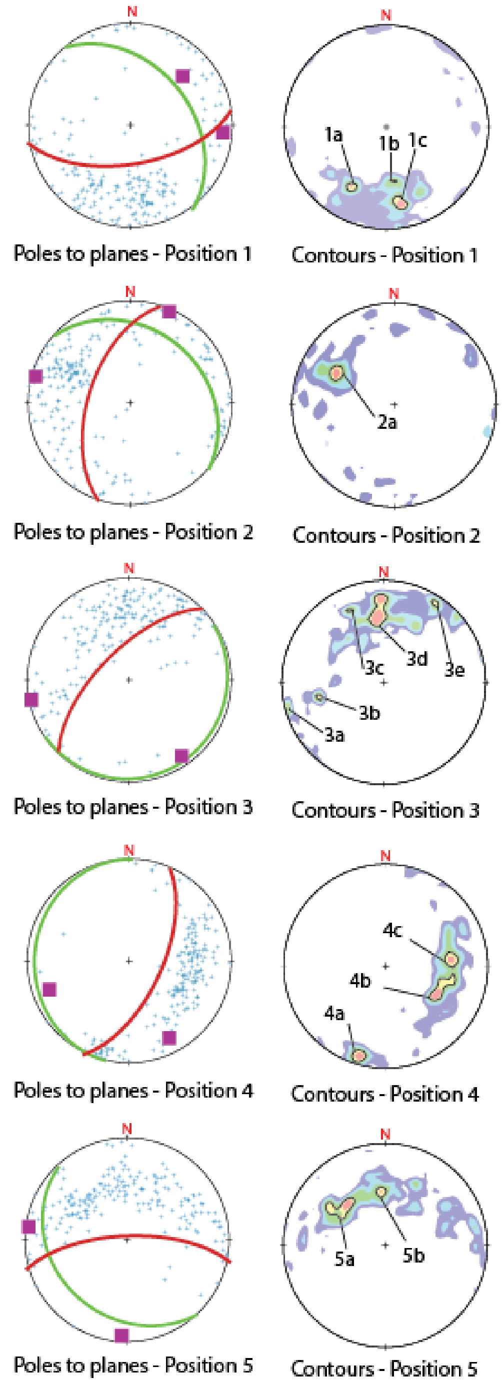

Figure 15. Stereonet diagrams of fracture orientations. Left column shows poles to planes of fracture orientations at each structural position. Orientations of observational planes are shown in red great circles. Orientations of beds are shown in green great circles. Purple squares represent orientation of macro scale joint sets. Stereonet diagrams in the right column show density contour and display high density in red and labeled.

Fracture systems at different structural positions do not appear to have similar fracture orientations. Figure 15 displays fracture orientation data as poles to planes, with relative fracture densities contoured in order to identify fracture sets (Table 4) at each location (contouring performed using StereoStat structural analysis software). Most fracture data appear to cluster along great circles related to observational plane orientation and bedding orientation. Plots of the major joint sets at each structural position reveal a dominant north-south strike and sub-vertical dip for macro scale fractures at all locations (Fig. 15).

Laboratory Methods and Data

I have separated my description of laboratory methods and data by structural position (Locations 1 – 5). However, since samples obtained at each location represent such a small percent of the bed studied, it cannot be assumed that characteristics observed in thin section fully characterize that specific structural position.

Petrographic analysis of thin sections

I obtained images from thin sections using a petrographic microscope in order to describe the characteristics of fractures at each structural position. All photomicrographs were taken using a Lieca KL 2500 LCD microscope with a Leica DFC290 HD camera. I also used a Canon 8800F flat-bed scanner with two polarizing film sheets to obtained cross-polarized images of each entire thin section.

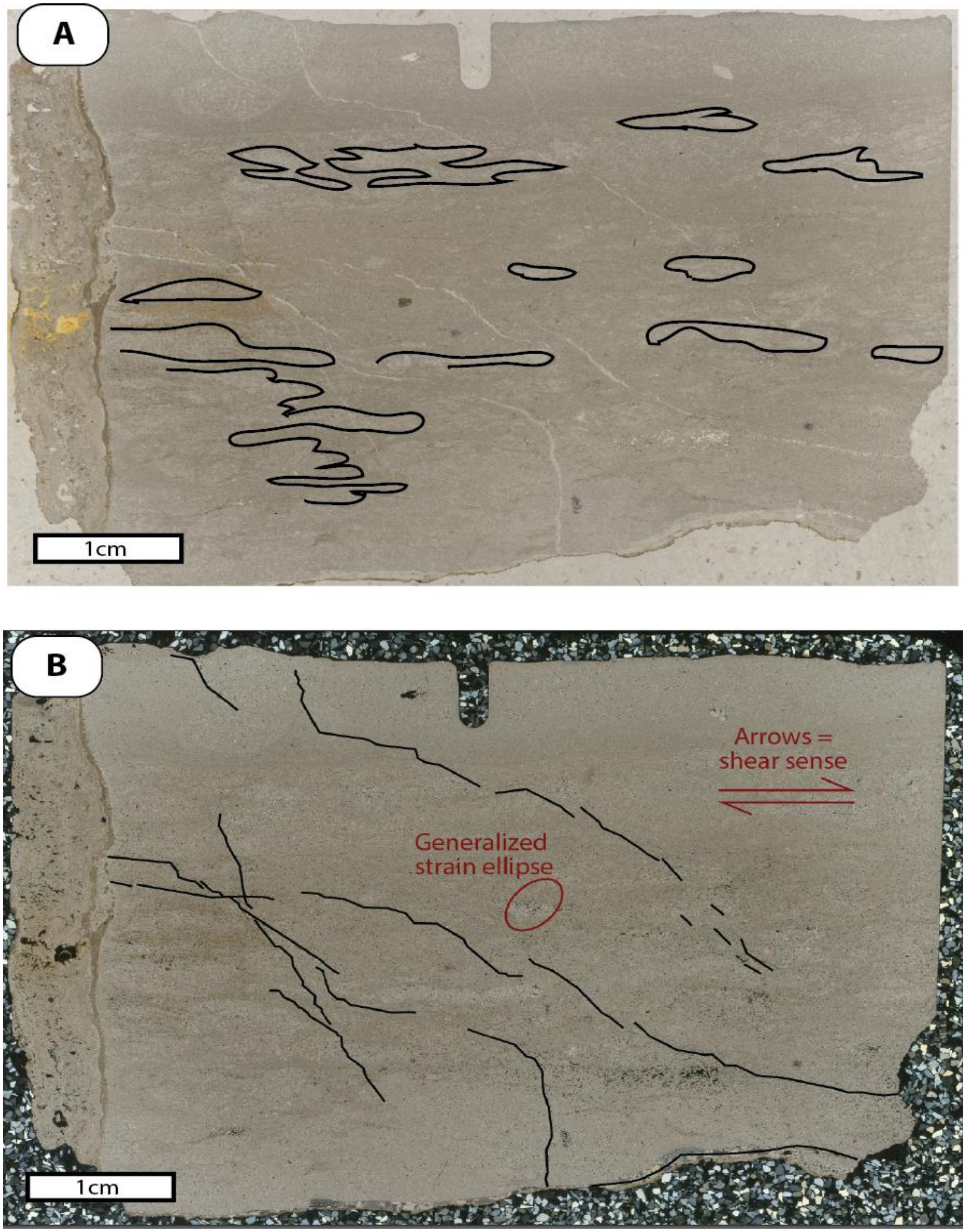

Figure 16. Cross-polarized images of full thin sections. Sample obtained at the forelimb location. (a) PPL with marked bioturbation; and (b) XPL showing dominant fracture orientation that are oblique to bedding, and the generalized strain ellipse, assuming opening mode fracture formation.

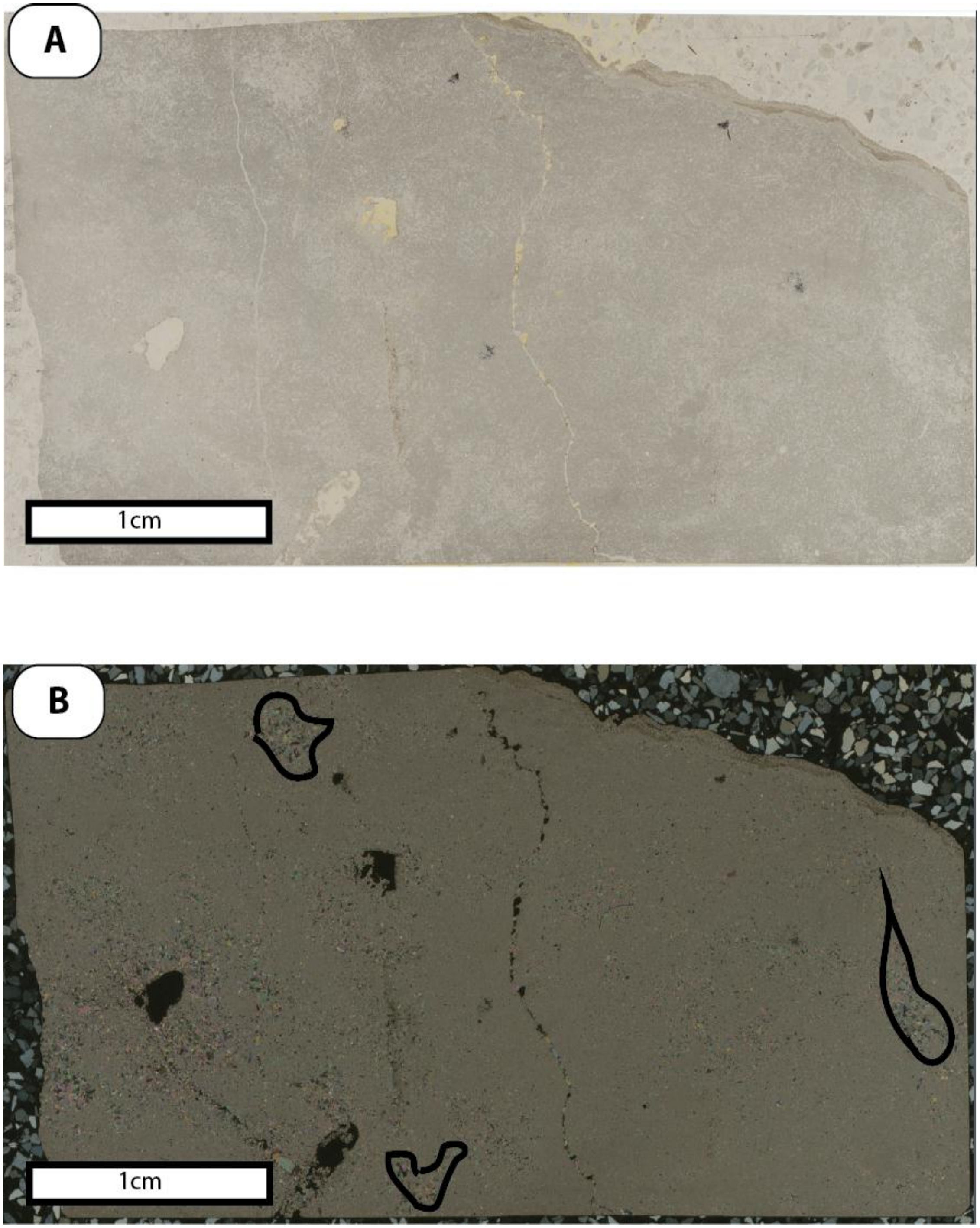

Figure 17. Cross-polarized images of full thin sections. Sample obtained at the forelimb hinge. (a) PPL; and (b) XPL with areas outlined to mark bioturbation.

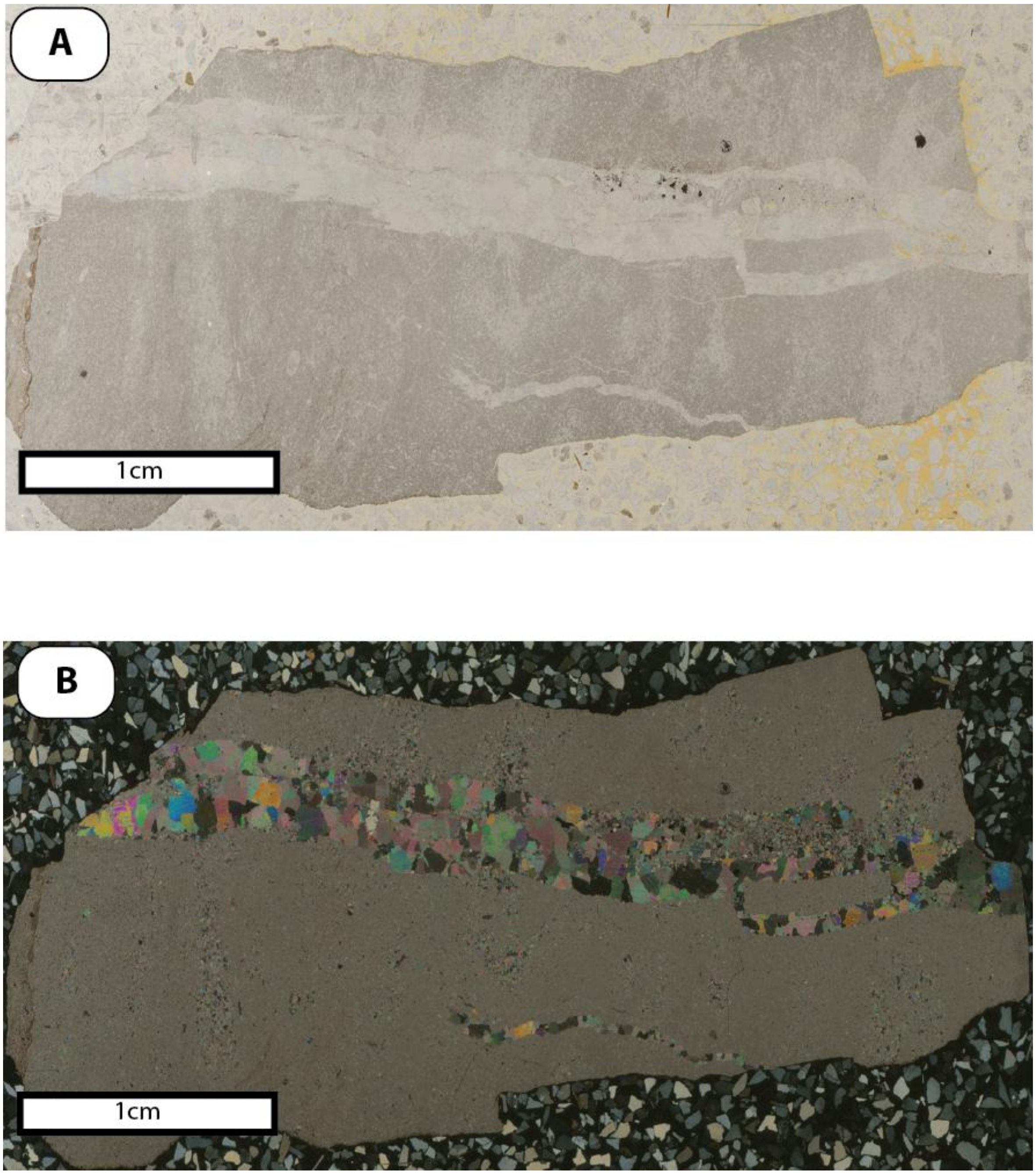

Figure 18. Cross-polarized images of full thin sections. Sample obtained at the middle limb. (a) PPL; and (b) XPL.

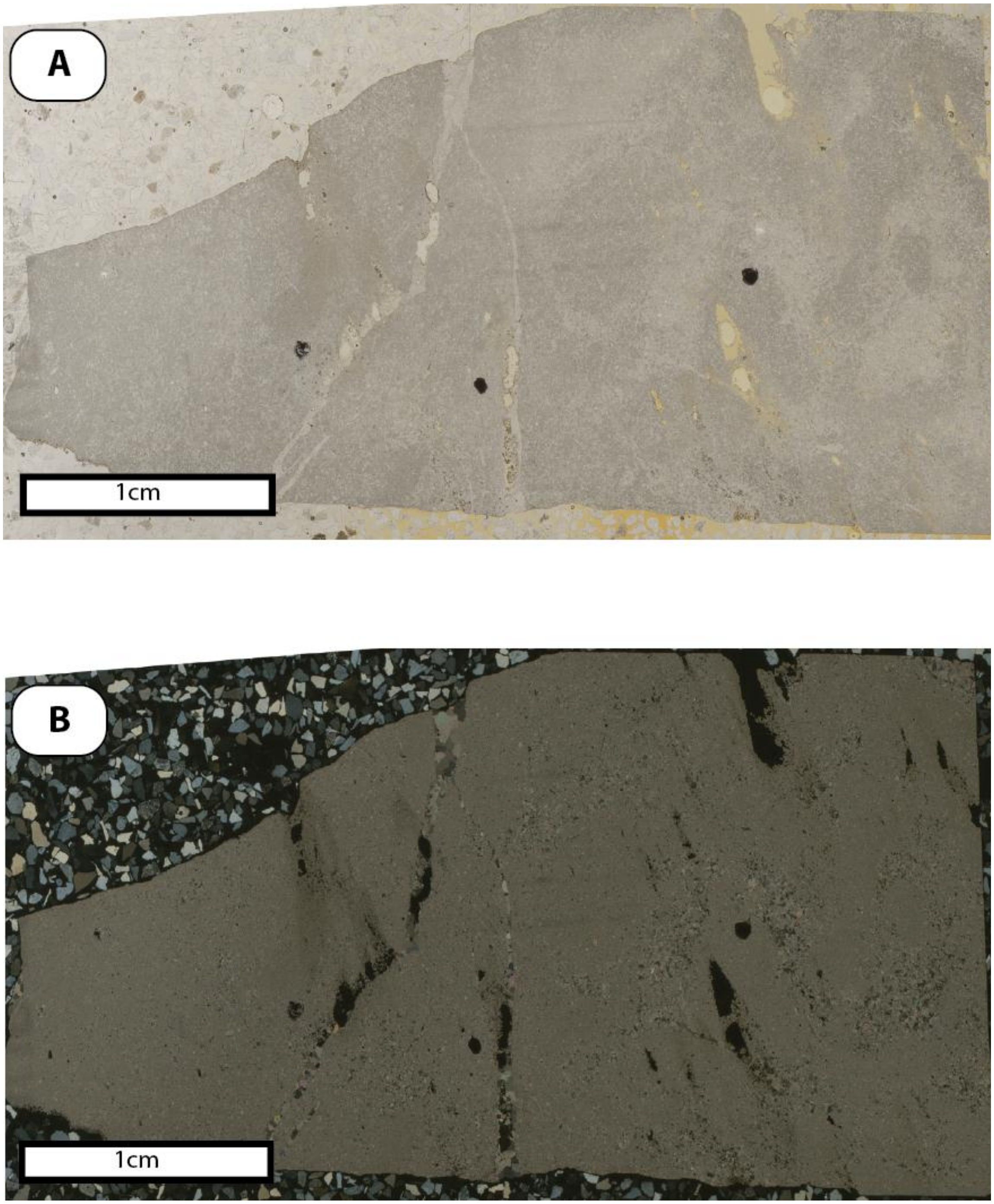

Figure 19. Cross-polarized images of full thin sections. Sample obtained at the backlimb hinge. (a) PPL (b) XPL with areas that suggest bioturbation.

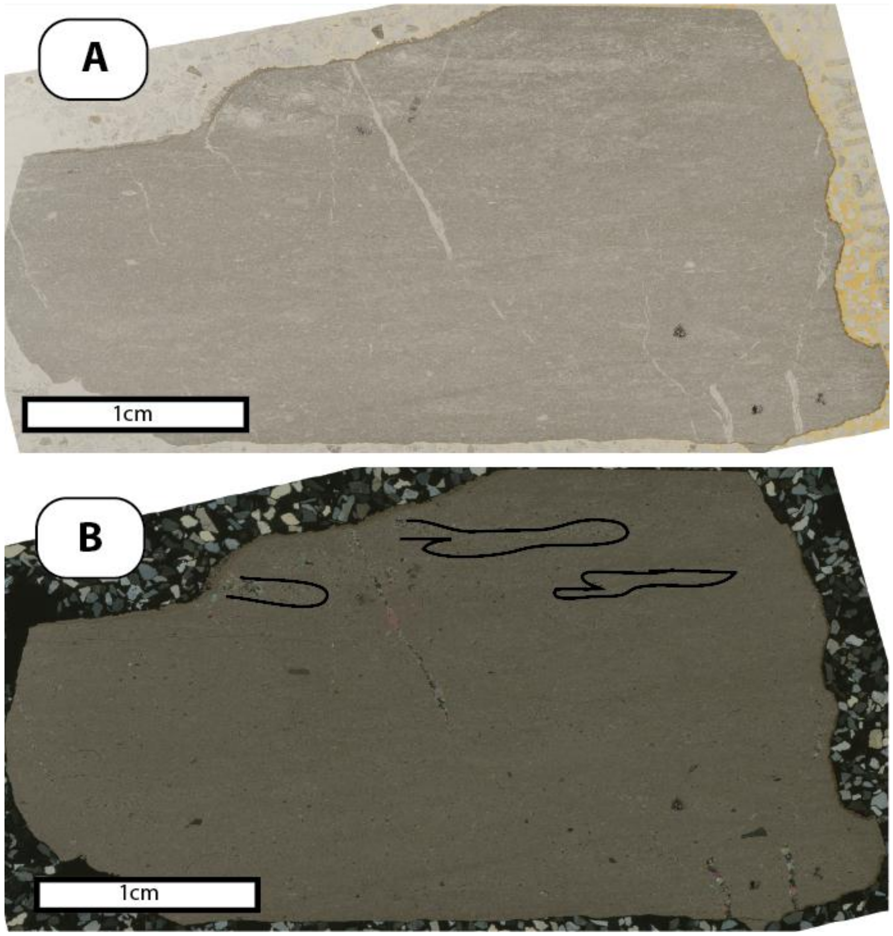

Figure 20. Cross-polarized images of full thin sections. Sample obtained at the backlimb. (a) PPL (b) XPL with areas marked to indicate bioturbation

Thin section petrography revealed that bedrock and fracture characteristics are fairly similar at all five locations (Figs. 16-20). Petrographic images show fine-grained, mud-like limestone at all five locations, with less than 10% fossils and/or organic material. Cross-polarized thin sections display evidence for burrowing and bioturbation (pers. comm., D. Lehrmann, 2013; Figs. 16, 17, and 20). Based on these observations, I have classified the limestone beds at all five locations as micritic limestone.

Although thin section petrography did not reveal the same fracture intensity documented in the field, the thin section from the forelimb location showed evidence of a significant fracture set (Fig. 16). Although fractures are affected by bedding, partially controlling their propagation, the consistent oblique orientation of the fractures relative to bedding in the forelimb sample (Fig. 16) allowed me to approximate the orientation of a generalized strain ellipse, assuming opening mode fracture formation. No dominant fracture set was documented at other structural positions.

Most fractures observed were filled with blocky calcite crystals (Figs. 21a, 21b, and 22a). These thick fractures were up to nearly 7 mm wide, and many of these fractures have multiple generations of fracture fill. For example, one thick fracture has one generation of fill that consists of blocky eu-to sub-euhedral calcite crystals and another generation with smaller calcite crystals that appear to have characteristics similar to the host rock (Fig. 21). Cross-cutting relationships indicate that the thick type of fracture describe above pre-dates a second type of thinner fractures. Figures 21 and 22 reveal a thin white fracture that cross-cuts the thicker fractures, appearing to follow calcite crystal boundaries from the thicker, earlier fracture fill.

Petrographic thin sections showed that fractures are predominantly calcite-rich, based on calcite staining and petrographic identification. Nevertheless, some of the thick fractures contained pyrite crystals and organic material. Figure 21a shows three distinct pyrite crystals (black opaque crystals) within the fracture's calcite fill, and Figure 22a shows possible pyrite crystals and/or organic material in between calcite crystals the fracture's fill. There are also smaller and less frequent dolomite fractures present in the thin sections analyzed (Figs. 22b and 23a). In Figure 23a, the fracture to the left shows a sinuous dolomite fracture with the inclusion of calcite crystals. This type of feature was seen in many other dolomite fractures. Moreover, dolomite was seen not only in fractures but also as isolated crystals within the host rock and as dolomitization fronts (Fig. 23b).

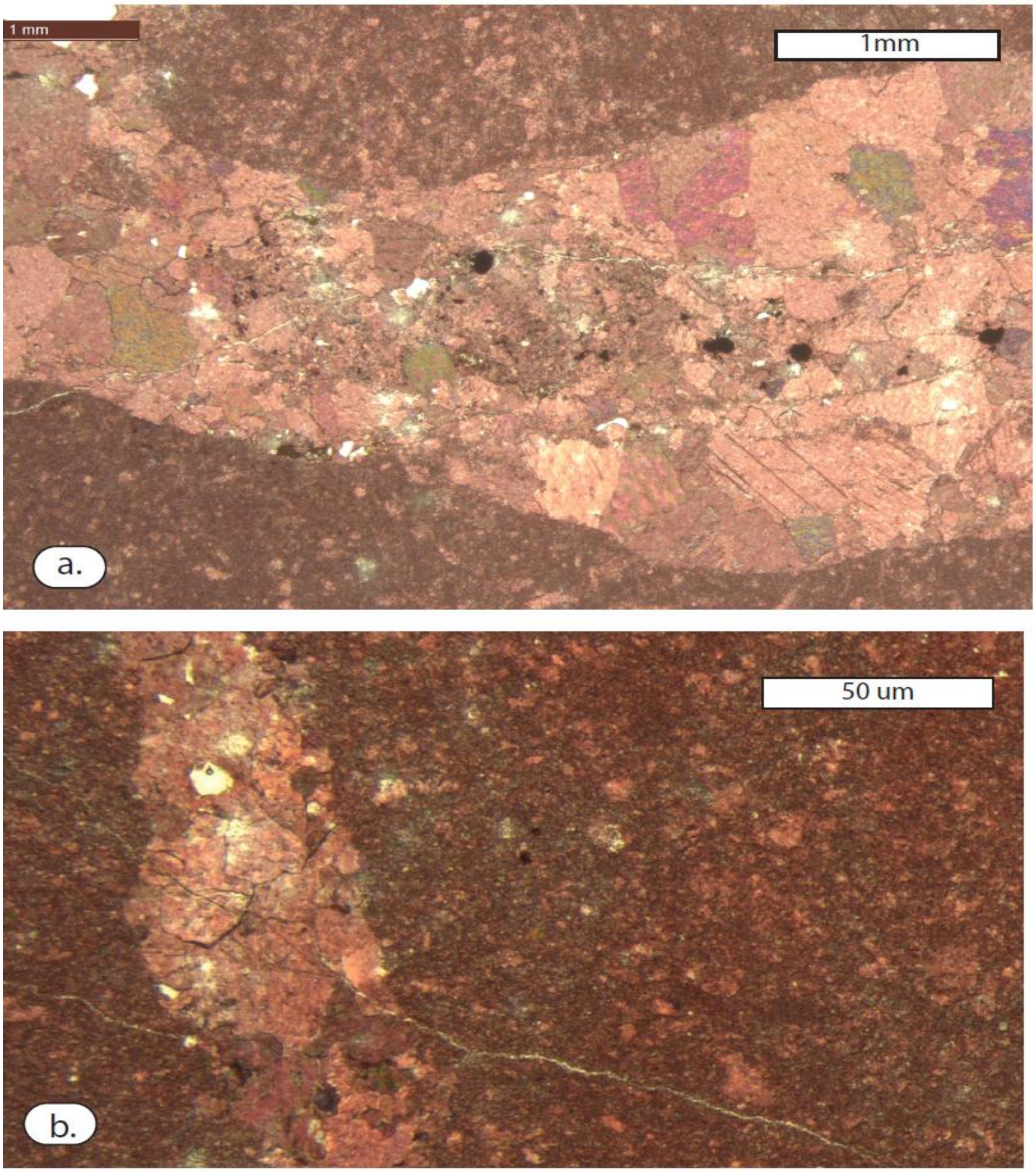

Figure 21. Photomicrograph with XP light showing thick calcite veins (middle limb). (a) Presence of black pyrite crystals. Thinner fracture cross-cuts thicker fracture. (b) Photomicrograph with XP light from a sample obtained in the backlimb. Thinner fracture cross-cuts thicker fracture.

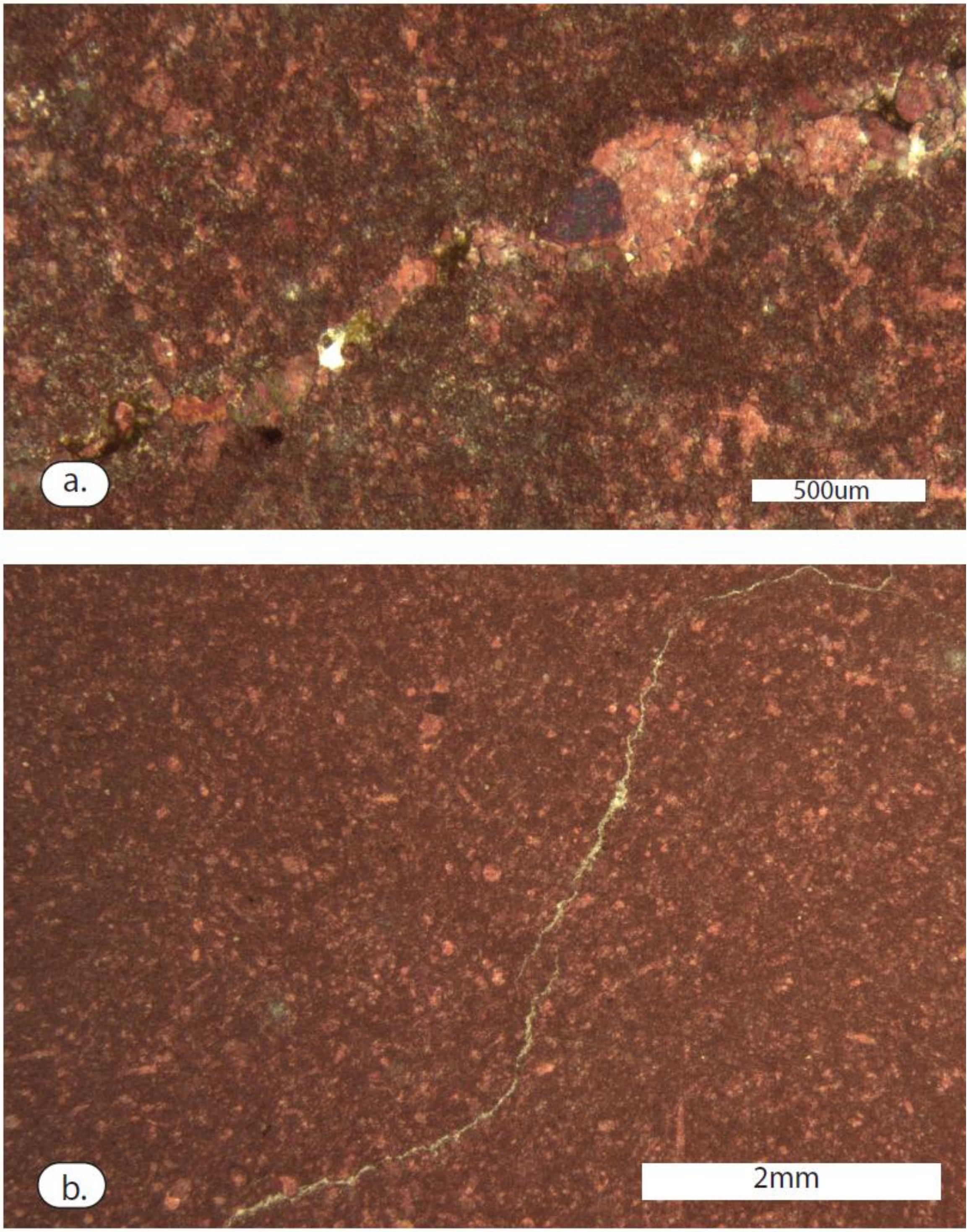

Figure 22. Photomicrograph with XP light showing different types of fractures (Forelimb). (a) Fracture with sub- to euhedral calcite crystals, possible organic material and/ or pyrite; (b) Thinner dolomite fractures.

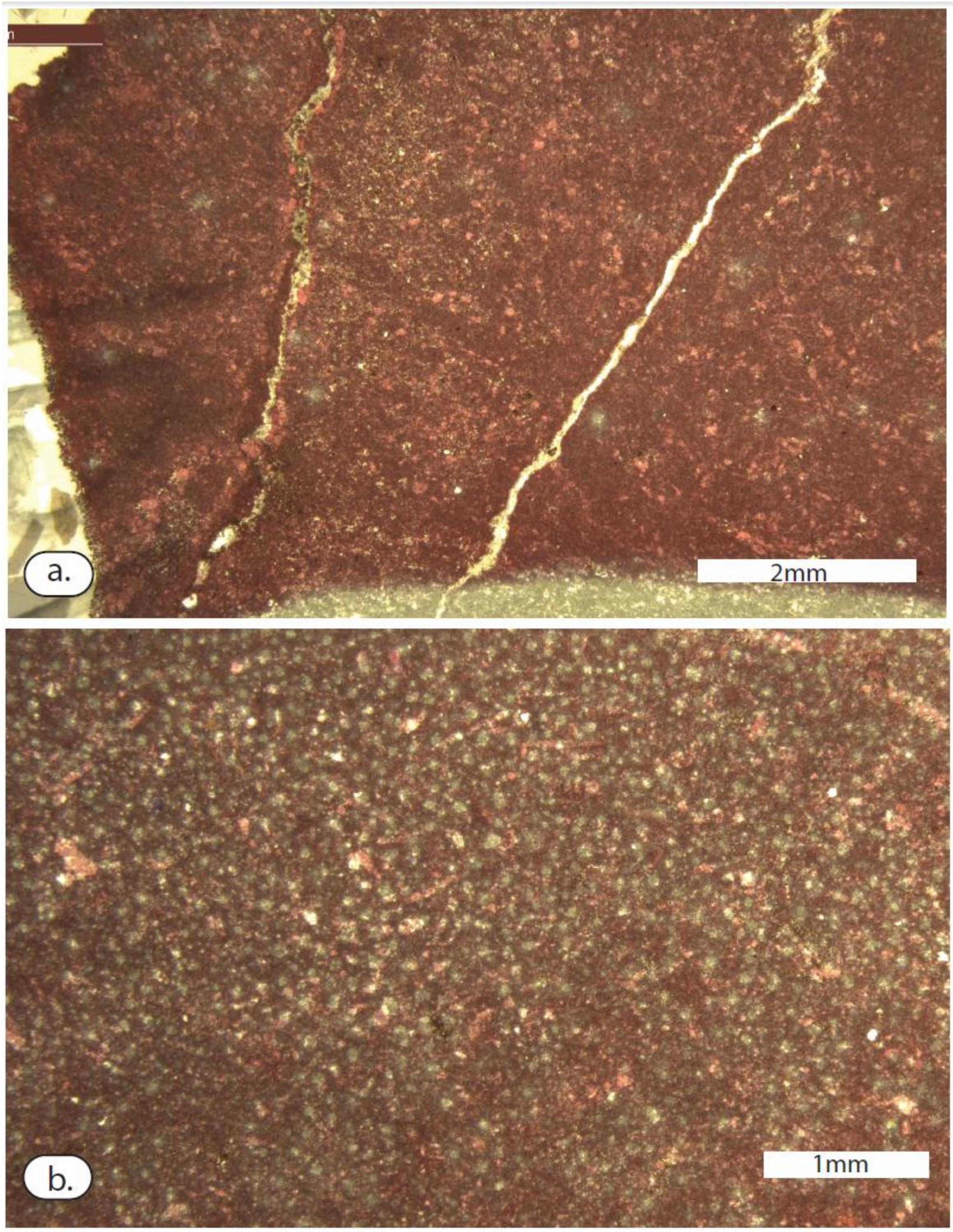

Figure 23. Photomicrograph with XP light showing the presence of dolomite (a) two dolomite fractures from a sample obtained in the Back limb hinge; (b) Dolomitization from the forelimb.

Optical Cathodoluminescence (CL)

I studied the luminescence characteristics of polished thin sections using a standard optical microscope with a cathodoluminescence (CL) attachment. The CL attachment, a *Reliotron III Cathodoluminescence Instrument,* was manufactured by Reliom Industries. This allowed me to see lithologic and fracture characteristics that are not visible in plane-polarized or cross-polarized optical microscopy. All photographs were taken with a Nikon Eclipse LV 100 camera at the Bureau of Economic Geology in Austin Texas. For all analyses, the instrument vacuum was set to 40mTorr with a potential difference of 7-8 kilovolts and a current of between 0.5 and 0.9 mA.

Optical CL images from all five locations revealed the presence of organic material, weathering fronts, multiple generations of fracture fill, calcite zoning and en echelon fractures. Moreover, these images also showed the existence of cryptic fractures, which are not visible with standard light microscopy. At all five locations, thick calcite fracture fill with eu-to subeuhedral crystals were the most prevalent.

Location 1: Forelimb

CL and PPL images of the same field of view from a sample from location 1 show the presence of different textural characteristics. Some thin fractures contained porous material, possibly filled with organic material. As seen in Figures 24a and 24c, the purple and bright red color, is likely organic material utilizing pore space. PPL images also show burrowed vs. non-burrowed textures (Fig. 24c), but these different textures were not visible under CL (Fig. 24d).

Fracture fills observed in the thin section for this location appear to have different chemical composition than the host rock. Fracture fills have a different color than the host rock (Figs. 24b and 24f). Moreover, it appears that there are multiple generations of fracture fill. In Figure 24b, one generation of fill appears nearly identical to the host rock (upper right fracture) and another generation reveals brighter CL than the host rock (lower left fracture). PPL and CL images also indicate the presence of echelon fractures that are at an oblique angle relative to bedding (Fig. 24c). These fractures are from the fracture set documented in the forelimb location and were documented in the thin section petrography section.

Location 2: Forelimb - Middle Hinge

CL and PPL images at location 2 indicate the presence of possible open pore space, fractures with different compositions than the host rocks, and weathering zonation. Figure 25a shows a sinuous fracture with possible open pores or plucked grains due to thin section polishing processes. The fracture fill of this fracture appears to have the same CL brightness throughout the fracture, and the difference in color between the fracture and host rock suggests different compositions (Fig. 25b). Other images suggest the presence of weathering zones in the rock, indicated by a change in texture from the fine-grained, unweathered host rock to the coarser-grained and weathered surface (Fig. 25c,d). The CL image suggests that the weathered section has a significantly different composition, based on the purple color relative to the bright red color of the unweathered host rock (Fig. 25d).

CL images from location 2 also show the presence of cryptic fractures. In PPL, fractures are very difficult to see, but CL images of the same locations clearly reveal fractures with different CL brightness than the host rock (Fig. 25e,g).

Location 3: Middle Limb

CL and PPL images observed at this location show fractures with three generations of crystal growth. In Figure 26a, the far right section of the image is the host rock (labeled "host rock"). The rest of the image is a single fracture with three different crystal generations. The first generation of fracture fill can be observed to the left of the host rock in a triangular zone with notably larger and blockier crystals than the surrounding crystals. A second generation of fracture fill is characterized by the growth of euhedral calcite crystals that appear to have nucleated on the fracture wall and are brighter under CL than the preceding fracture fill. A third generation of fracture fill is characterized by smaller calcite crystals of similar brightness to the preceding euhedral crystals (Fig. 26).

Similarly, in two other samples, the host rock is in the far left side of the image, and the three generations of fracture fill include a first generation characterized by large, eu –to sub-euhedral blocky calcite crystals with brightness similar to the host rock; a second generation where euhedral calcite crystals with a brighter CL signature appear to have nucleated on the fracture's wall; and a third generation of smaller calcite crystals (Figs. 26c and d). Figures 26a and 26c appear to have fracture fill generations with similar textural characteristics. Figure 26d also shows a fracture with three generations of fracture-filling crystallization. One generation of fracture fill consists of the large, eu-to sub-euhedral calcite crystals. A second generation of fracture fill can be observed in the euhedral crystals that appear to have grown from the fracture wall. A third generation consists of the large, blocky, CL-bright calcite crystals along with some large pyrite crystals.

Location 4: Middle - Backlimb hinge

CL and PPL images at this location show the presence of open pores, organic material and calcite zoning. A thick fracture with blocky, sub- to euhedral calcite crystals also contains open space, which appears to have formed after the fracture was filled with calcite crystals (Fig. 27). CL reveals zoning in calcite crystals, with the outer rings of crystals appearing similar to the host rock with brighter CL signatures (Fig. 27b). The CL image also reveals two optically bright zones sub parallel to the fracture wall. These zones suggest a short period of crystal growth while the fracture was opening. As in other CL images, purple color may indicate organic material.

Location 5 Backlimb

CL and PPL images at the backlimb location show the presence of sinuous fractures (Fig. 28a), multiple generations of fractures and crystal zoning. Figure 28c shows a thick fracture with zoned, blocky, sub-euhedral calcite crystals. CL images show that the fracture fills have a different CL signature than the host rock (Fig. 28b,c,f). A later fracture appears to wind through the fracture fill, utilizing crystal boundaries (Fig. 28e,f). The brown color in the PPL image (Fig. 28e) suggests the presence of organic material.

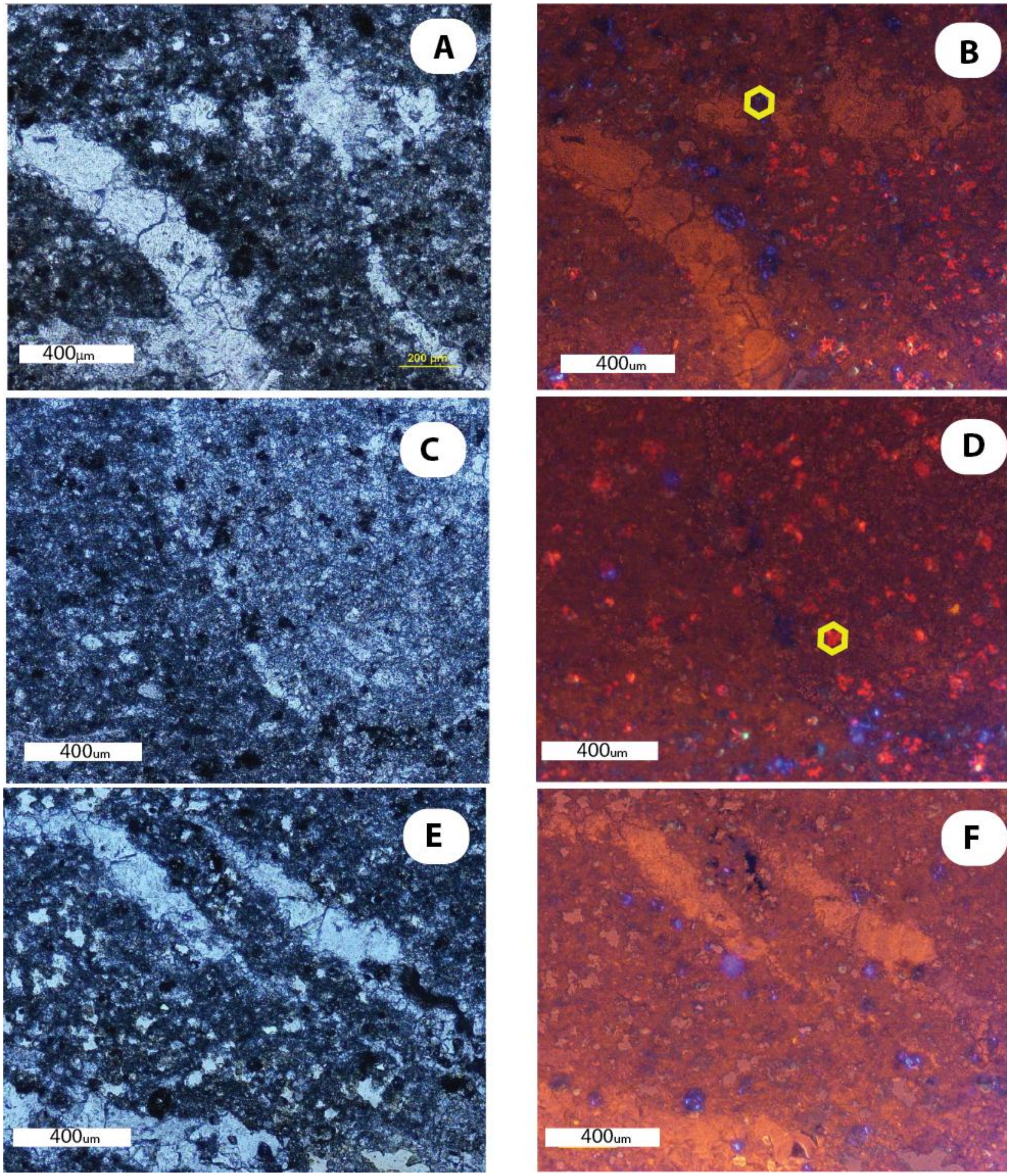

Figure 24. PPL and SEM-CL images from location 1 (forelimb). Each pair of PPL images to the left and SEM-CL images to the right portray the same location under the scope. Yellow polygons are location where EDS measurements were taken. (a) PPL image showing two fractures with white fill and porous material with black fill; (b) SEM-CL image fractures show different generation of fill. Porous material shown in purple. Red grains appear to have different composition than host rock; (c) PPL image showing porous material and two different textures (burrowed vs. non-burrowed); (d) SEM-CL image displays the porous material and red grains with different composition than host rock. It does not show different textures; (e) PPL image showing echelon fractures that are at an angle relative to bedding; and (f) SEM-CL image showing echelon fractures with different signature than host rock.

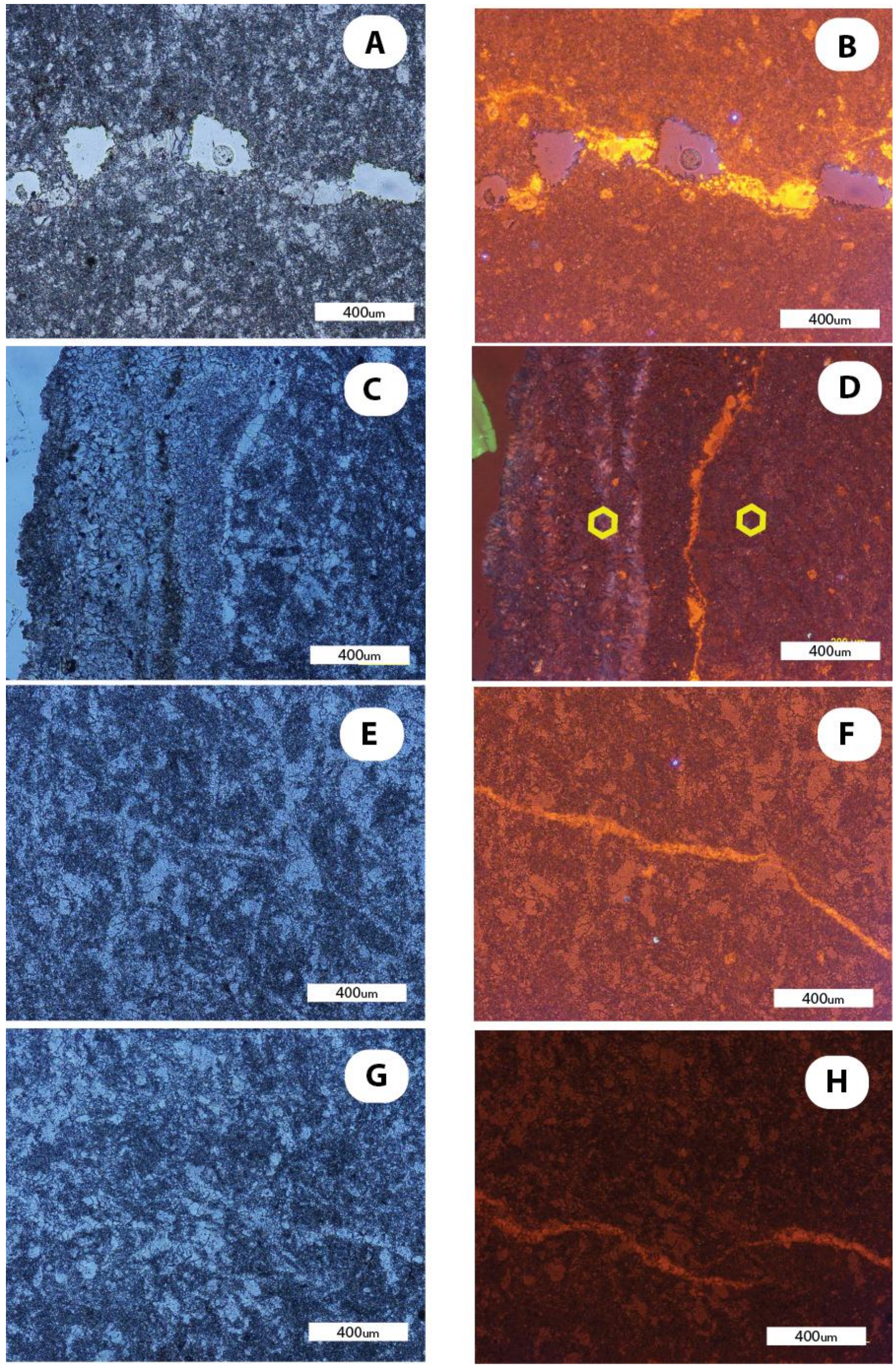

Figure 25. PPL and SEM-CL images from location (forelimb middle hinge). Each pair of PPL images to the left and SEM-CL images to the right portray the same location under the scope. Yellow polygons are location where EDS measurements were taken. (a) PPL image of sinuous fracture with open space; (b) SEM-CL shows sinuous fracture with open space and with different CL signature than host rock; (c) PPL image of weathering ring; (d) SEM-CL shows weathering ring and a fracture sub parallel to ring; (e) PPL image of host rock with no apparent fracture present; (f) SEM-CL image revealing cryptic fracture with different CL signature than the host rock; (g) PPL image of host rock with no apparent fracture present; and (h) EM-CL image revealing cryptic fracture with different CL signature than the host rock.

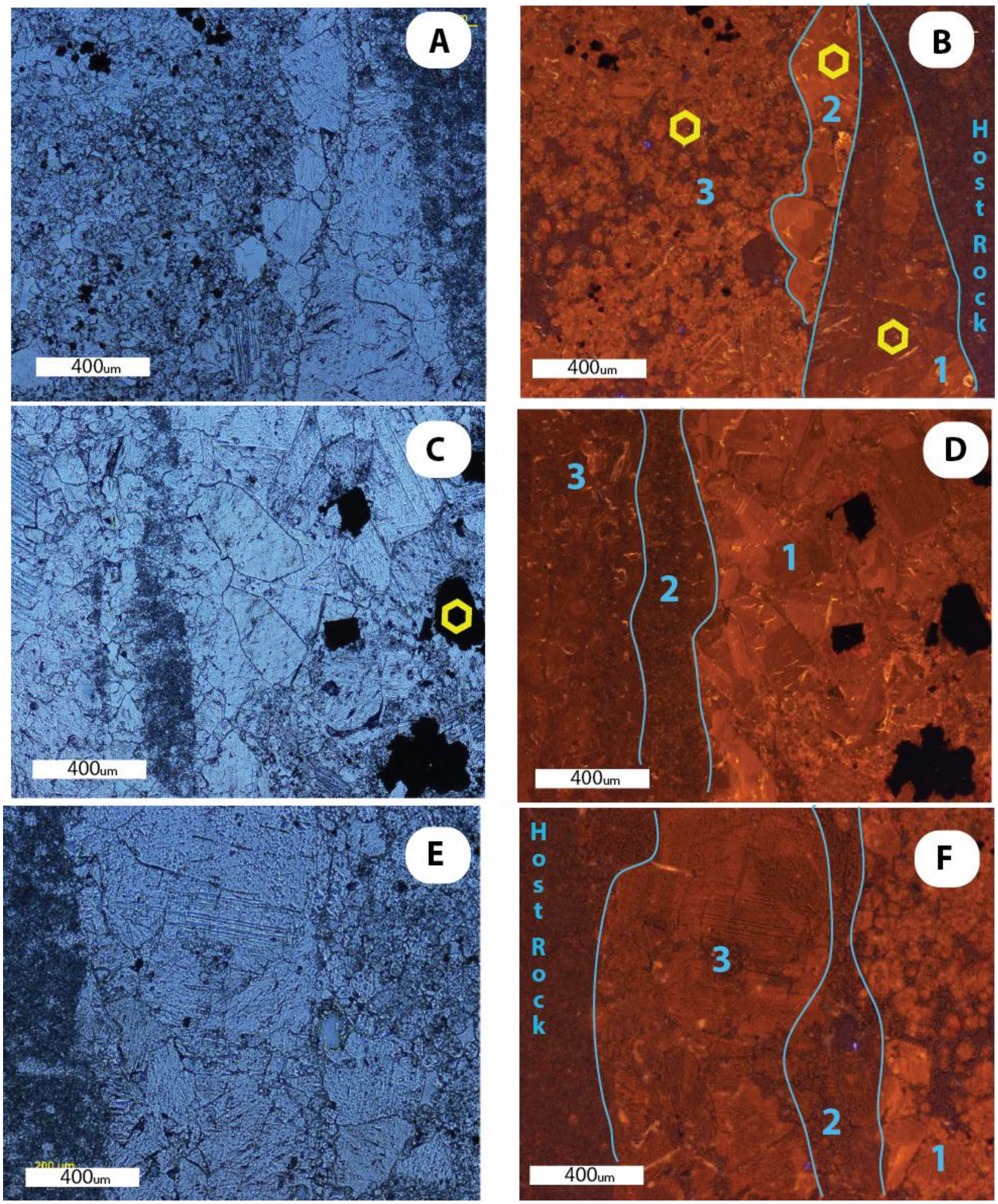

Figure 26. PPL and SEM-CL images from location 3 (Middle Limb). Each pair of PPL images to the left and SEM-CL images to the right portray the same location under the scope. Yellow polygons are location where EDS measurements were taken. (a) PPL image showing three generations of crystal growth within a fracture. (b) SEM-CL signature also shows three generations of crystal growth. (c) PPL image shows three generations of fill with pyrite crystals on black (d) SEM-CL image shows different signatures for each generation of fill. (e) PPL image showing three generations of crystal growth within a fracture. (f) SEM-CL image shows different signatures for each generation of fill.

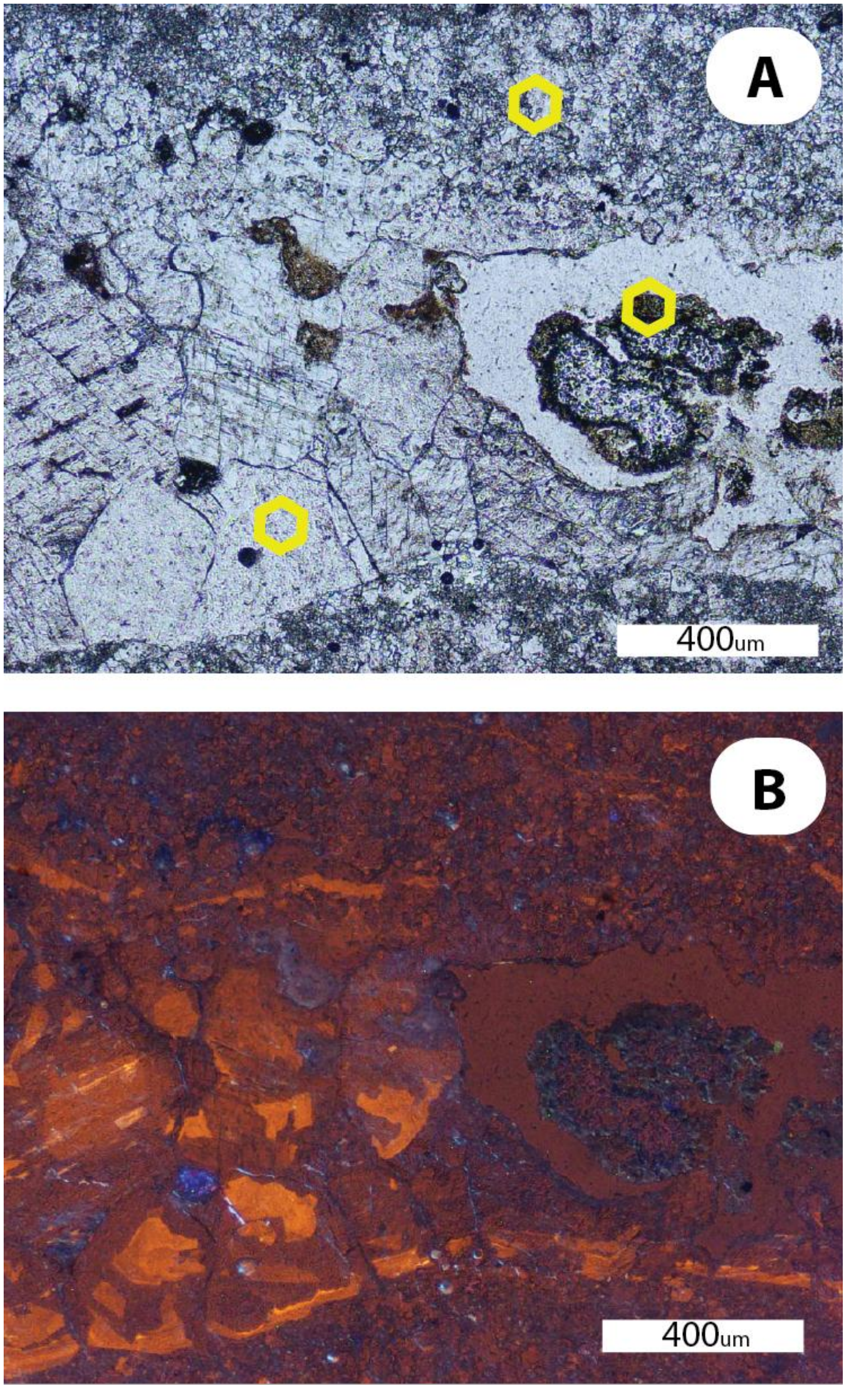

Figure 27. PPL and SEM-CL images from location 4 (middle-backlimb hinge). Each pair of PPL images to the left and SEM-CL images to the right portray the same location under the scope. Yellow polygons are location where EDS measurements were taken. (a) PPL image showing thick fracture with open pores (b) SEM-CL image of thick fracture with calcite crystals that show evidence of zoning.

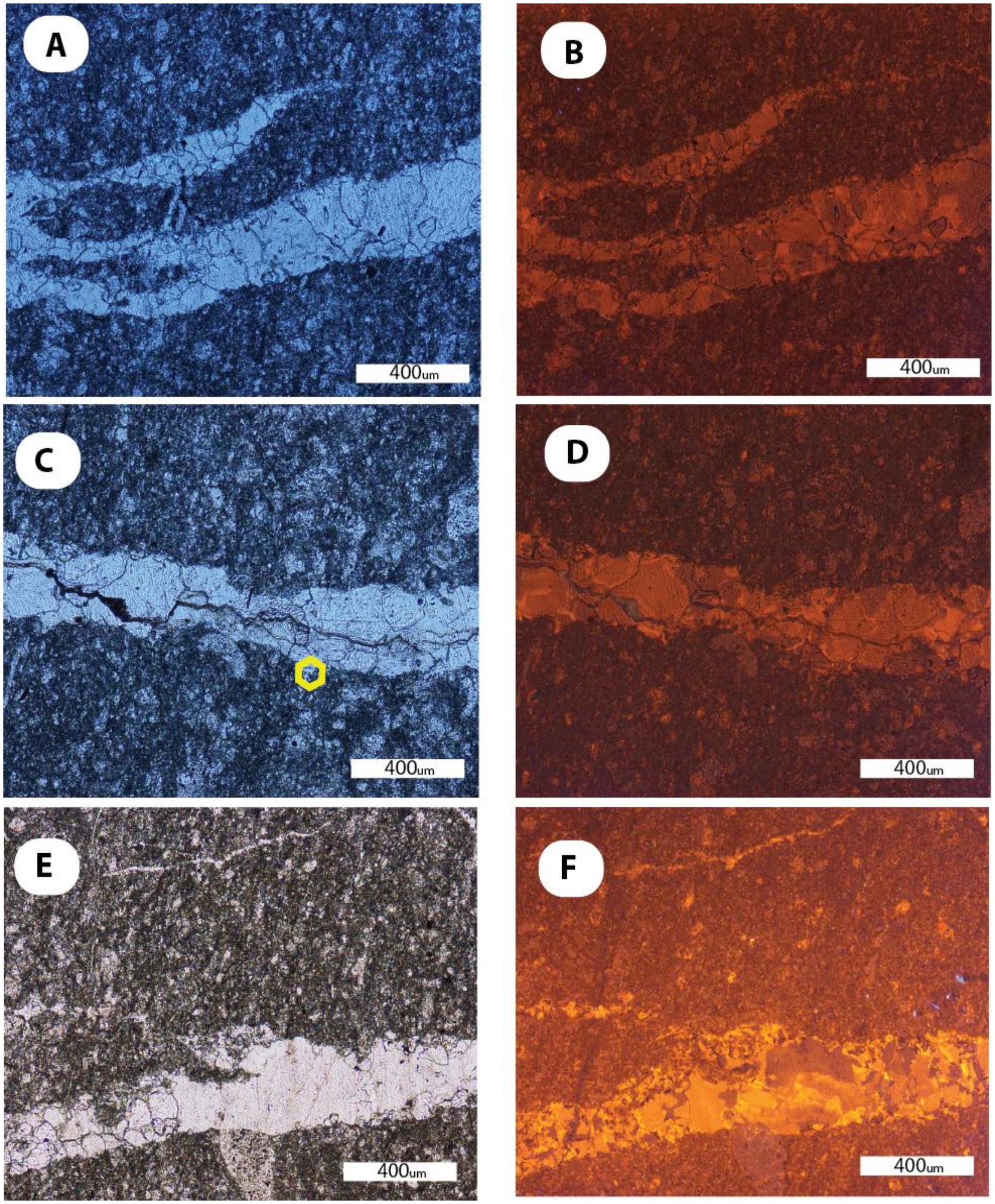

Figure 28. PPL and SEM-CL images from location 5 (backlimb). Each pair of PPL images to the left and SEM-CL images to the right portray the same location under the scope. Yellow polygons are location where EDS measurements were taken. (a) PPL image 2 shows sinuous fractures with blocky texture (b)SEM-CL image shows that fracture has different signature than host rock (c) PPL image shows fracture with blocky sub-euhedral calcite crystal fill. Later fracture appears winds through larger fracture (d) SEM-CL shows fracture with zoned calcite crystals. Later fracture shows different CL signature than larger fracture (e) PPL shows fracture with two different textures (f)(g).

Scanning Electron Microscopy

I used a scanning electron microscope (SEM) in order to get a better understanding about the compositional characteristics of the fractures under analysis. The SEM uses a focused beam of high-energy electrons to generate signals at the surface of specimens. These signals are created by electron-sample interactions and can reveal information about morphology, texture, and chemical composition of the materials in a sample. All SEM elemental analyses were taken at 20 kilovolts and spot size of 6 µm with a FEI Nova NanoSEM 430 field-emission SEM. Mineral identifications and phase identification maps were made using a Bruker XFlash® SDD energy dispersive spectroscopy (EDS) system that operates under a vacuum. All measurements were taken at the SEM lab of the Bureau of Economic Geology in Austin, TX.

I also used backscattered electron (BSE) imagery to obtain information about the mineral content of both fracture fill and the host rock adjacent to fractures. Interaction of an accelerated electron beam with a sample produces a variety of elastic and inelastic collisions between electrons and atoms within in a sample. Since the number of backscattered electrons reaching a detector is proportional to the mean atomic number of the sample, variations in brightness can be loosely correlated with variations in elemental composition.

The interaction of an electron beam with a sample produces not only a variety of collisions but also the emission of photons (including x-rays). I used an energy dispersive detector to separate the characteristic x-rays of different elements into an energy spectrum and to determine the relative abundance of elements in the analyzed sample. Moreover, I used the EDS system to create high-resolution element maps across an important location on one thin section (Goldstein, 2003).

Sample positions for SEM analysis were guided by host rock and fracture features observed in optical CL images. Results showed that the host rock and fracture fill were predominantly calcium rich, consistent with calcite, and also included magnesium, aluminum, silicon, and iron at some locations. Although backscattered electron (BSE) images reveal some compositional and textural variations, energy dispersive spectrometry (EDS) provided more detailed data about the presence or absence of elements in fracture fill at each structural position.

Location 1 Forelimb

EDS graphs and BSE images for location 1 showed a calcium-rich peak for the host rock, and revealed various compositions and elements present in the primary fills and grains with different characteristics included in those fills. EDS of porous material indicates that this material is calcium and magnesium rich, suggesting a dolomitic composition (Figs. 29a, 29b; Figs. 24b and 24d). EDS also showed the presence of chert within the rock, with Figure 29c showing the Si peak from that location. Figures 30a and 30b show BSE images of the fracture, but these images do not reveal a significantly different BSE signature between the calcite-rich and chert-rich regions. Moreover, this location showed the presence of euhedral, rhomb-shaped dolomite crystals (Fig. 30c).

Location 2 Forelimb Hinge

EDS graphs from this location indicate a predominant calcium rich composition with no distinct change in composition between weathered and unweathered surfaces recognized under CL (Figs. 25 and 31a,b).

Location 3 Middle Limb

EDS graphs from this location are based on analyses of the host rock and the different generations of fracture fill observed in both thin section petrography and CL images (Fig. 26). All generations of fracture fill from this location display calcium peaks in EDS (Fig. 32a,b,c), and the dark eu-to sub-euhedral suspected pyrite crystals documented in both thin section petrography and optical CL reveal large Fe peaks (Fig. 32c). EDS element maps of multi-generational fracture fill were taken to document any variation in composition between the three distinct fracture fill generations. With the exception of the pyrite crystals, calcium, iron, manganese, sulfur and titanium were distributed in equal concentrations throughout the fracture fill (Fig. 33).

Location 4 Backlimb hinge

EDS graphs from location 4 also indicate predominantly calcium-rich composition of the host rock, fracture fills, and late, pore-filling crystallization (Fig. 34a,b). However, EDS analysis of the suspected organic material within the pore seen in CL (Fig. 27) shows a spectral signature with silicon, calcium, aluminum, magnesium and sulfur peaks, suggesting clay with minor authigenic pyrite (Fig. 34c).

Location 5 Back limb

No SEM data were collected at this location.

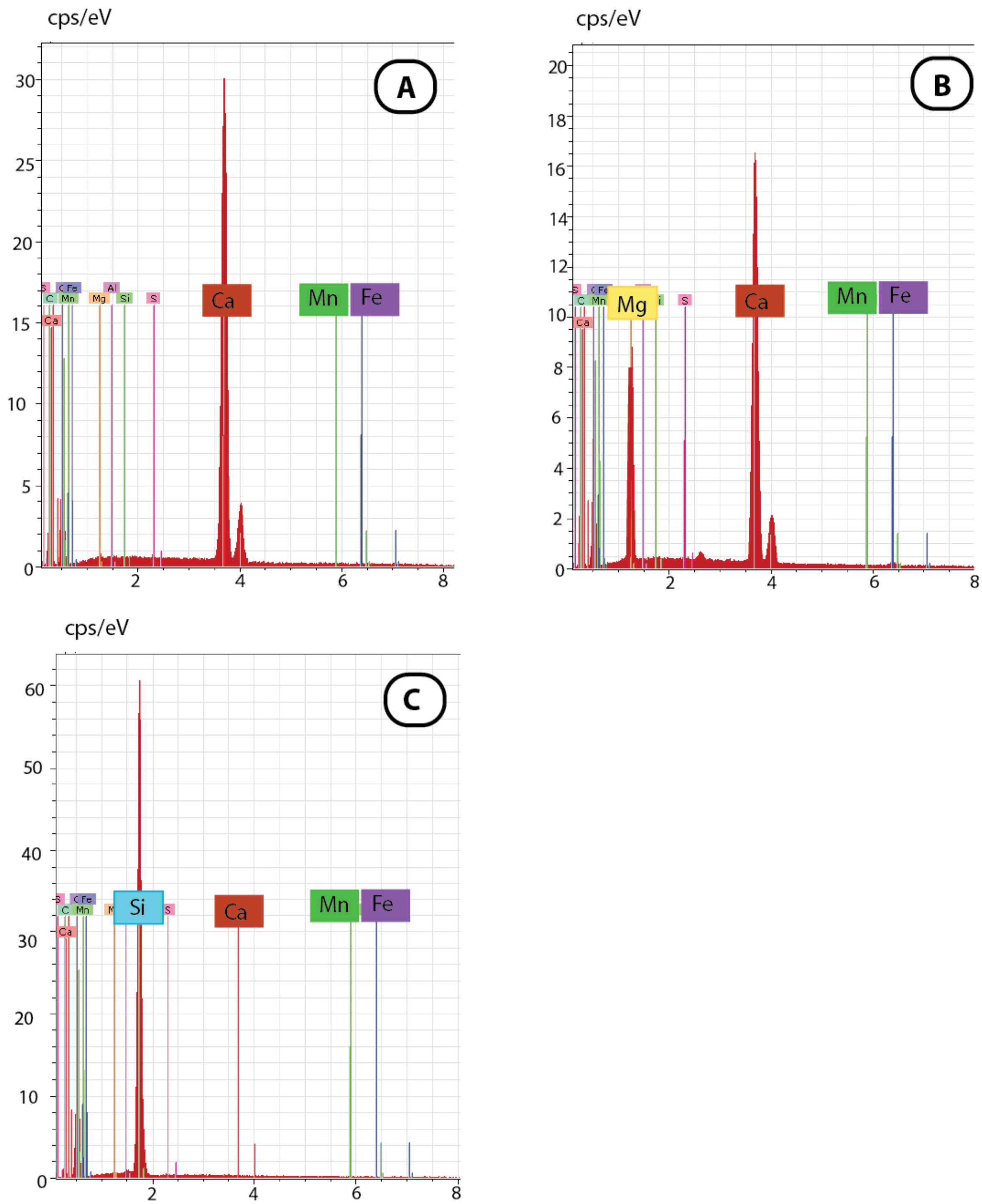

Figure 29. EDS elemental graphs obtained from sample in the forelimb. Data correlate with CL images in Figure 24. (a) Host rock ;(b) porous material, with the presence of significant calcium and magnesium suggesting dolomitic composition; and (c) Chert fracture.

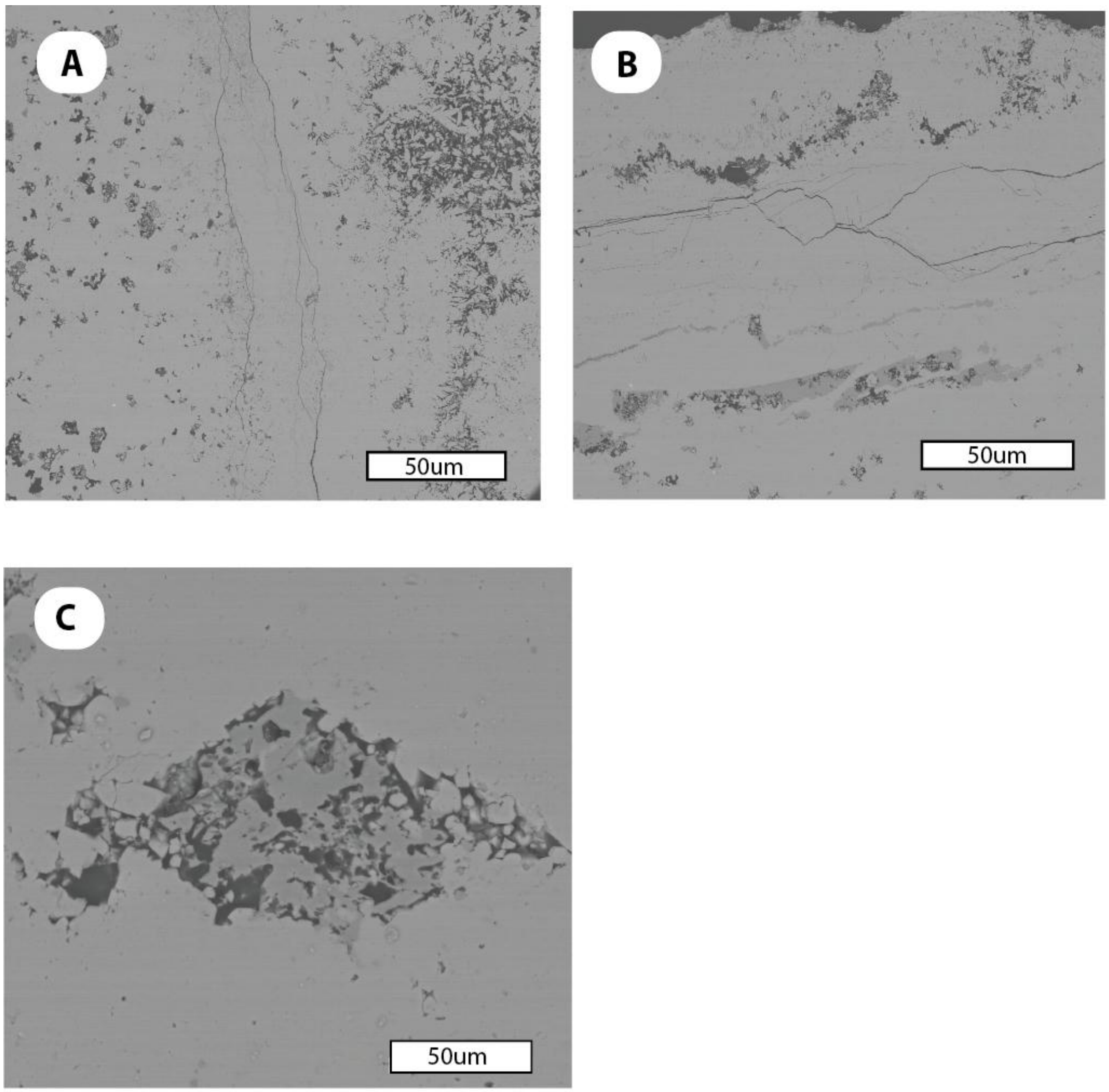

Figure 30. BSE images from sample obtained in the Forelimb. (a) thin chert fractures; (b) thin chert fractures; and (c) dolomite crystal rhomb.

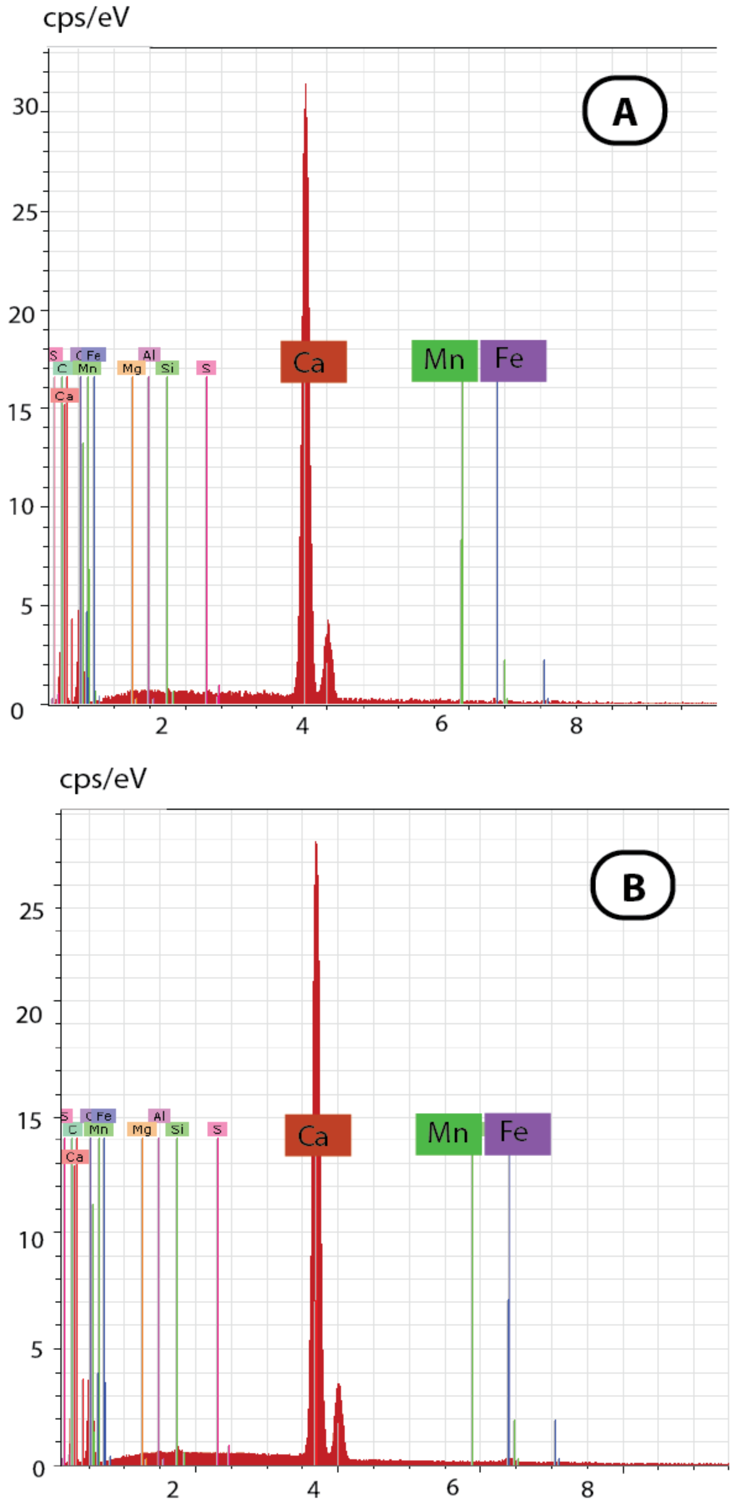

Figure 31. EDS elemental mineral graphs obtained from sample in the Forelimb hinge. Correlates with CL images in Figure 25. (a) weathered front showed in CL image; and (b) unweathered section.

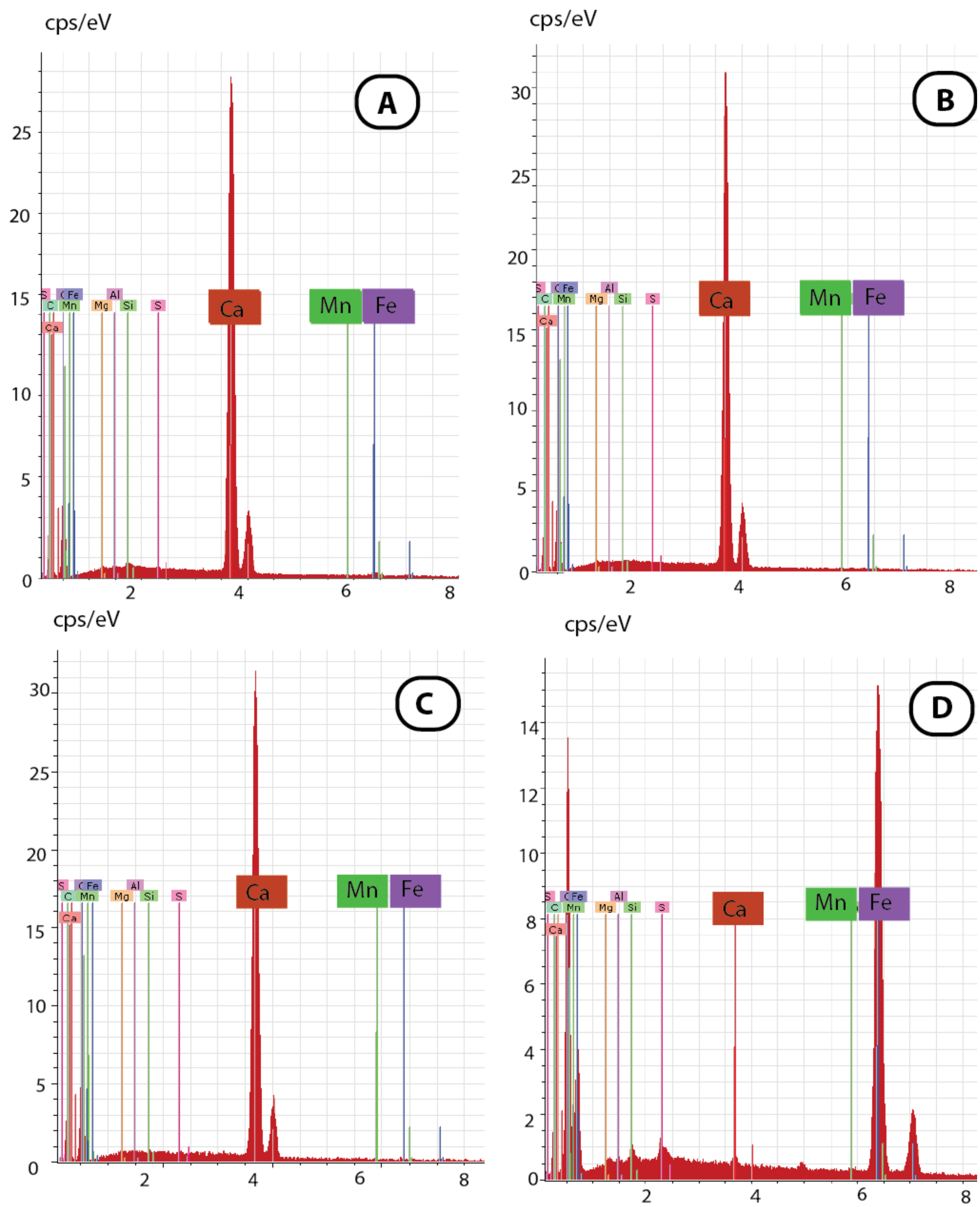

Figure 32. EDS elemental graphs from sample obtained in the middle limb; Correlate with CL image in figure 26. All measurement were taken from a single fracture with different generations of fracture fill. (a) blocky sub-to euhedral calcite crystals; (b) euhedral calcite crystals that appear to have nucleated on the fracture; (c)zone of smaller calcite crystals; and (d) black pyrite crystals.

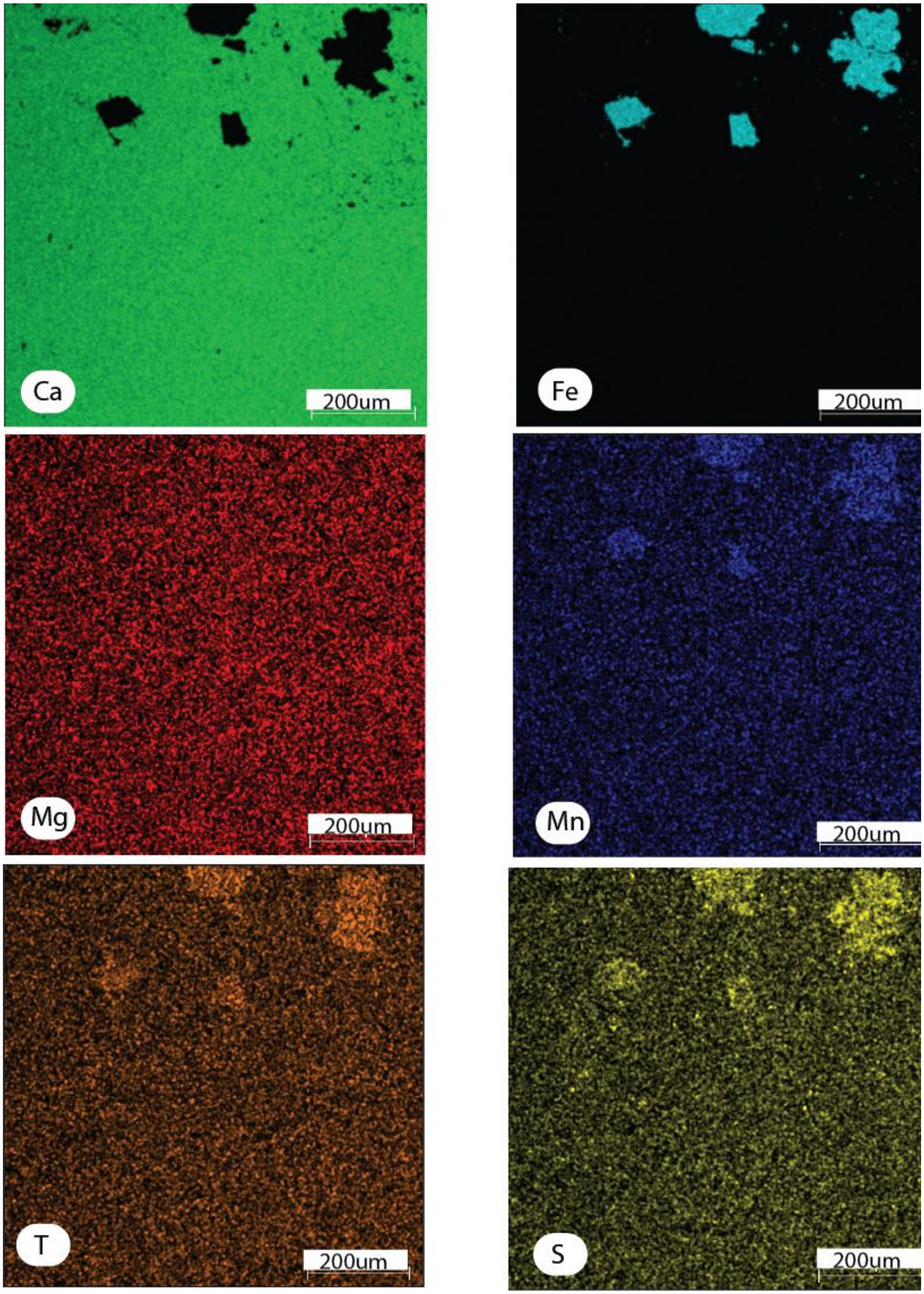

Figure 33. Element maps of calcium, iron, magnesium, manganese, titanium and sulfur from fracture observed at location 3. Pyrite crystals in the upper right corner of all maps, with the exception of magnesium, show different percent content of each material in comparison with host rock. No other significant differences were observed at other locations on these maps.

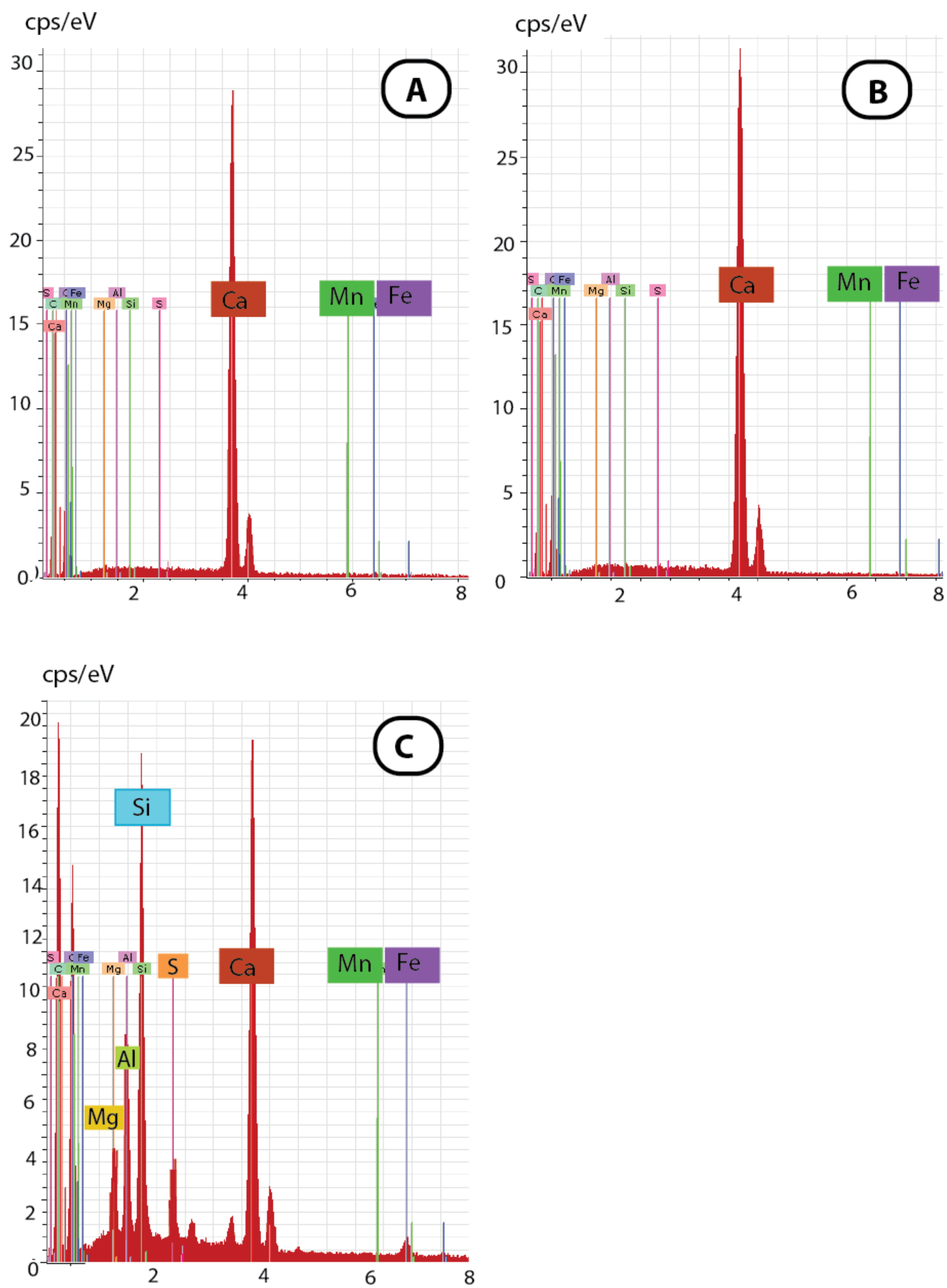

Figure 34. EDS elemental graphs from sample obtained in the backlimb hinge. These data correlate with CL images in Figure 27. (a) Host Rock; (b) calcite fracture; and (c) filled pore within a fracture.

IV. ANALYSIS

Analysis of fracture variables

The most common approach to compare parameters (variables) of multiple populations (in this case, structural position location) is by calculating the differences in means and/or medians. Although this method can provide information about the variability of each parameter in different populations, a more in-depth statistical analysis is required to evaluate the significance of such variability. I performed a significance test for fracture length and fracture aperture data in order to statistically evaluate the difference between parameters' medians at each structural position. In this significance test, the null hypothesis is that there is no significant difference in the medians of each parameter within different populations. The alternative hypothesis is that there *is* a statistical difference in the medians of each parameter within different populations.

Normality Test

In order to choose the appropriate significance test, one must first test whether or not each variable follows a normal distribution. I used two graphical approaches to check for normality. I compared histograms of each variable to the shape of a normal probability curve (Fig. 35a). If a quantity follows a normal distribution, the empirical distribution of the histogram should be symmetrical and bell-shaped. However, histograms suggest that all distributions are right-skewed (Figs. 35a and 35b), indicating that these data fail to follow normal distributions.

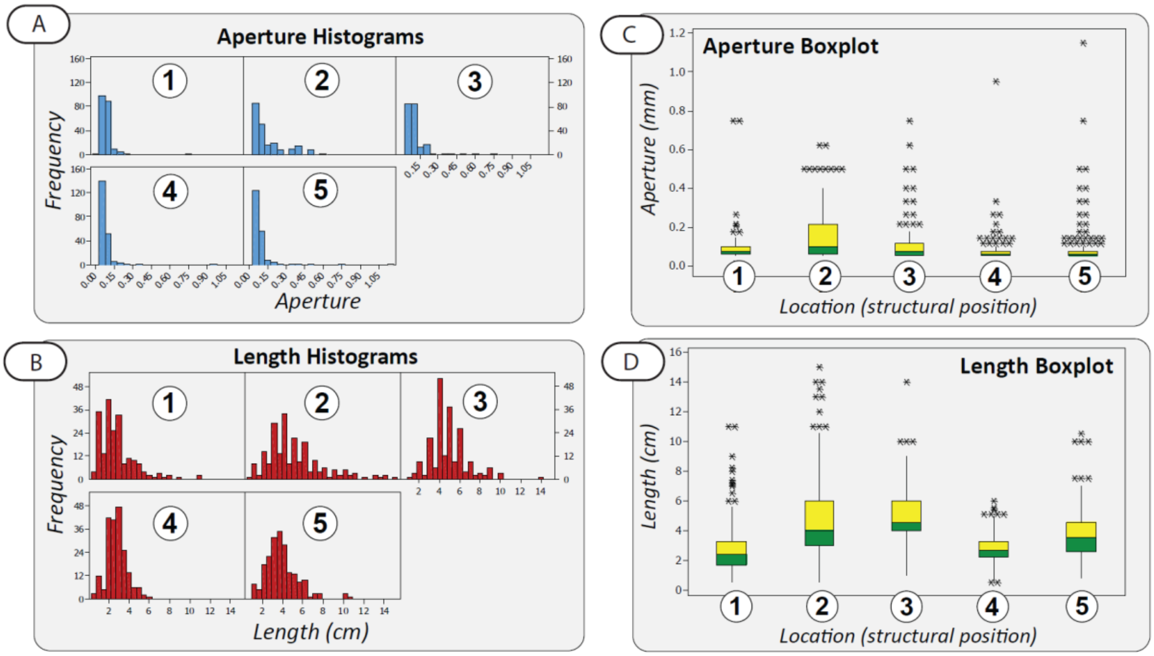

Figure 35. Graphical methods to test normal distributions. Location numbers correspond to structural positions discussed in the text. (A) Histograms of aperture data. Graphs show right skewed distributions in all five locations; (B) Histograms of fracture length data. Graphs show with right skewed distributions in all five locations; (C) Box plots of aperture data. At all location data results in asymmetrical boxplots; and (D) Box plots of fracture length data. At all location data results in asymmetrical boxplots.

I also used box-and-whisker diagrams to divide the data into quartiles based on the median of each parameter (Figs. 35c and 35d). The median for each dataset is indicated by the black center line between yellow and green areas, and the first quartile is indicated by the black line at the edges of the green area and third quartiles by the edges of the yellow area. The distance between these two lines is known as the inter-quartile range (IQR). The extreme values (within 1.5 times the IQR from the upper or lower quartile) are the endpoints of the lines extending from the IQR. All points at a greater distance from the median than 1.5 times the IQR are plotted individually as asterisks and represent potential outliers. Variables with normal distributions should have green and yellow quartiles of equal length above and below the mean. The box plots for aperture and length show that quartiles are not of equal length and therefore do not follow a normal distribution (Figs. 35c and 35d). Instead, the distribution for each variable at the different locations is right-skewed.

Two variable analysis: Kruskal – Wallis One-Way Analysis of Variance by Ranks

Kruskal - Wallis analysis is a non-parametric method for testing whether there is a significant difference among populations' medians. The test is appropriate for this study because it does not require a normal distribution, and it does assume the same shape (e.g., right-skewed) and scaled distribution (similar total population per location) for each group of samples (Gibbons and Chakraborti, 2003). Under these conditions, this statistical analysis provides a valid test of the null hypothesis that all medians are equal.

I used statistical and process management software known as Minitab to compare k number of random samples. For each variable, aperture and length, I used a k value of 5 (five different structural positions). Minitab first combines and ranks all the data, finds the group mean rank, and then standardizes the absolute difference of these average ranks.

The following summary of the mathematical theory behind Kruskal-Wallis analysis is from Nonparametric Statistical Inference (Gibbons and Chakraborti, 2003).The median test for k samples uses information about the magnitude of each of the N observations relative to a single number, which is the median of the pooled samples. Therefore, Minitab combines the N observations into a single ordered sequence from smallest to largest, keeping track of which observation is from which sample, and assigns the rank 1,2,…,N to the sequence. If ranks are well distributed among the k samples, which would be true for a random sample of a single population, the total sum of the ranks, $\sum_{i=1}^{N} i = N(N+1)/2$, would be divided proportionally according to the sample size among the k samples. For the i^{th} sample which contains n_i observations, the expected sum of the ranks is calculated by:

$$\frac{n_i}{N}\frac{N(N+1)}{2}=\frac{n_i\,(\mathrm{N}+1)}{2}$$

If the null hypothesis is true (all medians are equal), then the expected rank for any observation is the average rank (N+1)/2, and for n_i observations, the expected sum of ranks (R_i) is n_i(N+1)/2.

The Kruskal – Wallis analysis is based on a function of the deviations between the observed and the expected rank sums, with the reciprocals of the respective sample sizes used as weights. Thus, the Kruskal-Wallis statistic is defined as:

$$H=\frac{12}{N(N+1)}\sum_{i=1}^{k}\frac{1}{n_i}\left[R_i-\frac{n_i(N+1)}{2}\right]^2$$

The rejection region is calculated by H ≥ X_{k-1}^2.

In order to reject the null hypothesis, the computed value H= X^2 must be equal to or greater than the tabled critical chi-square value at the pre-specified degrees of freedom k-1.

A total of 1036 aperture and 1037 length values were used in testing. The results for both aperture and length data reveal a p value of 0.000. Therefore, the null hypothesis can be rejected. Most authors refer to a significant standard as $P < 0.05$ and statistically highly significant as $P < 0.001$ (less than one in a thousand chance of being wrong) (Graham, 2003). Since the p value is lower than 0.001, there is strong evidence that both aperture and length medians are significantly different across all locations Table 5.

Table 5. Kruskal Wallis Results

Aperture K-W test results

location	N	median	Ave. Rank
1	204	0.075	515.8
2	214	0.095	634.8
3	208	0.075	570
4	205	0.062	424.2
5	205	0.062	441.8
Overall	1036		518.5

DF = 4 P = 0.000 (adjusted for ties)

Length K-W test results

location	N	median	Ave. Rank
1	204	339	339
2	215	658.6	658.6
3	208	706.3	706.3
4	205	355.9	355.9
5	205	524.8	524.8
Overall	1037		519

DF = 4 P = 0.000 (adjusted for ties)

Observation bias correction

In order to clearly identify fracture sets and to compare fracture intensity at different structural positions, I used a new multi-step method developed by Surpless (2013) to account for observational biases that are present in any outcrop-based observation. This method accounts for the different probability of sampling fractures due to the fracture orientations relative to the observational plane, and for the different probability of sampling fractures in reference to their orientations with respect to the rectangular observational surface area.

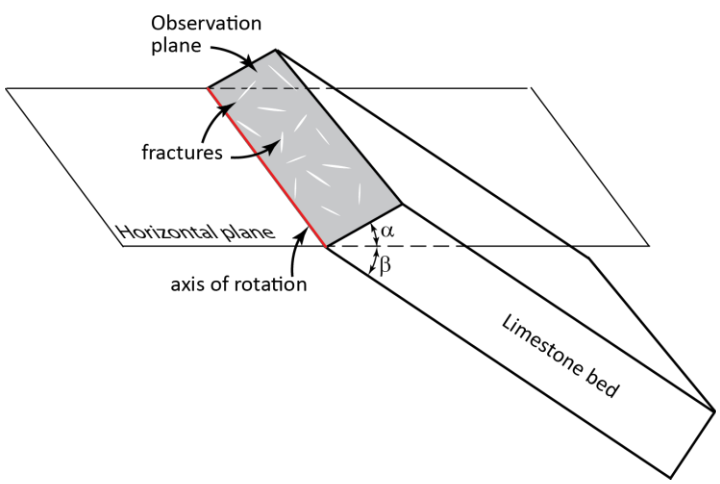

Figure 36. Angular relationships between the bed of interest, the observation surface, and horizontal. Prior to using bias correction methods, I first rotate all data about the axis of rotation indicated above (Following the method Surpless, 2013).

Prior to any bias

correction, all fractures were rotated about an axis parallel to the strike of the bed of observation (angle α, Fig. 36). By rotating the observational plane to horizontal, the post-rotation dips of all fractures become the angle of the fracture relative to the plane of observation (values listed in Appendix B).

Observational bias due to fracture orientation relative to the observational plane

I used the Surpless (2013) weighting system to account for observational bias due to fracture orientation relative to the observational plane. Unlike previous methods, this new approach does not multiply a predefined range of data by a single rating factor as described in background. Instead, the method developed by Surpless (2013) uses a function to weight fractures without any binning procedure.

First, the method uses the sine function relationship between an observed fracture at an angle of δ relative to an observational plane and the apparent spacing, d_A, relative to the true fracture spacing, *d* (Fig. 37):

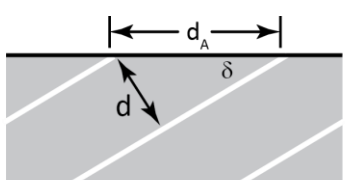

Figure 37. Angular relationship between a given fracture and the observation surface. Abbreviations: d = true fracture spacing; dA = apparent fracture spacing; and d = angle between observation surface and fracture.

$$\sin\delta = \frac{d}{d_A} \quad \text{eq. (1)}$$

The only angle at which d = d_A occurs at δ = 90°. Therefore, the fraction d / d_A is 1 at that angle. At angles below 90°, the rating factor increases with decreasing δ value to account for the smaller probability of fractures at small angles intersecting the observation plane. To address this problem of reduced probability of intersecting the observation plane, Surpless (2013) uses the fact that the fraction d_A/d increases at a rate proportional to the reciprocal of sin δ:

$$\frac{d_A}{d} = \frac{1}{\sin \delta} \qquad \text{eq. (2)}$$

Thus, rating factors can be based on the reciprocal of sin δ (Table 6). Nevertheless, this relationship cannot be used for all fractures because as δ approaches to zero, 1 / sin δ approaches infinity.

Table 6. Angle intervals and calculated rating factors based on 1/sin δ.

Angle (δ) between fracture and observation surface	Rating factor (f_i)
90°	1
89°	1
85°	1
80°	1.02
70°	1.06
60°	1.15
50°	1.30
40°	1.56
30°	2.00
20°	2.94
10°	5.88
6°	9.57
5°	11.11
2°	33.33
1°	50

Since my observation surface was not perfectly planar, I was able to sample some fractures parallel or sub-parallel to the observation surface. Thus, if I were to use a rating factor based directly on the reciprocal of sin δ, we would introduce new bias to our results for fractures at low intersection angles. To avoid such error, Surpless (2013) recommends using a maximum rating factor ($\boldsymbol{f_{1i}}$) of 11, which includes any fractures at angles of 5° or less relative to the plane of observation. For all other angles, I assigned rating factor based on the reciprocal of sin δ relationship.

$$\text{For } 0° \leq \delta \leq 5° : \boldsymbol{f_{1i}} = 11 \quad \text{eq. (3)}$$

$$\text{For } \delta > 5° : \boldsymbol{f_{1i}} = \frac{1}{\sin \delta} \quad \text{eq. (4)}$$

All post-rotation δ values (after the observational plane is rotated to horizontal) and the calculated weighting factors ($\boldsymbol{f_{1i}}$) for fractures calculated using equations 3 and 4 are listed in Appendix B.

Correction Method for bias due to observational plane shape

In order to avoid biases due to the shape of the observational plane, geologists attempt to use a circular observational area. However, due to bed characteristics, I could not obtain the requisite number of fractures within a circular area of a diameter equal to the thickness of the bed. Instead, I sampled fractures across a rectangular area, with one of the dimensions equal to bed thickness. Therefore, I corrected for this bias associated with the rectangular shape of the plane of observation using the Surpless (2013) method. This method consists of assigning a second rating factor ($\boldsymbol{f_{2i}}$) to each fracture based on its orientation relative to the observational plane.

In the program StereoStat, all data were rotated to an angle α about a horizontal axis (Fig. 36). Following Surpless' (2013) methods, I also rotated this observation area about a vertical axis an angle θ degrees, so that λ_2 is at 0° (Fig. 38). Appendix B shows the results of the rotation of all fractures. Once all data were rotated, I used the new strike value (S_r=

post-rotational strike value for a given fracture) for each fracture to calculate its probability of intersecting the observation area, based on the length of the line perpendicular to the fracture. This means that a fracture with a strike value of 000° would have the lowest probability of intersecting the observation area, while a strike value of 090° would have an intermediate probability of intersecting the observation area (Fig. 38). The rating factor $\boldsymbol{f_{2i}}$ was based on the relationship:

$$f_{2i} = \frac{\lambda_3}{\lambda_u} \text{ eq. (5)}$$

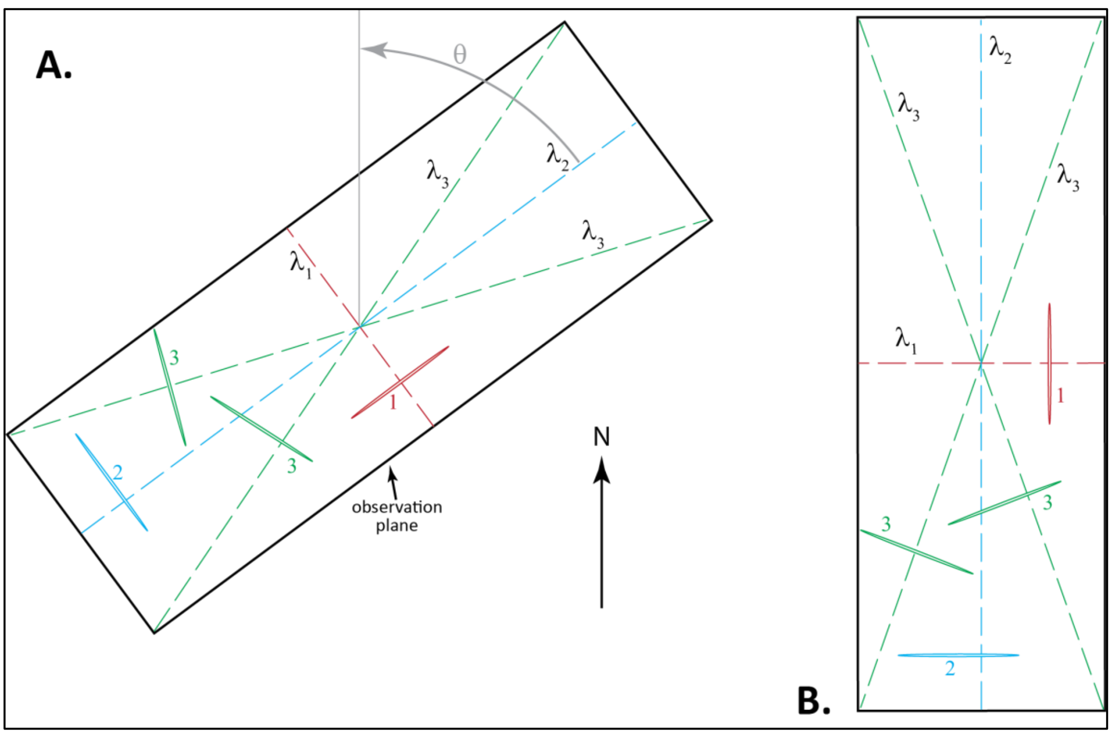

Figure 38. A. Hypothetical map view of the rectangular observation plane after the plane has been rotated to horizontal but before the observation area has been rotated in map view. The black outlined area represents the area of observation. In this example, fracture 1 would have the smallest probability of being observed based on the length of the line along which that fracture could intersect the observation area, λ_1; fracture 2 would have an intermediate probability of being observed based on the length of line λ_2; and fractures oriented in either #3 orientation would have the highest probability of being observed, based on the length of λ_3. All fractures will be rotated an angle θ about a vertical axis so that λ_2 is parallel to due north (0° azimuth). **B.** Post-rotation view of the observation area and fractures, with λ_2 parallel to due north. The plane of observation was rotated θ degrees (shown in A.) (Surpless, 2013).

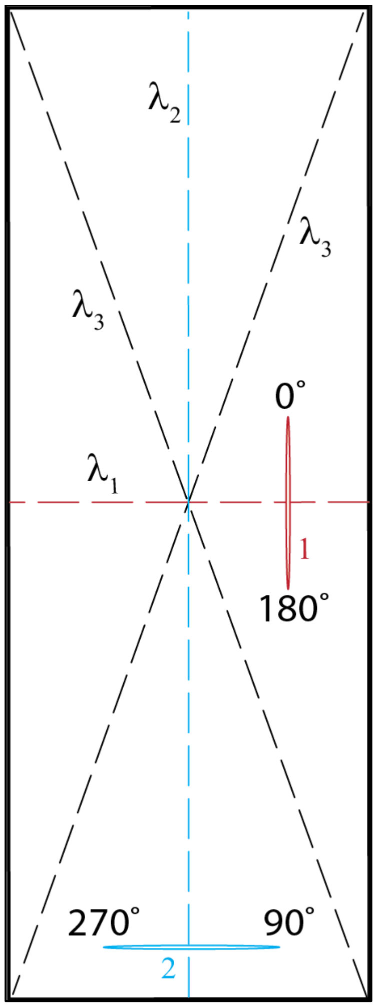

Figure 39. Apparent strike values (S_a) and corresponding length values for fractures of 0°, 90°, 180°, and 270°. Fractures in position 1 (red) would have λ^1 observation length while fractures in position 2 (blue) would have λ_2 observation length (Surpless, 2013).

Where λ_3 is the maximum length of a line of intersection on the observation plane and λ_u is the calculated length for a fracture of a given strike. Based on this relationship, when $\lambda_u = \lambda_3$, where λ_u is the calculated observation length for a given fracture, the rating factor $\boldsymbol{f_{2i}}$ is 1, while any λ_u shorter than λ_3 give a rating factor greater than 1.

For apparent strike values (S_r) of 0°, 090°, 180°, and 270°, the rating factors were fixed and based on the dimensions of the area of observation (λ_1 and λ_2; Fig. 39). Fractures in orientation 1 with strike values of either 0° or 180° have an observation length of λ_1, while fractures in orientation 2 have an observation length of λ_2. Thus, the rating factors for fractures of these positions become:

At 0° and 180° S_r values: $f_{2i} = \frac{\lambda_3}{\lambda_1}$ eq. (6)

At 90° and 270° S_r values: $f_{2i} = \frac{\lambda_3}{\lambda_2}$ eq. (7)

For all other fractures, I calculated the observation lengths of λ_3. There are four apparent strike values at which fractures would have this observation length (Fig. 40). S_r values at these four positions were determined by the dimensions of the area of observation, λ_1 and λ_2. The first post-rotational strike orientation occurs when $S_r = \beta = \tan^{-1}(\lambda_2/\lambda_1)$ (Fig.40a). Since these angular relationships remain constant at the other S_r values, these S_r values were expressed in terms of β. In Figure 24b, S_r = 180 – β; in Figure40 c, S_r = 180 + β; and in Figure 40d, S_r = 360 – β. In all cases, β = $\tan^{-1}(\lambda_2/\lambda_1)$.

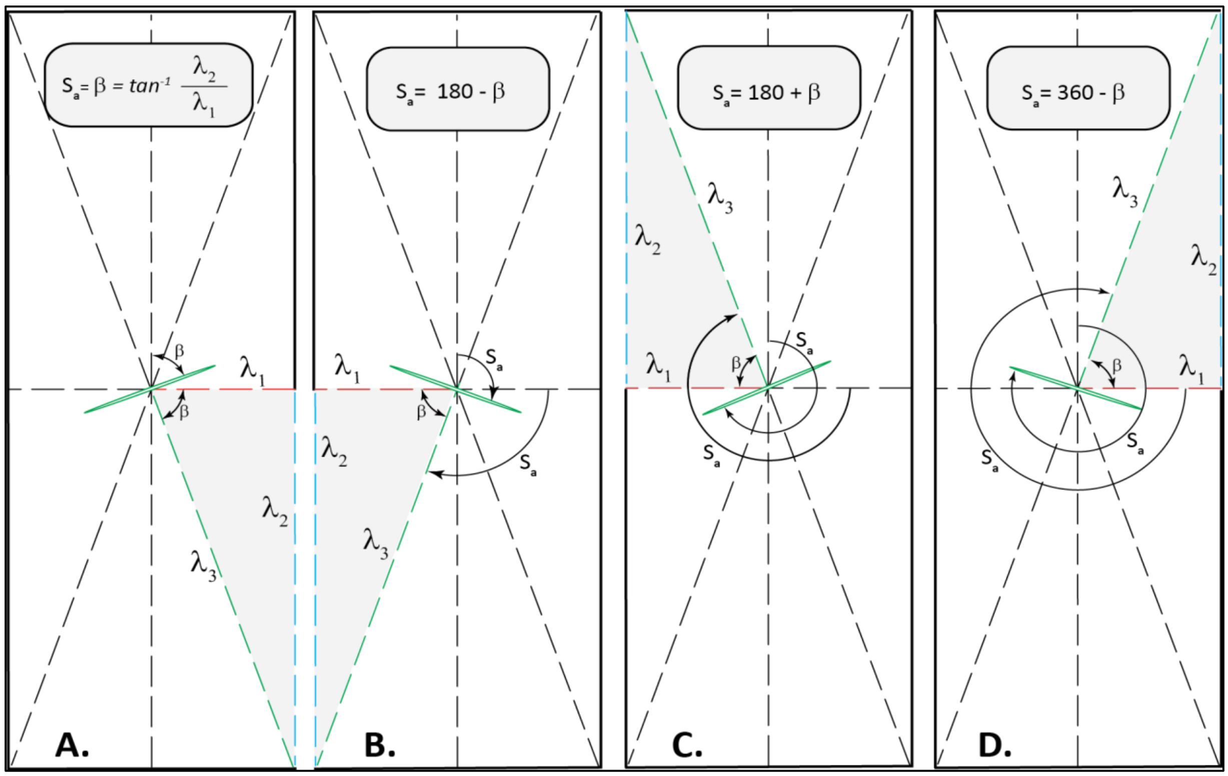

Figure 40. Four post-rotational strike (S_r) orientations at which a fracture would have observation length λ_3. **A.** The first S_r value, β, occurs when β = $\tan^{-1}(\lambda_2/\lambda_1)$. This value will vary based on the dimensions of the area of observation. **B.** The second S_r value occurs at 180 – β. **C.** The third S_r value occurs at 180 + β. **D.** The fourth S_r value occurs at 360 – β. See text for discussion (Surpless, 2013).

Following this method, I used a total of eight S_r values for which observation length and therefore rating factors (see eq. 5) are known for a given planar observation surface. For S_r values other than these, however, the observation lengths will vary according to different trigonometric functions. The range of values that lie between these known observational lengths values are indicated by the roman numerals I. through VIII. (Fig. 41).

These functions and the values for the known observation lengths are listed in Table 7, where λ_u is the observation length based on the post-rotation strike value (S_r).

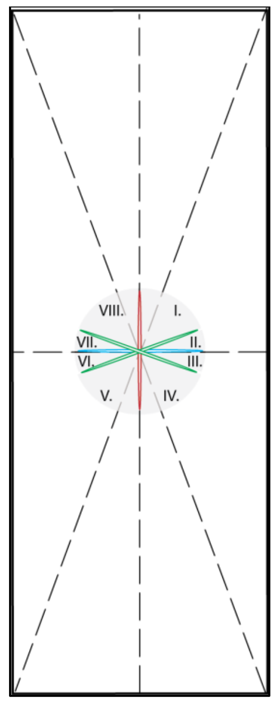

Figure 41 . Angular ranges for S_r values that lie between known observational lengths. Angular ranges I. through VIII. have different trigonometric functions that govern the lengths of observation.

Appendix B shows the new values after rotation and the final weighting factor.

Combination of the two weighting factors

With these relationships established for the orientation between the plane of the observation surface (rating factor f_{1i}) and the orientation of the fracture relative to the rectangular area of observation (rating factor f_{2i}), I calculated a complete weighting value for each fracture sampled by obtaining the product of the two rating factors:

$$f_{it} = f_{1i} \cdot f_{2i} \quad \text{eq. (8)}$$

Appendix B shows final results for all fractures at all 5 different structural positions.

Table 7. Summary of rating factors for fracture observations within a rectangular area, where S_r is the post-rotation strike value. Zones I. through VIII.

Angle(s)	*Observation length (λ_u)*	f_{2i}
0°	λ_1	λ_3/λ_1
Zone I: $0 < S_r < \beta$	$\lambda_u = \dfrac{\lambda_1}{\cos\ (S_r)}$	λ_3/λ_2
β	λ_3	1
Zone II: $\beta < S_r < 90°$	$\lambda_u = \dfrac{\lambda_2}{\cos(90 - S_r)}$	λ_3/λ_u
90°	λ_2	λ_3/λ_2
Zone III: $90° < S_r <$ [180° - β]	$\lambda_u = \dfrac{\lambda_2}{\cos(S_r - 90)}$	λ_3/λ_u
180° - β	λ_3	1
Zone IV: [180° - β] $< S_r <$ 180°	$\lambda_u = \dfrac{\lambda_1}{\cos(180 - S_r)}$	λ_3/λ_u
180°	λ_1	λ_3/λ_1
Zone V: 180° $< S_r <$ [180° + β]	$\lambda_u = \dfrac{\lambda_1}{\cos(S_r - 180)}$	λ_3/λ_u
180° + β	λ_3	1
Zone VI: [180° + β] $< S_r <$ 270°	$\lambda_u = \dfrac{\lambda_2}{\cos(270 - S_r)}$	λ_3/λ_u
270°	λ_2	λ_3/λ_2
Zone VII: 270° $< S_r <$ [360° - β]	$\lambda_u = \dfrac{\lambda_2}{\cos(S_r - 270)}$	λ_3/λ_u
360° - β	λ_3	1
Zone VIII: [360° - β] $< S_r <$ 360°	$\lambda_u = \dfrac{\lambda_1}{\cos(360 - S_r)}$	λ_3/λ_u

Post-weighting fracture orientation distributions

I created stereonet diagrams using StereoStat V1.5. I graphed weighted and unweighted strike and dip data from each structural position. I also plotted unrotated strike and dip and data rotated to horizontal with respect to bed orientation on equal-area stereo net diagrams (Fig. 42). I defined sets using contours with a one percent area contouring, a contour count of 5, an initial contour of 2 sigma and significant sigma of 3.

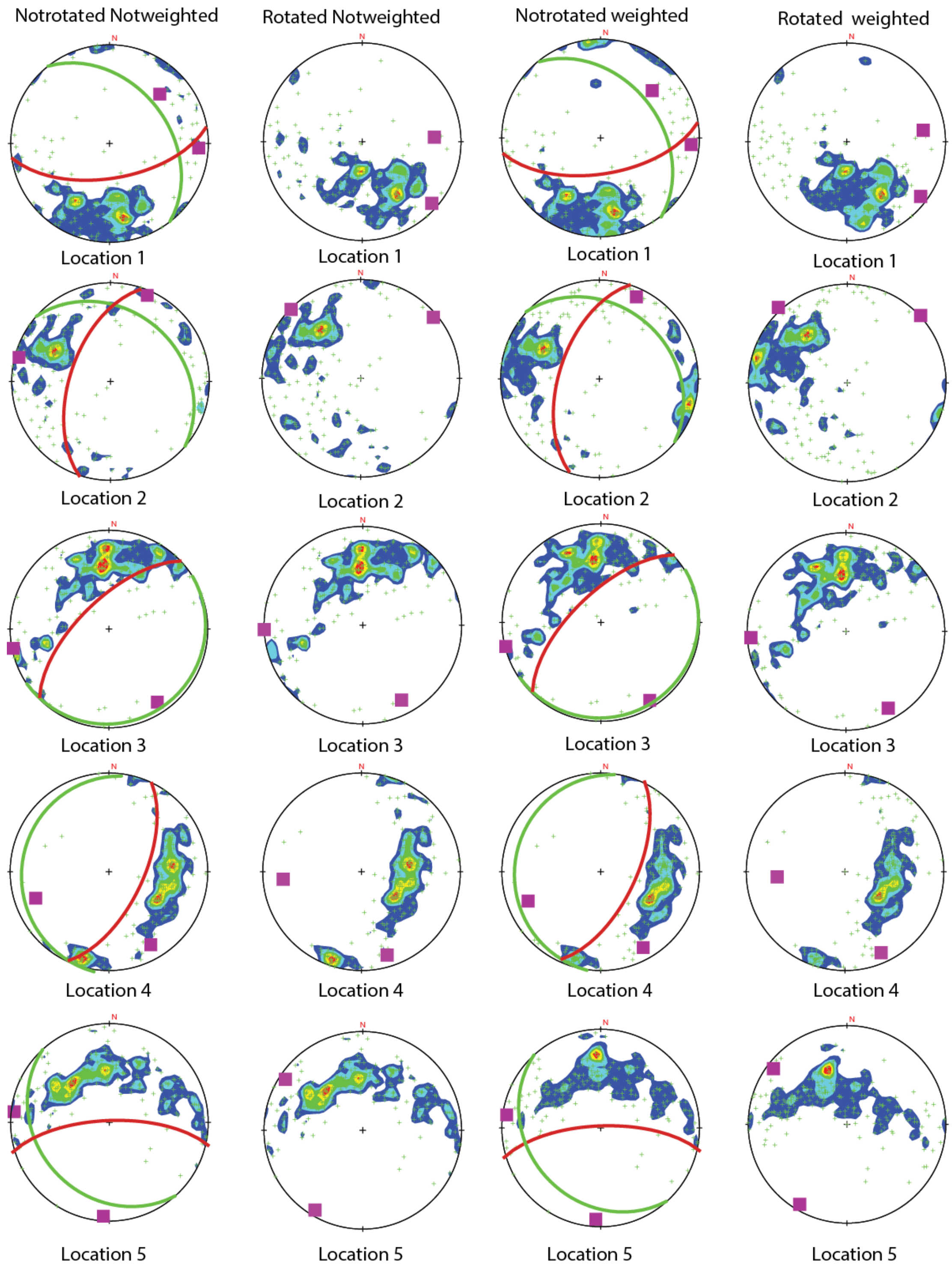

Figure 42. Stereo net diagrams with fracture orientation data and contours of high density regions. Red great circle is observational plane orientation and green great circle is bed orientation. Purple squares are major joint sets observed at each location. First column show raw fracture data. Second column shows fracture data rotated to horizontal according to bed orientation. Third column shows fracture data that has not been rotated, but that has been weighted for observational bias corrections. Fourth Column show fracture data that has been rotated to horizontal according to bed orientation and weighted for observational bias correction.

Fracture Intensity

I determined fracture intensity by calculating the number of fractures per centimeter measured on the observational plane, and I calculated the void space (aperture*length) as a percent of the observational surface area (Table 8). Fracture intensity was found to be significantly higher in the middle- backlimb hinge and forelimb positions, and mean aperture and length were lowest in these structural locations. Conversely, the lowest fracture intensity is the middle limb and middle-forelimb hinge position, and mean aperture and length were higher at these locations. Percent of possible void space was highest at the forelimb and lowest at the middle limb position. Thus, these results demonstrate an inverse relationship between fracture intensity and fracture length.

Table 8. Summary of statistical data

Location	Fracture Intensity (fractures/cm^2)	Mean Aperture (mm)	Average Fracture Length (cm)	Percent of Open Pore Space
Forelimb	0.853	0.087	2.806	20.719
Mid-Forelimb Hinge	0.230	0.151	5.003	17.343
Middle Limb	0.170	0.106	4.844	8.732
Mid-Backlimb Hinge	0.876	0.076	2.780	18.510
Backlimb	0.551	0.090	3.722	18.445

In order to quantify the relationships between fracture aperture to fracture intensity, I calculated the R^2 of each equation by obtaining the natural log of the aperture and intensity data in order to transform the exponential relationship into linear equations. Graphs of aperture and fracture intensity (Fig. 43) follow a power law distribution in all five locations, with fewer fractures having large apertures. R^2 values from linear regressions ranged from 0.69 to 0.92.

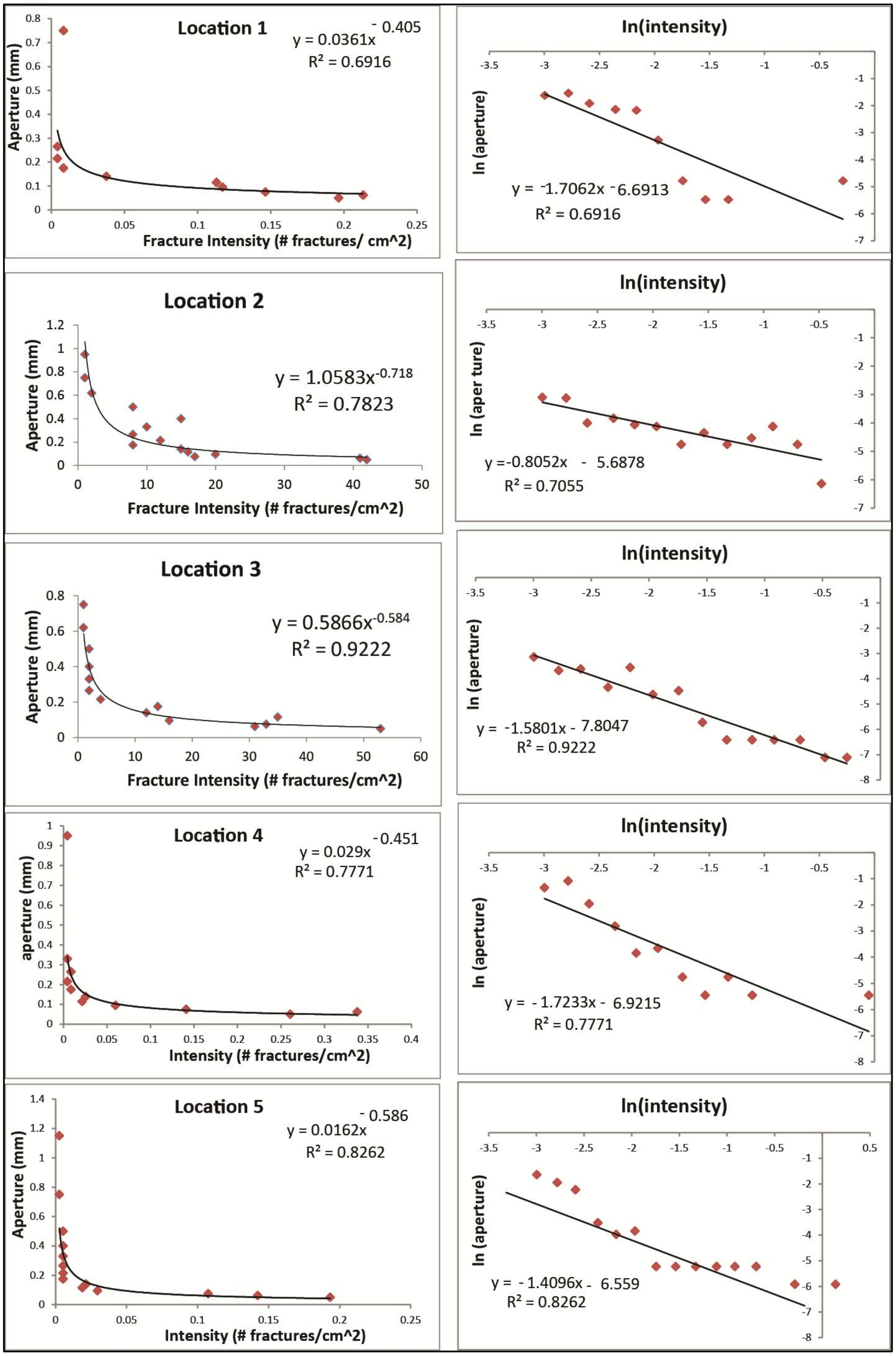

Figure 43. Relationship of fracture aperture and fracture intensity. Graphs to the left show aperture of fractures measured against the fracture intensity at each structural position of the Stillwell Anticline. Graphs to the right are linear regressions of fracture data at each structural position.

V. DISCUSSION

The micrite limestone bed traced across different structural positions in the Stillwell anticline contains significant intermediate-scale fracture systems at each location. Although optical imagery did not reveal the same fracture intensities as those observed in the field, it showed that fracture systems at all five locations have similar fracture morphology, fracture fill, and textures. In contrast, statistical analysis proved that fracture intensity, average aperture and length are significantly different at each structural position.

Other researchers have reported a lower visibility of fractures in optical microscopy. Laubach (1989) found that fluid inclusions in closed microfractures are sometimes composed of single, colorless, non-fluorescent phases. He concluded that fluid inclusions in both transgranular and intragranular planes surrounded by quartz represent an optical continuity with host grains and become invisible under the microscope (Laubach, 1989). The fractures observed in the Stillwell anticline limestone beds also contained similar mineral fill composition relative to the host rocks. As a result, there is a significant difference between optical microscopic and field visibility of fractures. Therefore, workers performing comprehensive fracture intensity studies of limestone should always collect data across a range of scales, from the microscopic to the macroscopic.

Thin section petrography and CL imagery showed that most fractures present in the Santa Elena limestone beds measured contained sub-to euhedral calcite crystals. This blocky texture suggests that veins were formed by crystallization within open fractures, rather than by crack seal mechanisms (e.g., Gale et al., 2008). Moreover, CL images revealed different generations of fracture fill. The temporally separate fill events suggest that the system was subject to changes in permeability due to both propagation events and fracture fill events. Therefore, the percent void space calculated at each structural position is likely a maximum that was never achieved during the life of the fracture-fluid system.

The results of the fracture intensity analysis indicate that fractures at an intermediate scale can be correlated with strain. Previous studies about strain rates in the Stillwell anticline indicate that the asymmetric fold should have maximum finite strain in the forelimb, a slightly lesser finite strain in the forelimb hinge and backlimb hinge, and very little, if any, fold-related strain in the middle limb of the system (Fig. 44; Mays et al., 2012). Strain at the forelimb is primarily accommodated by simple shear, while is more complex at the fold hinges. Data from this research reveal maximum fracture intensity at the forelimb hinge and backlimb hinge. These results imply that fracture systems at an intermediate scale are at least loosely correlated with the localized strain fields associated with fold deformation.

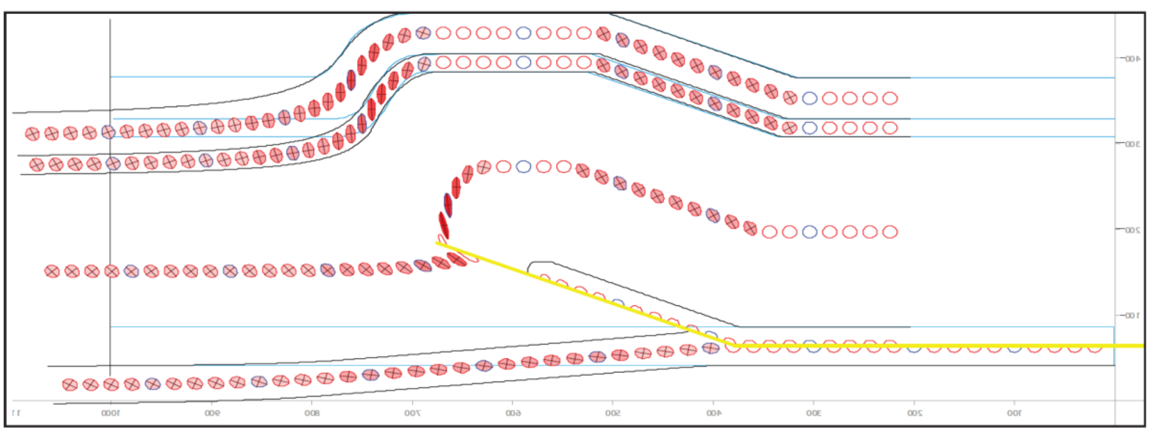

Figure 44. Kinematic best-fit foward model of the Stillwell anticline produced by Mays et al., 2012. Cross-section represented in blue. Fault is shown in yellow. Strain ellipses shaded with deeper red indicate greater strain.

Rock failure is the culmination of a progressive development of cracking during loading rather than a catastrophic spread of a single crack at a peak stress (Paterson and Wong, 2005). Therefore, even though composition, stratigraphic position, depositional environment and bed thickness were held constant, the type of failure observed in all five locations is not the same. Statistical analysis of fracture variables suggests that there is a significant difference between fracture length at all five locations (Table 5). For example, the longest average fracture length was measured at the forelimb location and the shortest average fracture length was at the forelimb hinge location. This variation implies that the progressive development of fractures is different at each structural position. In fact, length data comparisons to the kinematic model of the Stillwell anticline show that the location with greatest curvature has the shortest fracture lengths, while the location with greatest shear has the longest lengths. This relationship suggests that the local stress field is likely constantly changing in the hinge, while in the forelimb, the strain rate and orientation are much more consistent, permitting greater propagation of individual fractures.

Fracture intensity and aperture data reveal a power law relationship at each structural position, with greater fracture intensities correlated with narrower fractures. High R values (Fig. 43) support this relationship and indicate that populations of microfractures could be used to predict the intensity of macro fractures. This power law relationship has been previously described in the literature. Ortega et al. (2010) obtained even higher R values for power law relationships between aperture and fracture intensity.

However, other researchers suggest that the power law relationship between intensity and aperture is only valid within a certain range of fracture widths. Hooker et al. (2009) suggest that most power law distribution research has been based only on micro- to intermediate scale fractures. In their analysis of aperture-dependent fracture intensity, Hooker et al. (2009) incorporated data primarily from micro- and macro-fracture systems. Their results show that aperture-size data below a width of 0.012 mm and above a width of 1 mm follow a log-normal distribution. Intermediate-size fracture apertures, though relatively sparse in their study, suggest a power-law aperture-size distribution (Hooker et al., 2009). The results presented here support these findings and also suggest that the power law relationships obtained may not accurately predict smaller or larger fracture systems.

Fracture weighting procedures did not entirely remove observational bias. Research has shown that observational bias can be a result of bed orientation, and microfractures are generally perpendicular to bedding and are commonly subvertical (e.g., Laubach, 1989). Figure 42 shows that fracture orientations sampled here do correlate with bed orientation. Nevertheless, this relationship is not as strong as the correlation of each fracture systems with the observational plane. Therefore, I conclude that observational bias is still present after the weighting procedure. In order to properly weight fractures of lower sampling probabilities, the data must have at least one fracture that represents such orientations. If a data set completely lacks fractures of similar orientation to the observational plane, then no multiplier will be calculated for those fractures and observational bias will not be corrected.

Although the observational surface was not planar, the relief may have not been significant enough to permit the observation of at least one fracture from every orientation present.

Although fracture variables such as aperture, length, and intensity are influenced by strain rate and other factors, fracture orientations can commonly be tied to stresses related to tectonic activity (e.g., Fossen, 2010). Fracture sets present in the Stillwell anticline beds measured here show no clear correlation to the orientation of other structures in the area. Stereonets show that fracture sets have different orientations at all five structural positions. Even after rotation to horizontal, fracture sets at different locations do not appear to correlate with each other. Moreover, larger fracture systems and macroscopic, outcrop-scale joints sets do not show strong relationships (Fig. 42). None of the joint sets overlap with the high density fracture sets. This non-correlation between different fracture sets and joint sets shows that although fracture intensity, aperture and length values have strong relationships with the compressional deformation of the fold system, orientation appears to be independent of the tectonic activity in the area.

The significant variation in fracture orientations could imply greater rock permeability. The flow of fluids through rocks depends, in part, on fracture intensity and fracture connectivity. For fluid flow to occur in any particular fracture network there must be at least one interconnected sets of fractures. This condition is known as the percolation threshold (Fig. 45). Thus, the great variety of fracture orientations I documented could indicate the existence of interconnected fracture networks that reached a percolation threshold. Further research and characterization of connectivity could therefore help predict the rate and directionality of flow.

VI. CONCLUSIONS

The fracture weighting procedure did not completely remove observational bias from the data, which may have affected the analysis of fracture orientations in the system. Since information about fracture sets allows scientists to characterize fracture networks and their connectivity, it is imperative to develop better bias correction procedures. Until scientists find an accurate correction model, all fracture research should note that the results and observations may be affected by observational bias.

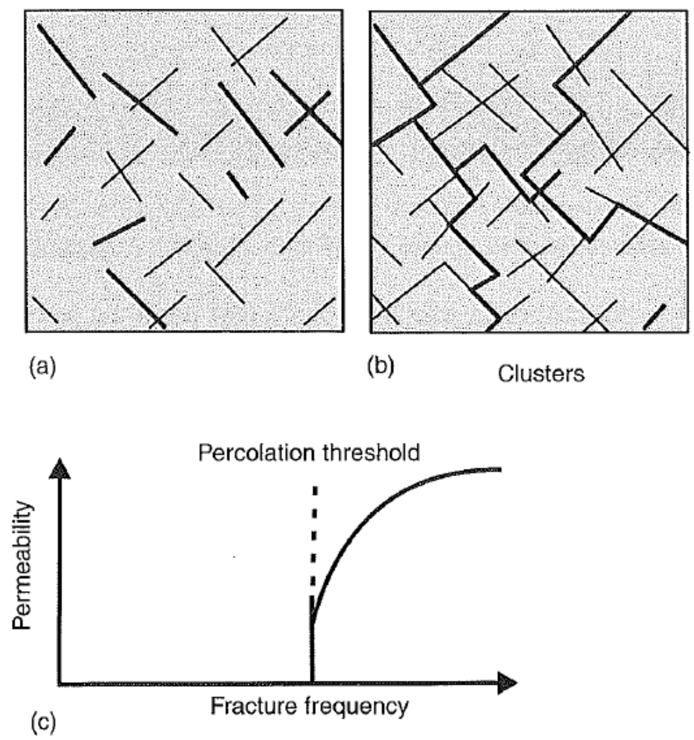

Figure 45. Fracture network connectivity. (a) Fracture network with poor connectivity; (b) Fracture network with high connectivity; (c) Percolation threshold is reached (Gudmundsson, 2011).

This research introduces a new field method that could be applied to the characterization of fracture systems in the subsurface. Fracture systems in the Santa Elena limestone beds measured are mostly composed of veins with multiple generations of calcite fill. The various stages of fracture fill suggest local changes in fluid source and indicate that the system has experienced significant changes in permeability.

These results show that style of deformation directly affects the evolution of fracture systems. The characteristics of these fracture systems display relationships between fracture intensity, fracture length, and bed curvature. Therefore, permeability in a fold system, even within same bed units, should be highly heterogeneous as different localities experience different deformation rates and stresses.

The results from this project could be applied to similar fold systems at other localities. Because of the inherent difficulty in sampling fracture systems in the subsurface, the relationships between fracture intensity, aperture and fracture length with shear strain and bed curvature could be used as a powerful tool to assess changes in permeability across different structural positions in unreachable areas. The ability to predict permeability across scales should be especially useful for the oil and gas industry when trying to maximize extraction from unconventional reservoirs.

REFERENCES

Bergbauer, S., 2007, Testing the predictive capability of curvature analyses, In Jolley, S., Barr, D., Walsh, J., and Knipe, R., Eds., Structurally complex reservoirs: Geological Society of London Special Publication 292, p.185 – 202.

Casey, M., and Butler, R., 2004, Modeling approaches to understanding fold development: implications for hydrocarbon reservoirs: Marine and Petroleum Geology, v. 21, p. 933 – 946.

Couples, G., and Lewis, H., 1998, Lateral variations in strain in experimental forced folds: Tectonophysics, v. 295, p.79 – 91.

Dickinson, W., 1981, Plate tectonic evolution of the southern Cordillera, In Dickinson, W., and Payne, W., Eds., Relations of tectonics to ore deposits of the southern Cordillera: Arizona Geological Society Digest, v. 14, p. 113 – 135.

Fossen, H., 2010, Structural Geology. University of Bergen. Cambridge University Press. Gale, J., Lander, R., Reed, R., and Laubach, S., 2010, Modeling fracture porosity evolution in dolostone: Journal of Structural Geology, v. 32, p. 1201 – 1211.

Gale, J., Lander, R., Reed, R., and Laubach, S., 2010, Modeling fracture porosity evolution in dolostone: Journal of Structural Geology, v. 32, p. 1201 – 1211.

Gibbons, J. D., and Chakraborti, S., 2003, Nonparametric Statistical Inference: CRC Press, New York, New York, 680 p.

Gillespie, P.A., Howard, C.B., Walsh, J.J., and Watterson, J., 1993, Measurement and characterization of spatial distributions of fractures: Tectonophysics, v. 226, p. 113-141.

Goldstein, J., 2003, Scanning electron microscopy and x-ray microanalysis: Kluwer Adacemic/Plenum Pulbishers, 689 p.

Graham, A., 2003, Statistics. Blacklick, Ohio: McGraw-Hill.

Gudmundsson, A., 2011, Rock fractures in geological processes: Cambridge: Cambridge University Press.

Deepa, P., Olson, J., and Thompson, L., 2000, Combining outcrop data and three-dimensional structural models to characterize fractured reservoirs: an example from Wyoming: American Association of Petroleum Geologists Bulletin, v. 84, p. 830 – 849.

Hoin, D., Surpless, B., and Mays, B., 2012, The role of mechanical stratigraphy in fault-propagation fold evolution: a case study: Southcentral Section GSA, Abstracts with Programs.

Hooker, J., Gale, J., Gomez, L, Laubach, S., Marrett, R., and Reed, R., 2009, Aperture-size scaling variations in a low-strain opening-mode fracture set, Cozzette Sandstone, Colorado: Journal of Structural Geology, v. 31, p. 707-718.

Keating, D. P., and M. P. Fischer, 2008, An experimental evaluation of the curvature-strain relation in fault-related folds: AAPG Bulletin, v. 92, p. 869–884.

Ladeira, F., and Price, N., 1981, Relationship between fracture spacing and bed thickness: Journal of Structural Geology, v. 3, p. 179 – 183.

Laubach, S., 1989, Paleostress directions from the preferred orientation of closed microfractures (fluid-inclusion planes) in sandstone, East Texas basin, U.S.A.: Journal of Structural Geology, v. 11, p. 603 – 611.

Laubach, S., 2003, Practical approaches to identifying sealed and open fractures: AAPG Bulletin v. 84, p. 561-79.

Laubach, S., Reed, R., Olson, R., Lander, R., and Bonnell, L., 2004, Coevolution of crack-seal texture and fracture porosity in sedimentary rocks: Cathodoluminescence observations of regional fractures: Journal of Structural Geology, v. 26, p. 967 – 982.

Laubach, S., Olson, J., and Gross, M., 2009, Mechanical and fracture stratigraphy: American Association of Petroleum Geologists Bulletin, v. 93, p. 1413 – 1426.

Lehman, T., and Busbey, A., 2007, Society of Vertebrate Paleontology Fall 2007 Big Bend field trip guide: Austin, Texas, Society of Vertebrate Paleontology, 117 p.

Lisle, R., 1994, Detection of zones of abnormal strains in structures using Gaussian curvature anaylsis: American Association of Petroleum Geologists Bulletin, v. 78, p. 1811 – 1819.

Liu, L., Gurnis, M., Seton, M., Saleeby, J., and Muller, R., 2010, The role of oceanic plateau subduction in the Laramide orogeny: Nature Geoscience Letters, doi: 10.1038/NGEO829.

Lonergan, L., 1999, Fractures, fluid flow and mineralization: Geological Society of London, Special Publication 155, p. 83-103.

Maler, M., 1990, Dead horse graben: a west Texas accommodation zone: Tectonics, v. 9, p. 1357 – 1368.

Marrett, R., 1996. Aggregate properties of fracture populations. Journal of Structural Geology 18, 169e631. 178.

Marrett, R., Aranda-García, M., 1999, Structure and kinematic development of the Sierra Madre Oriental fold-thrust belt, Mexico. *In*: Stratigraphy and Structure of the Jurassic and Cretaceous Platform and Basin Systems of the Sierra Madre Oriental, Monterrey and Saltillo Areas, Northeastern Mexico, a Field Book and Related Papers. South Texas Geological Society. Special Publication for the Annual Meeting of the American Association of

Petroleum Geologists and the SEPM. Society for Sedimentary Geology, San Antonio, p. 69-98.

Mauldon, M., Dunne, W., and Rohrbaugh, M., Jr., 2001, Circular scanlines and circular windows: new tools for characterizing the geometry of fracture traces: Journal of Structural Geology, v. 23, p. 247 – 258.

Mays, B., Surpless, B., and Hoin, D., 2012, Kinematic development of the Stillwell anticline, west Texas: Southcentral Section GSA, Abstracts with Programs.

Miller, D., Nilsen, T., and Bilodeau, W., 1992, Late Cretaceous to early Eocene geologic evolution of the U.S. Cordillera: In Burchfiel, B., Lipman, P., and Zoback, M. Eds., The Cordilleran Orogen: conterminous U.S.:Geological Society of America, v. G-3, p. 205 – 260. 15

Mercado L., 2012., The Relationship between Topographic Profile and Mechanical Stratigraphy in the Stillwell Anticline, West Texas. Trinity University Summer Symposium.

Moustafa, A.R., 1983, Analysis of Laramide and younger deformation of a segment of the Big Bend region, Texas: Ph.D. Thesis, University of Texas at Austin, Austin, Texas, 278 p.

Moustafa, A.R., 1988, Structural geology of the Sierra del Carmen, Trans-Pecos, Texas: Geological Quadrangle Map GQ-0054, University of Texas at Austin, Bureau of Economic Geology, 28 p.

Muehlberger, W.R., 1980, Texas Lineament Revisited: New Mexico Geological Society Guidebook, 31st Field Conference, Trans-Pecos Region, p. 113 – 121.

Muehlberger, W.R., and Dickerson, P.W., 1989, A tectonic history of Trans-Pecos, Texas, In Muehlberger, W.R., andDickerson, P.W., Eds., Structure and stratigraphy of Trans-Pecos Texas: American Geophysical Union Field Trip Guidebook T315, p. 35 – 54.

Murray, G., 1968, Quantitative fracture study – Sanish Pool, McKenzie County, North Dakota: American Association of Petroleum Geologists Bulletin, v. 52, p. 57 – 65.

Narr, W., 1996, Estimating average fracture spacing in subsurface rock: American Association of Petroleum Geologists Bulletin, v. 80, p. 1565 – 1586.

Nelson, R.A., and Serra, S., 1995, Vertical and lateral variations in fracture spacing in folded carbonate sections and its relation to locating horizontal wells: Journal of Canadian Petroleum Technology, v. 34, p. 51-56.

Nelson, R., 2001, Geologic analysis of naturally fractured reservoirs, 2nd Ed.: Gulf Professional Publishing, Boston, Massachusetts, 332 p.

Ortega, O., Marrett, R., and Laubach, S., 2006, A scale-independent approach to fracture intensity and average spacing measurement: American Association of Petroleum Geologists Bulletin, v. 90, p. 193 – 208.

Ortega, O., Gale, J., and Marrett, R., 2010, Quantifying diagenetic and stratigraphic controls on fracture intensity in Platform carbonates: an example from the Sierra Madre Oriental, northeast Mexico: Journal of Structural Geology, v. 32, p. 1943 – 1959.

Page, W., Turner, K., and Bohannon, R., 2008, Geological, Geochemical, and Geophysical Studies by the U.S. Geological Survey in Big Bend National Park, Texas, In Gray, J., and Page, W., Eds., U.S. Geological Survey Circular 1327, 93 p.

Palmström, A.,1995, RMi - a system for characterization of rock masses for rock engineering purposes: Ph.D. thesis, University of Oslo, Norway, 408 pp.

Palmström, A., and Stromme, B., 1996, The Weighted Joint Density Method Leads to Improved Characterization of Jointing: Conference on Recent Advances in Tunnelling Technology, New Delhi, India, 6p.

Paterson, M., and Wong T., 2005, Experimental Rock Deformation - The Brittle Field. Springer-Verlag Berlin Heidelber.

Price, N., 1959, Mechanics of jointing in rocks: Geological Magazine, v. 96, p. 149 – 167.

Smart, K., Ferrill, D., and Morris, A., 2009, Impact of interlayer slip on fracture prediction from geomechanical models of fault-related folds: American Association of Petroleum Geologists Bulletin, v. 93, p. 1447 – 1458.

St. John, B.E., 1965, Structural geology of Black Gap area, Brewster County, Texas: Ph.D. Thesis, University of Texas at Austin, Austin, Texas, 200 p.

St. John, 1966, Geology of Black Gap area, Brewster County, Texas: Geologic Quadrangle Map GQ-30, University of Texas at Austin, Bureau of Economic Geology, 18 p.

Stearns, D. W., 1968, Certain aspects of fracture in naturally deformed rocks, In R. E. Riecker, Ed., NSF advanced science seminar in rock mechanics: Bedford, Massachusetts, Air Force Cambridge Research Laboratories Special Report, p. 97–118.

Stearns, D., and Friedman, M., 1972, Reservoirs in fractured rocks: American Association of Petroleum Geologists Memoir, No. 16, p. 82 – 100.

Stewart, S., and Podolski, R., 1998, Curvature analysis of gridded geological surfaces, In Coward, M., Daltaban, T., and Johnson, H., Eds., Structural geology in reservoir characterization: Geological Society of London Special Publication 127, p. 133 – 147.

Stone, D. S., 1993, Basement-involved thrust-generated folds as seismically imaged in the subsurface of the central Rocky Mountain foreland: *In* C. J. Schmidt, R. B. Chase, and E. A. Erslev, Eds., Laramide basement deformation in the Rocky Mountain foreland of the western United States: Geological Society of America Special Paper 280, p. 271–318.

Surpless, B.E., and Quiroz, K., 2010, Determining subsurface fault geometry from complex 3D fold patterns: formation of the Stillwell anticline, west Texas: American Geophysical Union, Abstracts with Programs, Abstract T51A-2022.

Surpless, B., Mays, B., and Hoin, D., 2012, Kinematic evolution of the Stillwell anticline system, west Texas: implications for fluid flow within subsurface systems: Geological Society of America, Abstracts with Programs, Abstract 206006.

Surpless, B., 2013, A new method to correct outcrop-scale observational bias: unpublished manuscript.

Terzaghi R., 1965, Sources of error in joint surveys. Geotechnique, v. 15, 1965, pp 287-304.

Tinker, N., Keesling, G., Mercado, L., Surpless, B., and DeZoeten, E., 2013, Topographic profile, mechanical stratigraphy, and interlayer slip: exploring coupled fold-fracture evolution of the Stillwell anticline, west Texas: Abstracts with Programs, Southcentral Geological Society of America, Abstract 217336.

Tran, N., 2007, Fracture orientation characterization: Minimizing statistical modeling errors: Computational Statistics and Data Analysis, v. 51, p. 3187-3196.

Twiss, R., and Moores, E., 1992. Structural Geology. University of California at Davis. W.H. Freeman and Company New York.

Underwood, C.A., Cooke, M.L., Simo, J.A., and Muldoon, M.A., 2003, Stratigraphic controls on vertical fracture patterns in Silurian dolomite, northeastern Wisconsin: American Association of Petroleum Geologists Bulletin, v. 87, p. 121–142.

APPENDIX A. FRACTURE DATA

LOCATION 1

Fracture ID	Fracture Position		Dip Azimuth	Dip	Aperture	Morphology*	Length	Fill**
	Hor.	Vert.						
1	1.8	1.76	33	59	0.215	3	4.5	3
2	3.3	1.2	337	43	0.265	1	2.6	2
3	2.3	2.2	349	34	0.095	2	4.0	1
4	2	3.52	326	51	0.115	3	5.0	1
5	0	6.62	298	33	0.095	2	3.2	2
6	1.5	7.8	88	84	0.095	2	1.8	1
7	2.1	6.9	46	49	0.115	3	5.5	1
8	2.1	8	157	84	0.075	2	2.0	1
9	2.2	8.9	81	79	0.115	2	4.6	2
10	1.4	9.6	24	75	0.095	2	5.2	1
11	1.7	8.96	13	56	0.05	1	2.5	1
12	2.5	9.79	79	84	0.062	2	4.4	1
13	1.2	11	338	59	0.095	2	3.2	1
14	3.6	11	351	66	0.05	2	4.3	1
15	3.1	2.8	330	45	0.075	3	5.5	1
16	3.4	4.4	329	59	0.075	1	1.6	1
17	4.2	5.02	32	87	0.062	2	5.2	1
18	3.5	6.39	11	85	0.14	3	3.9	1
19	4.5	5.72	32	83	0.05	1	1.3	1
20	3.5	7.2	346	68	0.05	2	3.5	1
21	3.3	8.8	37	81	0.075	3	1.8	1
22	3.8	8.55	347	67	0.062	1	2.5	1
23	4.3	8.6	52	68	0.115	2	0.5	2
24	3.4	10.3	9	63	0.095	2	3.6	1
25	3.7	10.3	351	59	0.05	2	1.2	1
26	4.7	11.9	1	53	0.062	2	0.8	1
27	4.9	1.3	326	44	0.05	2	2.0	1
28	6.4	0.8	325	49	0.05	1	3.3	1
29	5	2.55	13	72	0.05	1	1.4	1
30	5.8	1.6	334	61	0.05	1	1.0	1
31	6.2	1.3	267	72	0.115	2	1.7	2
32	5.5	2.35	178	86	0.075	3	4.8	2
33	4.5	2.6	238	84	0.115	2	1.1	2
34	4.1	3	250	64	0.75	1	2.0	2
35	4.4	3.4	250	64	0.205	1	1.0	1
36	4.1	3.6	5	61	0.175	1	2.0	1
37	4.3	3.65	3	68	0.05	2	3.0	1
38	5	3.8	19	80	0.095	2	2.2	1
39	5.6	4.4	346	46	0.062	1	4.3	1
40	5.7	4	345	51	0.05	2	3.8	1
41	5.7	4.2	8	84	0.05	2	2.8	1
42	7.1	4	358	77	0.05	2	0.8	1
43	6.6	4.9	0	63	0.14	3	2.5	1
44	6.9	5.1	345	69	0.05	2	2.0	1
45	7.3	4.8	283	78	0.05	2	2.8	1
46	7.7	5	284	70	0.05	1	1.4	1
47	7.4	6.3	32	58	0.115	2	2.6	2
48	5.2	6.2	93	49	0.115	3	3.0	2
49	5.4	7.1	2	41	0.115	2	5.6	2
50	6.4	7.4	287	40	0.75	2	1.0	2
51	5.8	8.3	291	50	0.062	2	3.0	1
52	5	7.9	18	87	0.062	2	2.0	1
53	5.3	8.5	217	89	0.062	2	7.4	2
54	6.3	8.8	81	87	0.062	2	1.8	1
55	5.2	9.6	10	63	0.115	3	2.2	1
56	6.6	8.3	73	86	0.095	1	1.3	1
57	6	8.4	35	8	0.062	1	8.0	1
58	6.3	9.3	332	62	0.062	2	0.5	1

Fracture ID	Fracture Position		Dip Azimuth	Dip	Aperture	Morphology*	Length	Fill**
	Hor.	Vert.						
58	6.3	9.3	332	62	0.062	2	0.5	1
59	6.1	9.5	57	68	0.115	2	3.4	2
60	5.2	9.6	171	84	0.095	1	4.0	1
61	5.8	10.5	222	86	0.075	1	3.8	1
62	5.2	10.1	228	85	0.14	1	7.2	1
63	6.2	11	246	86	0.14	1	5.4	1
64	5.2	11.7	351	62	0.062	1	3.9	2
65	6.4	11.8	351	76	0.062	2	3.4	1
66	6.9	10.9	348	66	0.05	1	3.2	1
67	6.8	2	258	64	0.095	2	4.0	2
68	6.9	1.6	171	89	0.115	3	8.2	2
69	8.3	2.1	352	70	0.062	3	5.0	1
70	7.4	2.8	0	69	0.062	2	7.1	1
71	7.2	3.1	42	52	0.075	3	11.0	2
72	7.5	3.8	357	43	0.05	2	1.2	1
73	8.8	4	343	53	0.05	2	3.2	1
74	8.6	5.1	359	77	0.115	2	3.9	1
75	9.4	4.8	22	66	0.062	2	1.6	1
76	9.2	5.5	357	82	0.05	2	2.6	1
77	7.5	6.95	330	57	0.095	2	3.1	1
78	9.2	7.1	312	88	0.115	2	4.5	2
79	9	7	357	63	0.14	2	2.0	2
80	8.9	7.3	315	89	0.062	1	3.1	3
81	8.4	7.3	336	76	0.14	2	3.2	1
82	7.4	8.3	212	83	0.062	3	1.2	1
83	7.9	8.5	28	61	0.062	2	0.8	1
84	9.1	7.8	342	80	0.075	2	3.2	2
85	8.8	8	235	75	0.075	2	1.2	1
86	9.4	9.5	53	58	0.075	2	0.8	1
87	7.7	10.3	208	87	0.062	2	1.0	1
88	7.6	10.5	249	83	0.095	2	2.1	1
89	8	11	37	67	0.075	2	2.3	1
90	8.6	1.8	293	78	0.175	3	4.6	1
91	9.1	2.5	323	62	0.115	1	0.7	1
92	10.1	3.8	350	60	0.075	2	2.0	1
93	10.7	4.1	34	88	0.075	2	1.8	2
94	10.2	4.6	1	88	0.05	3	3.0	1
95	10.8	4.5	333	52	0.05	2	2.5	1
96	10.1	5.3	172	83	0.062	2	1.9	1
97	10.9	5.5	349	59	0.062	3	2.0	1
98	10.1	5.9	173	90	0.05	2	2.6	1
99	11.2	5.9	339	87	0.075	2	0.6	1
100	10.2	6.9	128	88	0.075	2	0.8	1
101	9.6	7.9	8	88	0.115	2	1.9	2
102	10.5	7.8	328	90	0.05	2	1.7	1
103	10.2	8.4	352	78	0.062	2	2.2	1
104	10.5	8.2	351	86	0.062	2	0.8	1
105	9.8	9	1	48	0.062	2	2.5	2
106	11.5	8.9	7	81	0.062	2	2.2	2
107	11.5	9.3	28	57	0.095	2	2.9	1
108	11.1	10	63	53	0.115	2	5.2	2
109	9.6	10.8	348	68	0.095	2	1.8	1
110	10.4	10.9	239	76	0.095	2	4.5	1
111	10.4	1.1	128	35	0.062	2	2.3	1
112	10.4	1.5	96	39	0.14	2	3.0	2
113	11.4	1.5	175	46	0.075	1	1.0	1
114	10.6	2.1	77	52	0.095	2	9.0	1
115	10.5	2.8	81	49	0.095	2	2.3	1

LOCATION 1 (CONTINUED)

Fracture ID	Fracture Position Hor.	Fracture Position Vert.	Dip Azimuth	Dip	Aperture	Morphology*	Length	Fill**
116	11.3	2.8	328	68	0.075	2	2.0	1
117	11.7	3.7	334	63	0.05	2	1.0	1
118	11.4	4.2	351	43	0.05	3	1.0	1
119	11.5	4	46	84	0.062	2	1.8	1
120	12	5.4	64	57	0.062	2	2.3	1
121	10.5	6.3	52	87	0.05	2	2.2	1
122	11	6.5	349	79	0.05	2	2.4	1
123	11.5	6.6	337	90	0.115	3	3.1	1
124	12.2	6.5	343	49	0.115	2	1.2	1
125	12.5	6.6	335	66	0.075	2	2.9	1
126	11.7	7.4	357	75	0.062	2	3.1	1
127	13	7.9	348	46	0.095	2	2.0	2
128	12	8	349	69	0.075	2	3.2	1
129	12.3	8.2	28	47	0.05	2	2.8	2
130	12.9	9.4	34	55	0.062	1	4.5	2
131	12.7	11.1	350	58	0.062	1	2.9	1
132	13.4	10.9	353	44	0.05	2	2.2	1
133	12.5	1.3	328	65	0.075	2	1.2	1
134	13	2.2	37	75	0.075	2	0.9	1
135	12.1	2.8	310	74	0.075	2	1.0	1
136	12.6	3.3	22	87	0.05	2	3.0	1
137	13.6	2.6	36	77	0.075	2	2.5	1
138	14.3	1.9	182	85	0.095	3	2.9	1
139	14.2	1.9	351	46	0.05	2	1.8	1
140	14.3	0.9	337	63	0.05	2	2.8	1
141	14.4	3.3	358	61	0.062	2	3.0	1
142	14.5	3.9	354	67	0.062	3	1.3	1
143	14.5	4.2	355	86	0.075	3	1.0	1
144	15	3.9	358	52	0.095	2	2.0	1
145	12.8	3.6	202	86	0.062	1	1.2	1
146	12.6	4.5	14	52	0.095	2	3.8	1
147	13.6	5.1	26	78	0.05	2	2.5	1
148	14.1	5.1	345	82	0.062	2	1.1	1
149	13.8	5.9	31	78	0.095	2	3.2	1
150	14.4	5.5	345	68	0.062	2	2.3	1
151	14.2	5.8	346	56	0.05	1	1.5	1
152	12.1	5.9	257	75	0.115	1	4.0	1
153	13.8	6.8	33	61	0.075	2	2.3	1
154	13.8	7.2	272	75	0.075	1	5.0	1
155	13	8.2	276	78	0.115	2	2.0	1
156	13.5	7.9	268	78	0.062	2	2.4	1
157	14.2	7.8	33	60	0.062	2	1.0	1
158	14.2	8.3	18	60	0.075	2	6.5	2
159	14.5	8.9	32	74	0.075	2	2.8	1
160	15	8.4	339	26	0.062	3	2.5	1
161	14.6	9.2	12	51	0.062	3	5.0	1
162	13.6	9.7	46	60	0.115	3	2.5	2
163	15	10.5	75	84	0.062	2	2.2	1
164	16	1.6	95	86	0.14	2	1.2	1
165	16.1	2.6	51	62	0.062	2	4.0	1
166	16.7	3.2	28	57	0.075	2	4.5	1
167	18.1	2.8	28	51	0.05	2	1.8	1
168	17.4	6.7	351	64	0.115	2	1.0	1
169	18.2	4.3	2	37	0.075	3	6.0	2
170	15.9	5.6	351	43	0.062	1	2.1	1
171	16.2	4.9	51	58	0.062	2	3.1	1
172	15.4	6.6	331	77	0.0115	3	11.0	2
173	16.2	6.4	336	84	0.095	2	1.5	1
174	17.5	6	238	64	0.095	1	3.0	1
175	18	6.3	257	80	0.05	1	2.0	1
176	17.7	7	95	56	0.075	3	2.0	3
177	17.5	7.4	33	66	0.05	3	3.3	1

Fracture ID	Fracture Position Hor.	Fracture Position Vert.	Dip Azimuth	Dip	Aperture	Morphology*	Length	Fill**
178	15.8	8.3	270	84	0.115	2	2.0	1
179	16	8.4	320	88	0.05	2	2.0	1
180	16	9.5	331	56	0.062	2	1.2	2
181	16.2	10	25	72	0.05	2	2.0	1
182	17	11.3	227	69	0.05	2	1.0	1
183	17.3	11.4	227	69	0.05	1	1.5	1
184	16.9	1.7	84	64	0.05	2	2.0	1
185	17.5	0.7	118	83	0.062	1	6.0	1
186	17.2	1.4	134	80	0.095	3	1.0	1
187	18.5	1	51	41	0.05	3	3.0	2
188	18.4	1.8	3	48	0.095	2	1.1	1
189	17.7	2.9	266	61	0.115	2	3.0	1
190	18.8	2.5	69	62	0.095	2	3.0	1
191	18.9	3.2	26	56	0.062	2	2.4	1
192	20.1	4.7	27	54	0.05	2	2.5	1
193	19.4	6.5	356	57	0.05	2	2.3	1
194	20.1	7	217	84	0.075	2	1.3	1
195	19.7	7.6	38	56	0.075	2	3.5	2
196	17.7	8.4	46	89	0.062	2	1.2	1
197	17.8	9.7	11	52	0.095	2	2.0	2
198	19.5	8.6	309	88	0.115	2	2.5	1
199	19.8	8.3	36	70	0.14	2	2.0	1
200	18.1	10	0	47	0.075	2	2.2	1
201	19	9.8	48	62	0.062	3	1.0	3
202	18.3	11.4	352	51	0.05	3	3.3	1
203	19	10.6	27	53	0.075	2	7.0	2
204	19.2	10.3	28	64	0.062	2	1.2	1

**Fill		*Morphology	
Filled fracture	1	Planar	1
Partially filled fract.	2	Sub-planar	2
Open fracture	3	Sinuous	3

LOCATION 2

Fracture ID	Fracture Position		Dip Azimuth	Dip	Aperture	Morphology*	Length	Fill**
	Hor.	Vert.						
1	1	2.3	78	76	0.62	1	6.0	1
2	1.1	5.5	352	89	0.095	1	11.0	1
3	1.5	4.7	352	89	0.4	1	7.0	1
4	2	4.3	0	65	0.4	2	13.5	1
5	2.8	3	168	67	0.215	1	3.8	1
6	3.5	5.2	219	62	0.5	1	3.0	1
7	5	1	275	80	0.215	1	9.0	1
8	4	8	125	90	0.4	2	7.0	1
9	7.5	1.6	110	82	0.05	1	9.0	1
10	8	3.3	216	84	0.115	2	8.0	1
11	8.5	2.4	235	83	0.173	1	8.7	1
12	7.5	7.5	109	89	0.05	1	8.8	1
13	10	4	76	57	0.095	2	7.0	3
14	9	7.3	253	89	0.4	1	7.5	1
15	10.5	9.9	84	87	0.05	2	10.0	1
16	11	8.8	38	36	0.175	2	13.0	1
17	12	1.2	160	72	0.062	1	2.0	1
18	13	1	167	82	0.5	2	5.5	1
19	13.5	1.7	201	85	0.4	2	10.0	1
20	13.5	6.1	115	70	0.33	1	7.5	1
21	14.5	2.4	203	81	0.4	2	6.0	1
22	8	11.8	124	88	0.265	2	10.5	1
23	9.5	11.7	154	62	0.05	1	10.0	1
24	15	8.4	182	65	0.215	2	4.8	1
25	15.5	0.4	182	65	0.215	2	4.8	1
26	15.5	0.8	162	81	0.33	1	3.0	1
27	17	1.2	17	81	0.265	3	3.0	1
28	17	0.2	127	85	0.4	3	4.5	1
29	24	0.5	119	72	0.4	3	4.0	1
30	19	0.8	167	81	0.5	2	2.5	1
31	20.2	1.2	18	84	0.175	2	1.0	1
32	20	1.8	108	72	0.215	2	3.0	1
33	21	1.2	64	78	0.062	2	3.0	1
34	20.5	4.3	148	81	0.05	1	8.0	2
35	23	3	265	87	0.14	2	4.0	1
36	23.5	4.2	232	82	0.4	2	9.5	1
37	24	5.1	134	83	0.075	1	4.0	1
38	25	3.3	216	67	0.4	3	6.0	1
39	23.8	5.7	142	74	0.05	1	6.5	1
40	27	3.1	185	52	0.14	2	3.0	1
41	26	2.3	297	83	0.115	2	3.5	1
42	28	2.4	237	71	0.265	3	6.0	1
43	25	5.6	249	69	0.5	3	14.0	1
44	20.5	6.1	163	67		3	4.0	1
45	22	6.6	118	68	0.5	2	6.0	1
46	20.5	8.4	51	64	0.33	2	5.5	1
47	13.5	9.2	71	67	0.33	3	5.5	1
48	15.5	8.5	299	77	0.062	3	3.0	1
49	14.5	9	94	79	0.062	1	3.0	1
50	16	8.7	122	68	0.095	1	5.0	1
51	16.5	8.3	133	69	0.4	1	3.0	1
52	17	8.3	285	85	0.095	1	3.0	1
53	18	9.4	48	55	0.5	2	4.0	1
54	15	10.6	57	74	0.215	2	5.0	1
55	14.5	10.6	79	84	0.05	2	3.0	1
56	19.5	10.9	61	63	0.62	3	15.0	1
57	29	2.8	119	71	0.071	1	3.0	1
58	29.5	2.8	217	85	0.071	1	4.0	1
59	30.5	2.7	112	67	0.05	1	5.0	1
60	30.5	3	234	82	0.05	1	7.0	1
61	32	2.7	275	72	0.115	2	5.5	1
62	31	3.1	225	76	0.062	1	1.0	1
63	30.5	2.9	289	86	0.265	2	9.0	1
64	27	6.7	267	87	0.215	1	4.0	1
65	28.5	6.8	59	67	0.075	1	12.0	1
66	28.5	7.7	80	67	0.062	1	4.0	1
67	30	7.9	30	57	0.075	1	5.0	1
68	30.5	7.6	30	71	0.05	1	3.0	1
69	33	7.2	187	86	0.215	3	5.0	1
70	32	6.5	317	58	0.05	1	4.0	1
71	31	5.3	11	68	0.115	2	6.0	1
72	32	4.7	12	70	0.062	2	2.0	1
73	31.5	2	29	6	0.115	3	4.0	1
74	34.5	1.5	30	72	0.265	3	11.0	1
75	36	2.9	91	59	0.14	1	4.0	1
76	37	3.1	102	69	0.095	1	4.0	1
77	35	3.4	107	89	0.115	1	4.0	1
78	36.5	1	112	89	0.062	1	3.0	1
79	35.5	6.8	53	82	0.065	2	6.6	1
80	37	1.8	303	87	0.33	3	6.0	1
81	42	1	34	69	0.215	2	8.0	1
82	45	1	68	60	0.215	2	5.0	1
83	38	6.8	284	81	0.05	2	6.0	1
84	37	7	288	83	0.095	2	5.5	1
85	36	7.7	113	76	0.05	1	4.0	1
86	35	8.3	284	84	0.062	1	8.0	1
87	34.5	8.6	281	83	0.095	1	7.0	1
88	40.5	5.3	178	84	0.115	2	6.0	1
89	41	6.8	86	52	0.115	1	9.0	1
90	39.5	7	102	86	0.175	2	7.0	1
91	42.5	6.5	271	85	0.14	1	10.0	1
92	43	4.9	71	50	0.05	2	4.5	1
93	41.5	4.3	99	90	0.115	1	6.0	1
94	42	4	102	61	0.062	1	4.5	1
95	43	3.2	240	73	0.115	1	5.0	1
96	43.5	3.6	106	77	0.062	2	8.0	1
97	44	3.8	36	67	0.115	1	3.3	1
98	43.5	2.4	16	82	0.062	1	4.0	1
99	45	3.3	18	61	0.095	1	2.2	1
100	46	3.2	127	74	0.095	2	3.3	1
101	44	5.3	110	60	0.05	1	5.0	1
102	44.5	6.4	112	74	0.05	1	3.0	1
103	45	6.3	114	71	0.05	1	5.0	1
104	44	7.4	241	78	0.265	3	11.0	1
105	44	7.2	117	87	0.062	2	6.6	1
106	46.5	5.9	242	79	0.215	2	3.0	1
107	43	8.4	128	52	0.05	2	5.5	1
108	46	7.5	46	16	0.095	2	4.0	2
109	46	7.6	68	55	0.062	2	4.5	1
110	48	4.1	82	37	0.095	1	1.1	3
111	50.5	7.6	117	65	0.269	2	6.6	1
112	49.5	6.6	110	54	0.095	1	2.2	1
113	50	4.9	121	83	0.115	1	5.0	1
114	47	2.6	104	57	0.115	2	4.0	3
115	50	5.3	3	66	0.062	1	2.0	1
116	48.5	1.2	221	56	0.05	2	3.5	1
117	45.5	3.9	115	59	0.062	1	1.5	1
118	49	2.9	9	31	0.175	2	7.0	2
119	52	1.5	130	72	0.062	1	3.0	1
120	52	2.8	105	47	0.095	1	3.3	1
121	51	3.3	318	81	0.075	1	6.0	1
122	51.5	3.8	136	75	0.075	1	6.0	1
123	51.5	5.3	359	79	0.05	2	3.0	1
124	52	6	359	79	0.062	1	5.0	1

LOCATION 2 (continued)

Fracture ID	Fracture Position		Dip Azimuth	Dip	Aperture	Morphology*	Length	Fill**
	Hor.	Vert.						
125	54	4.2	11	63	0.062	1	4.0	1
126	53.5	5.5	209	82	0.05	1	5.0	1
127	55	5.9	124	40	0.062	2	4.0	1
128	53	8.5	199	86	0.05	1	3.3	1
129	57	7.1	42	75	0.075	1	2.0	1
130	57	7.8	89	76	0.14	2	3.3	1
131	56.5	5.1	123	58	0.4	2	10.5	1
132	55	1.3	121	56	0.14	2	4.5	1
133	58	4	125	45	0.33	3	4.0	1
134	58.5	7.1	259	74	0.4	2	3.0	1
135	60	4.8	196	84	0.115	1	2.2	1
136	61	4	124	54	0.33	2	9.5	1
137	59	8.1	190	48	0.05	1	2.0	1
138	60.5	6.9	253	74	0.062	3	3.0	1
139	61	8.4	121	59	0.062	2	3.0	1
140	61.5	9.2	127	50	0.05	1	2.0	1
141	62.5	8.2	118	50	0.115	2	4.0	1
142	62.5	7.2	237	81	0.175	1	5.0	1
143	62	6	119	51	0.4	2	5.0	1
144	63	4.5	121	57	0.062	1	4.0	1
145	64.5	5	119	57	0.062	1	5.0	1
146	63	6	119	49	0.05	2	5.0	1
147	63	3	116	66	0.05	1	2.0	1
148	64.5	1.8	115	64	0.14	2	4.5	1
149	64	2.7	121	50	0.05	1	4.0	1
150	65	1.5	164	80	0.115	1	3.3	1
151	65	1.2	91	41	0.062	2	3.0	1
152	66.5	2.2	112	41	0.062	2	3.0	1
153	66.5	5.5	113	44	0.095	1	1.0	1
154	67.5	7	122	44	0.062	1	1.0	1
155	67	5.5	118	52	0.05	2	2.0	1
156	68.5	3.4	112	53	0.095	2	4.0	1
157	68.5	3	100	49	0.062	1	6.0	1
158	69	3.4	92	60	0.062	1	5.0	1
159	69	2.5	112	44	0.062	1	4.0	1
160	70.5	3.8	112	62	0.075	2	2.0	1
161	68	4.4	289	78	0.4	3	7.0	1
162	70	5.1	177	59	0.062	2	3.0	1
163	69.5	6.1	126	45	0.5	2	7.5	2
164	66.5	5.4	108	42	0.062	2	7.5	1
165	68.5	6	134	36	0.05	1	10.0	1
166	67.5	5.3	198	90	0.05	1	3.0	1
167	66.5	6.5	48	72	0.14	2	1.0	1
168	65	7	114	36	0.215	2	7.0	1
169	66	7.3	117	39	0.14	2	3.0	1
170	64	7.1	195	32	0.175	2	6.0	2
171	69	6.8	38	61	0.095	1	1.0	2
172	69.5	6.6	27	59	0.095	1	0.5	1
173	70	6.4	116	58	0.14	3	3.0	1
174	71	2.8	123	62	0.062	1	3.0	1
175	70.5	2.9	179	68	0.14	2	5.5	1
176	70.5	2.1	113	53	0.05	2	2.5	1
177	72.5	2	124	57	0.05	1	3.0	1
178	72	1.6	121	73	0.062	1	6.0	1
179	72.5	1.8	223	88	0.05	1	2.5	1
180	73	1.5	154	59	0.05	1	5.0	1
181	70.5	1.3	200	61	0.062	1	2.5	1
182	73	0.7	138	79	0.075	1	3.4	1
183	76.5	1	47	88	0.05	1	3.3	1
184	75	1.5	46	39	0.05	1	3.5	1
185	75.5	1.5	131	52	0.062	2	4.0	1
186	75.5	1.1	127	56	0.33	1	6.0	1
187	76.5	1.9	132	53	0.075	1	3.5	1
188	77.5	0.8	143	55	0.05	1	4.0	1
189	78	1.3	138	59	0.062	1	4.0	1
190	78.5	1.5	142	59	0.05	1	4.0	1
191	79	1.8	109	67	0.075	2	2.0	1
192	76	2.6	116	54	0.175	2	7.0	1
193	75.5	2.9	34	87	0.33	2	8.0	1
194	75	2.8	115	53	0.095	2	4.5	1
195	74.5	2.5	135	57	0.062	1	5.5	1
196	75.5	4.4	148	63	0.075	2	6.0	1
197	76	4.6	139	51	0.05	1	1.0	1
198	72.5	5	89	72	0.05	1	3.3	1
199	71.5		183	58	0.075	1	2.5	1
200	73	5.9	119	52	0.062	1	5.0	1
201	72	5.3	97	76	0.075	2	5.5	1
202	70.5		189	64	0.14	1	4.5	1
203	72.5	7.2	84	66	0.095	1	2.4	2
204	72.5	8.7	84	60	0.075	2	2.5	1
205	70.5	8.8	86	62	0.05	2	4.0	1
206	72	9.1	151	64	0.05	1	4.0	1
207	73	8.5	240	75	0.5	3	13.0	2
208	74.5	8	348	80	0.095	2	1.3	2
209	75.5	6.2	348	80	0.075	1	2.3	1
210	74.5	6.2	111	54	0.14	1	6.0	1
211	77	6.5	292	76	0.14	2	4.0	1
212	78	6.2	293	76	0.265	3	14.0	1

**Fill

Filled fracture	1
Partially filled fract.	2
Open fracture	3

*Morphology

Planar	1
Sub-planar	2
Sinuous	3

LOCATION 3

Fracture ID	Fracture Position		Dip Azimuth	Dip	Aperture	Morphology*	Length	Fill**
	Hor.	Vert.						
1	0	0.9	339	68	0.330	2	7.5	2
2	2	4.4	7	71	0.175	2	8.0	2
3	6.6	1.6	119	49	0.075	1	2.0	1
4	6.9	1.3	215	41	0.175	2	3.3	1
5	7.5	4.5	347	82	0.62	2	6.0	1
6	8.4	5.6	140	55	0.062	1	2.5	1
7	9.3	2	171	61	0.115	2	5.0	1
8	12	0	139	19	0.095	2	4.5	2
9	11.8	0.9	149	31	0.115	1	8.0	1
10	13	1.6	73	53	0.062	2	6.0	1
11	12.4	7.2	154	31	0.75	3	10.0	1
12	14.6	5.8	208	36	0.075	1	7.5	1
13	15.5	4.1	175	46	0.075	1	4.5	1
14	17.2	0.6	143	35	0.075	1	2.0	1
15	17.8	4.1	67	83	0.140	2	8.5	2
16	19.7	7.2	45	82	0.400	2	6.0	2
17	20.3	7.2	229	89	0.050	2	7.0	1
19	20	3.4	146	76	0.05	1	4.0	1
20	20.9	5.8	227	87	0.075	2	4.0	1
21	20.7	4.7	229	87	0.050	3	9.0	1
22	21.5	6.8	56	85	0.115	2	8.5	1
23	22.4	1.5	237	87	0.215	3	7.0	1
24	23	2.3	84	43	0.095	2	4.0	1
25	23.6	5	151	59	0.14	1	1.5	1
26	24.5	2.6	81	61	0.075	2	5.5	1
27	23.9	2.5	230	73	0.140	1	4.5	1
28	23	4.4	174	59	0.14	2	6.0	1
29	25.4	2	77	54	0.075	1	5.0	1
30	25.6	2.3	77	54	0.050	1	6.0	1
31	25.8	5.7	168	32	0.05	2	5.5	1
32	21.6	3.2	80	67	0.075	1	5.0	1
33	28.3	3.6	80	67	0.075	1	6.0	1
34	28.4	5.2	67	80	0.050	1	6.6	1
35	28.8	5	249	33	0.115	1	4.0	1
36	30.5	5.5	249	27	0.140	1	6.0	1
37	31.2	2.8	118	27	0.095	1	4.0	1
38	32.2	5.3	177	55	0.115	1	7.0	1
39	33.6	1.4	68	71	0.050	1	6.5	1
40	35	2.2	249	90	0.075	1	6.0	1
41	35.6	1.1	76	87	0.095	1	6.3	1
42	33.2	5	162	69	0.14	1	5.0	1
43	34	5	154	69	0.05	1	4.0	1
44	34.2	3.3	149	69	0.175	1	4.0	1
45	35.6	4.1	217	69	0.115	1	4.0	1
46	36.2	5.4	3	89	0.115	3	5.0	1
47	35.7	3.6	138	59	0.05	1	5.0	1
48	35.3	5.9	137	73	0.095	1	2.5	1
49	37.8	7.1	196	60	0.115	1	4.5	2
50	38.3	6.6	152	67	0.062	2	4.0	1
51	38.7	5.5	236	66	0.095	1	6.0	1
52	37.5	6	158	67	0.115	1	1.0	1
53	39.3	1.9	142	31	0.050	1	6.0	1
54	38.9	3.6	133	62	0.050	1	1.3	1
55	40.3	4.8	194	74	0.115	1	9.0	1
56	40.2	5.4	216	78	0.075	1	7.0	1
57	41.7	6	146	49	0.075	1	4.0	1
58	41.2	6.9	152	51	0.05	2	3.0	1
59	41.7	3.4	137	44	0.075	1	5.0	1
60	41.9	2.8	126	49	0.075	1	5.0	1
61	43.1	4.7	179	62	0.05	2	6.0	1
62	43.6	5.3	185	55	0.05	2	5.0	1
63	44.7	3.2	214	83	0.05	1	3.0	1

Fracture ID	Fracture Position		Dip Azimuth	Dip	Aperture	Morphology*	Length	Fill**
	Hor.	Vert.						
64	44.4	2.8	177	72	0.05	1	5.0	1
65	45	3.8	181	61	0.062	1	4.0	1
66	45.6	6.9	132	56	0.075	2	7.0	1
67	45.1	5.3	207	56	0.05	1	5.0	1
68	45.9	5.3	209	59	0.062	1	3.0	1
69	46.3	5.9	128	48	0.075	1	3.0	1
70	47.7	6.3	171	70	0.05	2	3.0	1
71	48.8	5.2	166	65	0.075	1	5.0	1
72	49.6	4.6	106	28	0.050	2	4.0	1
73	51.6	4.5	141	45	0.05	2	4.0	1
74	51.5	3.6	187	71	0.05	1	5.0	1
75	52.5	3.9	249	40	0.140	2	4.0	1
76	53.3	4.5	141	45	0.175	2	3.5	1
77	53	4.2	181	74	0.062	1	6.0	1
78	53.2	1.9	172	60	0.05	1	4.0	1
79	53.4	3.2	77	88	0.05	1	4.0	1
80	53.9	1.9	149	80	0.062	2	5.0	1
81	55.9	2.9	77	54	0.175	1	4.5	1
82	55.2	4.8	213	53	0.115	1	5.0	1
83	54.7	4.6	126	40	0.14	1	2.0	1
84	56.7	6.1	208	83	0.115	2	4.0	1
85	56.2	6	178	62	0.075	2	3.0	1
86	57.5	3.9	154	69	0.075	1	5.0	1
87	57	5.3	173	52	0.05	2	3.0	1
88	57.2	5	227	87	0.05	1	4.0	1
89	57.7	6	213	83	0.075	1	4.0	1
90	56.6	6.3	212	52	0.062	1	3.5	1
91	56.9	6.5	123	64	0.115	1	5.0	1
92	59	6	191	63	0.05	1	3.0	1
93	58.5	6	212	63	0.05	1	4.0	1
94	58.3	3.7	184	67	0.075	2	6.0	1
95	58.8	4	177	67	0.075	1	4.0	1
96	58.5	4.4	159	60	0.062	1	4.0	1
97	59.3	4.4	161	58	0.115	1	4.0	1
98	59.7	5.3	76	55	0.095	1	2.0	1
99	60.9	4.6	222	77	0.05	2	4.0	1
100	61	5.3	130	47	0.075	1	2.0	1
101	62.1	4.4	65	66	0.115	1	4.0	1
102	63.2	5.2	76	60	0.175	1	5.3	1
103	62.6	6.3	185	51	0.095	2	4.0	1
104	63.6	7.5	114	46	0.14	2	5.5	2
105	64.9	7.6	154	39	0.062	2	4.5	1
106	65.1	5.6	213	68	0.05	1	6.0	1
107	64.1	3	93	39	0.075	1	3.5	1
108	66.1	3.5	93	39	0.115	1	3.0	1
109	66.4	3.1	216	77	0.075	1	3.0	1
110	68.4	3.1	167	52	0.095	2	5.0	1
111	68.3	5.6	93	36	0.095	1	4.5	1
112	66.3	6.1	199	82	0.115	1	6.0	1
113	68	7.5	154	39	0.050	2	3.0	1
114	68.9	5.3	166	75	0.05	2	4.0	1
115	69.8	6.5	176	51	0.115	1	4.0	1
116	69.2	6.5	195	54	0.075	1	4.0	1
117	71.3	5.9	197	77	0.062	1	4.0	1
118	71.3	4.8	213	76	0.265	2	4.0	1
119	70.9	6.8	176	71	0.062	1	4.0	1
120	70.9	7.3	176	71	0.05	1	3.0	1
121	71.8	3	234	74	0.05	1	4.5	1
122	72.6	4.5	161	53	0.05	1	4.0	1
123	71.3	4.3	163	45	0.075	1	6.0	1
124	70.2	1	182	38	0.140	1	5.0	1

LOCATION 3 (continued)

Fracture ID	Fracture Position Hor.	Fracture Position Vert.	Dip Azimuth	Dip	Aperture	Morphology*	Length	Fill**
125	72.1	2.8	189	80	0.065	2	3.0	1
126	73.2	3.7	230	81	0.115	1	4.0	1
127	73.8	4.5	157	38	0.062	3	3.5	1
128	73.6	5.7	192	53	0.05	1	5.0	1
129	69.3	6.9	201	51	0.062	1	4.0	1
130	72.8	7.1	174	52	0.05	1	4.0	1
131	72.9	6.7	158	66	0.075	2	5.0	2
132	76.3	3.7	168	84	0.095	3	5.5	1
133	75	3.7	171	52	0.075	2	4.0	1
134	75.8	6	192	50	0.062	1	7.0	1
135	75.9	5.7	183	52	0.115	1	9.0	2
136	77.6	1.7	228	79	0.050	2	5.5	1
137	76.7	5.4	195	72	0.095	1	5.0	1
138	77.7	5.3	157	56	0.115	2	6.0	1
139	78.5	3.9	171	79	0.5	3	3.0	1
140	79.1	5.7	109	88	0.215	2	7.0	1
141	79.6	4.5	211	90	0.215	3	5.0	1
142	82.1	5.9	253	79	0.115	2	9.0	1
143	84.3	5.9	214	72	0.115	3	6.0	1
144	85.4	4.3	3	69	0.065	2	5.0	1
145	86.2	2	73	68	0.065	1	5.0	2
146	90.2	2.2	216	85	0.05	1	4.0	1
147	88.8	2.7	134	78	0.075	1	1.5	1
148	87.8	3.5	205	80	0.05	1	4.0	1
149	87.8	4	183	77	0.05	1	3.0	1
150	87.6	5.4	154	65	0.062	1	4.2	1
151	88.4	5.6	201	70	0.075	1	4.0	1
152	87.7	6.3	211	82	0.05	1	4.0	1
153	86.6	6	178	75	0.062	1	3.0	1
154	87.4	6.3	189	75	0.05	1	4.0	1
155	87	7.3	169	55	0.175	2	4.0	1
156	89.9	6.5	47	81	0.4	2	4.0	1
157	90.5	5.9	177	71	0.05	1	3.0	1
158	90.6	5.3	147	87	0.265	2	5.0	1
159	91.3	2.3	159	52	0.115	2	9.0	1
160	91.5	2.1	168	52	0.062	1	4.0	1
161	90.9	1.1	186	68	0.062	1	4.5	1
162	92	2.4	178	76	0.14	1	6.0	1
163	92.2	3.5	174	58	0.115	1	5.5	1
164	89.2	3.7	212	57	0.05	2	5.0	1
165	92.7	4.8	32	81	0.500	1	8.0	1
166	93.6	4.5	59	85	0.215	3	6.5	1
167	95	1.8	73	88	0.175	2	6.0	1
168	95.5	4.9	73	90	0.175	3	4.0	1
169	98.2	4.1	253	49	0.05	1	4.0	1
170	99.8	3.5	179	56	0.075	2	6.0	1
171	99.4	2.5	154	53	0.05	1	6.0	1
172	99.6	0	182	33	0.050	2	10.0	1
173	101.6	1.3	202	59	0.115	1	4.5	1
174	100.8	1.9	176	66	0.062	2	3.0	1
175	100.9	4.4	206	64	0.05	1	6.0	1
176	101.3	5.9	38	87	0.05	2	6.0	1
177	101.7	6.8	199	63	0.05	2	6.0	1
178	104.6	3.8	192	40	0.175	2	14.0	1
179	104.7	3.3	94	80	0.062	1	6.0	1
180	102.8	7.5	168	28	0.062	2	9.0	2
181	110.1	1.5	194	44	0.062	1	5.0	1
182	107.5	0.2	283	86	0.05	1	3.0	2
183	106.6	1.5	181	68	0.115	3	4.0	1
184	106.6	6.5	175	46	0.115	2	5.5	1
185	106.7	6.8	175	46	0.062	2	3.0	1
186	108	9.8	172	44	0.115	2	5.0	1
187	109.3	7.9	222	90	0.115	2	4.0	1
188	109	8.8	209	50	0.075	1	4.0	1
189	109.8	7.4	212	83	0.175	2	5.0	1
190	110.2	5.8	74	86	0.115	2	5.0	1
191	110.4	5.2	77	84	0.062	1	5.0	1
192	111.1	6.2	75	87	0.115	2	7.0	2
193	112.3	5	88	74	0.33	3	10.0	1
194	113.9	0.9	157	41	0.062	2	4.5	1
195	112.6	6.3	83	82	0.115	1	5.0	1
196	114.8	0.8	86	48	0.095	2	3.5	1
197	116.6	6.5	194	55	0.05	2	3.0	1
198	118.6	4.2	199	84	0.14	2	7.0	1
199	119.7	5.1	223	49	0.062	2	5.0	1
200	119.5	1.6	81	55	0.175	1	5.5	1
201	118.3	0.7	127	52	0.115	2	5.0	1
202	119.2	0.1	114	46	0.095	2	4.5	1
203	119.3	0.1	209	50	0.095	1	2.0	1
204	121.4	5.7	99	51	0.175	2	5.0	1
205	119.7	7.3	200	52	0.095	1	2.0	1
206	117.9	6.6	103	45	0.062	2	2.0	1
207	121.4	1.7	143	46	0.175	1	2.0	1
208	123.2	0	182	55	0.05	2	4.0	1
209	124.8	0	229	80	0.115	2	5.0	1

****Fill**

Filled fracture	1
Partially filled fract.	2
Open fracture	3

***Morphology**

Planar	1
Sub-planar	2
Sinuous	3

LOCATION 4

Fracture ID	Fracture Position		Dip Azimuth	Dip	Aperture	Morphology*	Length	Fill**
	Hor.	Vert.						
1	3.4	2.0	216	68	0.05	2	3.5	1
2	2.6	2.5	6	83	0.05	1	3.5	1
3	2.3	3.0	19	78	0.075	1	3.0	1
4	3.2	3.0	232	59	0.05	1	3.4	1
5	3.7	2.9	0	88	0.062	2	1.8	1
6	2.4	3.8	294	59	0.05	2	3.6	1
7	4.2	3.8	254	54	0.05	2	3.8	1
8	3	4.1	283	33	0.062	2	2.5	1
9	4.1	4.6	334	68	0.05	1	2.1	1
10	3.5	5.0	329	55	0.075	2	1.7	1
11	1.2	4.7	280	25	0.095	2	1.4	1
12	2.3	5.5	264	40	0.05	1	2.3	1
13	2.6	5.8	19	87	0.95	2	0.6	1
14	0.6	5.7	83	77	0.075	2	2.2	1
15	0.2	6.5	303	69	0.062	2	2.3	1
16	2.1	6.8	261	77	0.075	1	3.3	2
17	2.6	6.8	26	86	0.265	2	3.6	1
18	3.3	6.5	194	80	0.175	2	2.0	1
19	3.1	6.1	194	81	0.062	1	2.5	2
20	3.8	7.8	195	87	0.062	1	3.6	1
21	1.8	7.9	324	67	0.095	2	4.4	1
22	3.8	8.4	287	50	0.095	2	3.2	1
23	3.9	9.5	303	52	0.062	1	4.4	1
24	2.2	10.0	1	63	0.05	2	3.6	1
25	2.8	10.1	217	66	0.062	2	4.1	1
26	1.4	10.7	303	45	0.05	1	4.1	1
27	1.7	11.0	307	46	0.05	1	2.1	1
28	2.2	11.0	3	78	0.062	1	2.9	1
29	2.4	11.2	3	78	0.05	2	3.2	1
30	3.4	10.6	276	52	0.05	2	2.6	1
31	3.8	10.3	245	71	0.05	2	2.8	1
32	3.7	11.2	53	90	0.062	1	2.5	1
33	3.8	11.3	24	78	0.062	1	1.1	1
34	4.4	11.2	300	48	0.05	1	2.2	1
35	4	11.5	24	75	0.075	1	3.2	1
36	3	12.0	301	46	0.095	2	2.7	1
37	2.9	12.6	329	61	0.062	1	0.5	1
38	3.7	12.2	264	49	0.05	2	3.0	1
39	1.2	13.4	335	50	0.062	1	4.4	1
40	2.1	14.0	251	79	0.115	1	4.7	1
41	2.9	13.3	345	57	0.05	2	3.0	1
42	2.9	12.7	338	39	0.062	1	2.4	1
43	3.1	12.7	217	88	0.05	1	2.8	1
44	3.7	12.9	308	47	0.05	1	2.3	1
45	3.9	13.5	24	73	0.05	2	2.9	1
46	3.6	14.0	271	51	0.062	2	2.9	1
47	2.2	15.0	326	58	0.075	2	2.0	1
48	3.2	14.5	308	41	0.05	2	2.9	1
49	4.2	2.0	278	60	0.05	1	3.0	1
50	5.1	1.6	17	81	0.05	2	2.0	1
51	4.9	2.5	44	86	0.05	1	2.2	1
52	5.2	2.6	270	61	0.05	1	1.8	1
55	5.7	4.0	304	43	0.05	1	3.1	1
56	6.8	3.7	308	57	0.062	2	2.2	1
57	5.4	5.2	297	49	0.33	2	2.2	1
58	6.6	5.8	299	45	0.062	2	3.7	1
59	4.8	6.0	299	43	0.062	2	2.0	1
60	5.3	6.6	271	42	0.05	2	3.7	1
61	6	6.5	319	35	0.05	2	2.2	1
62	4.8	6.6	276	45	0.062	2	3.1	1
63	5.1	7.2	317	51	0.062	2	2.3	1
64	6.3	7.4	265	57	0.115	2	3.3	1
65	4.6	7.7	17	81	0.075	1	1.8	1
66	5.2	8.0	284	46	0.075	2	3.3	1
67	4.4	8.6	18	78	0.075	1	3.9	1
68	5	9.0	339	57	0.05	1	2.4	1
69	6	8.1	318	61	0.05	2	2.2	1
70	3.9	9.6	206	73	0.075	2	2.0	1
71	5.2	9.3	280	43	0.175	2	1.0	1
72	5.2	10.3	264	72	0.095	2	2.5	1
73	5.2	10.5	277	60	0.095	2	2.0	1
74	5.1	11.6	285	63	0.062	1	2.4	1
75	5.9	12.0	250	59	0.062	1	1.8	1
76	4.9	12.7	240	63	0.062	3	2.2	1
77	6.1	12.3	16	75	0.05	2	2.4	1
78	5.7	12.9	223	57	0.062	1	3.2	1
79	4.8	13.8	340	84	0.095	2	2.9	1
80	4.1	14.1	41	86	0.14	1	6.0	2
81	4.6	14.8	14	78	0.095	1	3.4	1
82	5.8	14.5	345	80	0.075	1	3.5	1
83	6.1	1.0	17	82	0.115	2	2.4	1
84	6.1	2.4	285	41	0.062	2	3.2	1
85	7.2	1.0	241	55	0.075	1	3.5	1
86	7.4	2.0	292	48	0.05	1	2.4	1
87	8.1	0.9	251	55	0.075	2	3.0	1
88	7.9	1.9	288	48	0.062	1	2.8	1
89	7.7	2.3	286	45	0.075	2	2.8	1
90	8.2	2.3	267	52	0.075	2	2.2	1
91	6.2	3.2	329	69	0.14	2	4.0	1
92	7.7	4.1	285	48	0.062	2	2.8	1
93	7.6	4.9	200	63	0.062	2	4.1	1
94	8.7	4.3	262	58	0.095	2	5.5	1
95	9	4.2	20	79	0.062	2	4.2	1
96	8.4	4.8	13	78	0.05	1	2.2	1
97	7.4	5.5	17	84	0.075	2	2.4	1
98	6.9	6.5	248	52	0.062	1	1.1	1
99	6.7	6.8	258	54	0.05	1	3.1	1
100	7.1	6.8	255	57	0.062	2	2.3	1
101	8.2	6.9	303	64	0.062	2	3.0	1
102	8.5	6.8	264	41	0.075	2	3.3	1
103	6.1	8.0	319	57	0.05	1	2.6	1
104	7.4	7.9	338	78	0.062	1	2.9	1
105	8.5	8.2	339	37	0.075	2	2.9	1
106	8.8	8.1	212	82	0.095	2	3.1	1
107	6.2	9.3	256	48	0.062	2	2.6	1
108	6.9	9.0	280	50	0.05	1	2.1	1
109	7.6	9.3	247	60	0.265	2	1.9	2
110	8.6	9.1	309	45	0.062	1	3.0	1
111	9.7	9.0	248	73	0.05	2	2.9	1
112	9.8	9.6	248	73	0.05	2	2.3	1
113	9	9.4	242	80	0.05	1	2.1	1
114	8.4	9.5	312	54	0.062	2	2.7	1
115	6.4	10.2	279	57	0.115	2	1.3	1
116	7	10.0	284	55	0.062	2	2.8	1
117	7.4	10.2	262	66	0.05	2	2.4	1
118	6.1	11.3	240	74	0.075	1	2.5	1
119	6.5	10.7	238	75	0.215	2	3.1	1
120	7	10.8	272	74	0.05	1	3.1	1
121	8.1	10.6	287	57	0.062	1	2.8	1
122	6.5	11.4	261	63	0.115	1	3.8	1
123	7.6	12.6	282	63	0.075	2	2.9	1
124	8.2	13.0	306	68	0.062	1	3.2	1
125	8.2	13.3	31	73	0.062	2	3.5	1
126	6.9	14.5	289	54	0.062	2	2.3	1

LOCATION 4 (continued)

Fracture ID	Fracture Position Hor.	Fracture Position Vert.	Dip Azimuth	Dip	Aperture	Morphology*	Length	Fill**
127	7.8	13.6	261	55	0.062	1	3.4	1
128	8.4	13.4	262	54	0.062	1	3.4	1
129	9.8	13.8	210	77	0.05	1	3.0	1
130	9.7	1.3	297	49	0.05	2	5.1	1
131	10.4	1.6	298	64	0.062	2	3.2	1
132	9.8	2.9	279	55	0.05	1	3.0	1
133	10.4	2.5	14	89	0.062	2	2.5	1
134	11.1	2.7	16	88	0.062	1	2.9	1
135	11.5	2.9	21	89	0.062	2	2.0	1
136	11.4	3.8	312	62	0.062	2	3.0	1
137	10.8	4.4	283	51	0.075	1	2.2	1
138	10.3	5.0	273	57	0.062	1	0.8	1
139	9.6	5.4	262	45	0.075	1	1.1	1
140	9.8	5.5	261	43	0.062	1	3.4	1
141	10.5	5.6	18	85	0.062	2	2.4	1
143	11.4	5.1	239	69	0.062	1	3.1	1
144	10.8	6.3	270	49	0.075	1	1.1	1
145	9.1	7.9	287	58	0.075	2	2.5	1
146	9.5	8.0	328	57	0.095	1	0.5	1
147	10	7.2	295	49	0.062	2	2.1	1
148	11.5	6.5	262	51	0.05	1	2.6	1
149	12.1	6.3	241	57	0.14	1	0.9	2
150	11.3	7.0	302	47	0.05	2	1.6	1
151	10.4	8.3	310	62	0.05	2	2.0	1
152	10.3	8.8	289	57	0.05	2	1.0	1
153	11.1	8.5	286	46	0.05	2	2.3	1
154	11.5	8.3	13	84	0.05	1	2.2	1
155	11.4	7.8	222	63	0.095	1	1.4	1
156	12.1	8.5	294	46	0.05	2	2.5	1
157	12	7.3	300	49	0.062	2	2.4	1
158	10.7	9.4	302	56	0.062	1	2.0	1
159	11	9.2	298	65	0.05	1	2.0	1
160	11.9	8.8	214	89	0.062	1	2.5	1
161	12.1	9.6	284	59	0.05	2	2.2	1
162	10.6	10.1	14	82	0.062	2	2.3	1
163	11.7	10.2	255	56	0.062	1	3.3	1
164	12.7	9.9	298	53	0.05	1	1.2	1
165	11.7	10.5	262	62	0.05	1	3.2	1
166	11.1	11.2	288	48	0.075	1	2.9	1
167	11.6	10.8	239	60	0.062	2	2.5	1
168	12.6	10.4	246	57	0.075	2	2.4	1
169	9.2	11.8	268	71	0.062	2	2.2	1
170	9.9	12.3	266	56	0.075	2	3.5	1
171	9.7	12.5	273	57	0.062	2	3.6	1
172	9.8	13.0	249	49	0.05	1	3.4	1
173	9.3	13.4	235	85	0.062	1	4.2	1
174	10.3	12.4	3	86	0.062	1	4.0	1
175	10.7	12.1	247	70	0.075	1	2.2	1
176	10.7	12.4	309	63	0.062	2	3.1	1
177	11	13.4	271	88	0.062	2	2.2	1
178	9.7	14.4	16	71	0.05	1	2.1	1
179	11.3	14.4	282	56	0.095	2	4.2	1
180	12.2	15.0	265	57	0.062	1	2.5	1
181	11.4	13.8	20	86	0.05	1	1.8	1
182	11.8	13.9	174	90	0.075	1	1.0	1
183	13.2	12.0	112	59	0.14	3	5.1	1
184	12.2	1.7	273	44	0.05	2	1.1	1
185	13.1	2.0	16	76	0.062	1	2.8	2
186	13.2	0.9	11	77	0.14	1	2.7	1
187	13.7	1.5	11	78	0.062	1	2.8	1
188	14.5	2.9	281	71	0.062	2	2.6	1
189	12.2	4.0	287	68	0.075	2	2.1	1

Fracture ID	Fracture Position Hor.	Fracture Position Vert.	Dip Azimuth	Dip	Aperture	Morphology*	Length	Fill**
190	13.1	4.5	269	51	0.095	1	2.2	1
191	14	5.3	257	48	0.05	2	2.1	1
192	14.8	5.3	263	49	0.062	1	2.5	1
193	14.1	7.1	267	63	0.062	1	4.6	1
194	14.5	7.0	237	63	0.062	1	3.6	1
195	15.1	6.9	242	62	0.062	2	3.0	1
196	15.5	5.9	268	56	0.062	2	2.6	2
197	13.7	7.5	243	60	0.075	1	4.5	1
198	14.1	7.9	242	75	0.05	2	2.9	1
199	13.9	8.5	258	65	0.062	1	4.0	1
200	14.6	7.9	264	53	0.062	1	5.1	1
201	14.8	8.9	266	60	0.05	2	4.0	1
202	14.4	9.2	19	72	0.062	1	4.9	1
203	15.6	8.8	279	58	0.075	1	5.1	1
204	13.7	10.1	340	73	0.062	1	4.9	1

****Fill**

Filled fracture	1
Partially filled fract.	2
Open fracture	3

***Morphology**

Planar	1
Sub-planar	2
Sinuous	3

LOCATION 5

Fracture ID	Fracture Position		Dip Azimuth	Dip	Aperture	Morphology*	Length	Fill**
	Hor.	Vert.						
1	0.2	10.6	258	77	0.075	1	3.9	1
2	0.3	11.0	238	73	0.75	2	5.6	1
3	0.4	9.9	138	83	0.062	2	2.6	1
4	0.5	3.1	78	87	0.095	1	3.4	1
5	0.6	7.4	149	44	0.14	2	3.6	1
6	0.7	3.4	191	57	0.062	1	1.8	1
7	0.7	3.5	192	57	0.062	1	1.7	1
8	1.0	6.3	177	86	1.15	3	10.5	1
9	1.0	9.1	258	75	0.115	1	2.6	1
10	1.1	2.2	258	31	0.05	1	1.2	1
11	1.1	7.6	207	53	0.075	1	2.4	1
12	1.3	3.4	134	59	0.062	2	2.1	1
13	1.3	4.9	106	67	0.095	2	2.2	1
14	1.4	1.0	98	70	0.075	1	1.7	1
15	1.6	7.5	205	71	0.05	1	4.0	1
16	1.7	5.8	209	59	0.05	2	2.3	1
17	1.8	12.0	177	35	0.062	2	2.0	1
18	1.9	4.8	213	45	0.05	1	1.9	1
19	2.1	2.5	129	60	0.05	1	2.5	1
20	2.1	1.3	271	76	0.05	1	3.0	1
21	2.1	4.4	138	41	0.05	1	3.1	1
22	2.2	4.4	138	41	0.05	1	3.1	1
23	2.2	4.2	245	71	0.05	1	2.6	1
24	2.3	10.8	204	57	0.062	2	2.4	1
25	2.4	1.8	271	76	0.075	1	2.4	2
26	2.4	3.8	276	84	0.062	2	3.9	1
27	2.8	13.0	134	29	0.062	2	2.6	1
28	2.8	1.8	271	76	0.05	1	1.8	1
29	2.9	6.2	251	58	0.05	2	3.4	1
30	3.0	2.3	171	49	0.05	2	6.1	1
31	3.1	3.2	278	89	0.075	1	2.6	1
32	3.4	2.9	279	89	0.05	1	1.8	1
33	3.4	5.0	169	59	0.075	2	3.4	1
34	3.5	5.4	173	53	0.075	2	2.2	1
35	3.6	4.3	197	53	0.05	1	3.8	1
36	3.7	8.5	244	70	0.062	2	3.0	1
37	3.9	3.9	237	61	0.115	1	1.9	1
38	3.9	4.3	259	50	0.062	1	2.9	1
39	3.9	6.5	209	69	0.062	2	2.7	1
40	3.9	8.0	179	71	0.075	2	3.0	1
41	3.9	9.7	112	75	0.33	2	3.6	1
42	3.9	10.8	211	61	0.05	1	3.0	1
43	4.0	10.4	207	57	0.05	1	5.0	1
44	4.1	5.2	207	52	0.05	2	2.4	1
45	4.1	6.2	169	61	0.05	2	3.0	1
46	4.1	10.2	219	54	0.05	2	3.7	1
47	4.2	12.1	191	37	0.05	1	4.0	1
48	4.4	13.2	125	53	0.05	1	5.0	1
49	4.5	9.3	203	58	0.062	2	3.4	1
50	4.6	8.1	106	86	0.265	2	5.0	1
51	4.6	12.6	126	48	0.062	1	3.5	1
52	4.7	11.0	109	75	0.05	1	2.3	1
53	4.8	6.0	181	58	0.05	2	0.8	1
54	5.1	8.0	74	84	0.05	1	1.4	1
55	5.2	10.7	97	50	0.05	2	2.0	1
56	5.3	13.4	122	54	0.075	1	5.0	2
57	5.3	10.8	174	47	0.05	1	3.0	1
58	5.4	9.5	212	34	0.062	1	5.8	1
59	5.6	1.5	168	43	0.062	2	5.5	1
60	5.6	5.1	162	47	0.095	2	3.2	1
61	5.6	5.5	164	56	0.062	2	4.0	1
62	5.7	4.2	134	84	0.14	2	3.0	1
63	5.8	8.0	236	67	0.175	1	3.5	1
64	5.8	2.5	181	44	0.062	1	4.9	1
65	5.9	10.0	165	61	0.14	2	4.0	2
66	6.0	8.6	82	86	0.062	2	0.8	1
67	6.0	12.0	128	71	0.05	2	3.0	1
68	6.2	12.5	162	34	0.05	2	3.5	1
69	6.4	11.5	168	85	0.05	2	3.0	1
70	6.6	11.5	137	46	0.05	2	3.2	1
71	6.6	12.0	303	41	0.05	2	5.0	1
72	7.0	10.2	99	59	0.062	1	1.0	1
73	7.0	12.4	202	25	0.05	3	7.5	1
74	7.0	3.5	177	39	0.062	2	4.0	1
75	7.2	9.2	100	69	0.215	1	2.5	2
76	7.3	4.1	256	53	0.062	2	4.5	1
77	7.4	5.5	210	46	0.062	2	3.4	1
78	7.4	13.6	216	31	0.075	1	6.0	2
79	7.5	6.0	205	32	0.05	1	4.0	1
80	7.6	8.8	176	65	0.4	3	6.0	1
81	7.6	12.6	179	37	0.05	1	4.0	1
82	7.6	1.8	62	90	0.05	1	2.5	1
83	7.6	0.8	172	40	0.075	2	3.0	1
84	7.9	11.7	248	58	0.075	2	3.0	1
85	8.0	4.8	243	62	0.062	2	2.5	1
86	8.5	9.7	91	68	0.075	1	4.2	1
87	8.6	3.7	142	43	0.05	1	3.0	1
88	8.6	8.9	113	51	0.115	2	2.0	1
89	8.6	11.0	134	47	0.05	2	4.5	1
90	8.8	4.4	237	44	0.075	1	5.0	1
91	8.9	10.7	94	70	0.062	1	3.5	1
92	9.0	4.9	123	53	0.062	1	3.5	1
93	9.0	11.4	235	59	0.095	2	3.0	1
94	9.0	11.9	176	43	0.075	1	7.5	1
95	9.1	13.6	236	33	0.265	2	3.5	1
96	9.2	12.0	123	58	0.05	2	3.4	1
97	9.3	10.0	123	38	0.05	2	4.0	1
98	9.4	8.9	124	58	0.075	2	2.8	1
99	9.5	2.3	219	40	0.062	2	4.0	1
100	9.6	5.9	250	67	0.075	1	3.5	1
101	9.8	8.9	131	48	0.05	1	3.5	1
102	9.9	8.8	125	42	0.05	2	2.4	1
103	10.0	11.4	177	31	0.05	2	4.0	1
104	10.0	14.2	238	53	0.175	2	3.0	1
105	10.1	7.4	248	62	0.062	2	1.4	1
106	10.2	12.8	262	80	0.075	2	5.5	1
107	10.2	1.7	116	46	0.062	1	6.6	1
108	10.3	1.3	137	37	0.05	1	3.0	1
109	10.4	14.2	216	67	0.062	2	4.0	1
110	10.6	7.3	115	49	0.05	1	3.4	1
111	10.6	9.5	137	44	0.05	1	3.0	1
112	10.6	9.8	152	39	0.062	2	2.9	1
113	10.6	13.4	183	52	0.062	2	3.5	1
114	10.7	1.8	154	51	0.062	2	7.0	1
115	10.7	3.0	307	79	0.33	2	2.0	3
116	10.9	12.1	183	82	0.062	2	4.0	1
117	11.0	6.3	115	50	0.062	2	3.2	1
118	11.0	11.2	132	35	0.05	2	4.0	1
119	11.1	10.1	152	39	0.05	1	4.0	1
120	11.3	4.9	104	57	0.095	2	3.5	1
121	11.4	1.2	219	41	0.095	2	4.6	1
122	11.4	6.1	132	45	0.05	2	2.5	1
123	11.6	2.4	177	58	0.075	2	2.4	1
124	11.7	7.5	119	65	0.062	2	3.0	1

LOCATION 5 (continued)

Fracture ID	Fracture Position Hor.	Fracture Position Vert.	Dip Azimuth	Dip	Aperture	Morphology*	Length	Fill**
125	11.8	11.6	32	90	0.5	3	10.0	1
126	11.8	13.5	90	70	0.115	2	2.4	1
127	12.0	6.2	125	62	0.05	2	3.4	1
128	12.1	6.6	130	50	0.05	2	3.6	1
129	12.2	14.4	127	59	0.14	3	2.0	1
130	12.2	5.2	283	86	0.075	1	1.2	1
131	12.2	6.0	93	78	0.05	1	3.0	1
132	12.4	2.4	103	78	0.075	2	3.0	1
133	13.0	3.0	112	54	0.075	1	3.0	1
134	13.4	4.3	83	52	0.062	2	2.0	1
135	13.8	2.3	271	83	0.115	3	10.0	1
136	14.4	3.7	140	49	0.05	2	1.2	1
137	14.4	8.2	222	38	0.062	2	4.0	1
138	14.4	11.1	147	48	0.062	2	5.5	1
139	14.5	4.4	248	47	0.062	2	4.0	1
140	14.8	10.6	156	46	0.05	2	5.5	1
141	14.8	13.8	226	62	0.4	2	1.5	1
142	15.0	8.3	159	42	0.05	2	4.5	1
143	15.3	10.7	160	56	0.075	2	6.0	1
144	15.3	4.6	277	49	0.075	2	1.3	1
145	15.4	13.5	117	57	0.05	2	3.4	1
146	15.4	14.2	222	62	0.5	2	1.8	1
147	15.5	11.5	252	73	0.062	2	3.3	1
148	15.6	1.7	134	75	0.05	2	5.5	1
149	16.0	8.0	296	88	0.095	2	3.5	2
150	16.0	11.9	235	55	0.14	2	3.3	1
151	16.0	14.0	237	60	0.062	2	6.0	1
152	16.0	3.6	123	53	0.062	2	4.5	1
153	16.2	9.4	169	52	0.062	2	4.0	1
154	16.4	13.1	237	68	0.075	2	7.0	1
155	16.4	14.2	127	40	0.05	2	3.5	1
156	16.6	2.5	115	43	0.075	2	4.4	1
157	16.8	5.1	264	59	0.075	2	3.0	1
158	16.9	14.6	181	44	0.115	2	4.4	1
159	17.0	9.8	253	79	0.062	2	4.0	1
160	17.2	9.2	253	79	0.115	2	3.5	1
161	17.7	14.1	189	52	0.095	2	3.0	1
162	17.8	3.3	115	69	0.05	2	4.0	1
163	17.8	8.5	252	51	0.05	2	3.5	1
164	18.0	5.8	115	41	0.062	1	4.0	1
165	18.0	11.6	147	49	0.075	2	3.0	1
166	18.1	5.6	102	47	0.062	1	4.0	1
167	18.2	7.6	178	44	0.05	1	4.0	1
168	18.3	13.5	171	82	0.075	3	5.0	1
169	18.4	4.4	227	40	0.075	2	5.0	1
170	18.5	13.0	138	48	0.075	2	5.5	1
171	18.5	2.7	145	44	0.075	2	4.5	1
172	18.5	3.3	177	48	0.05	2	4.0	1
173	18.6	2.5	171	45	0.05	2	6.0	1
174	18.9	7.1	119	45	0.062	3	6.0	1
175	18.9	10.0	169	36	0.075	2	5.0	1
176	19.5	6.6	262	58	0.05	2	2.2	1
177	19.5	12.0	155	50	0.062	1	5.5	1
178	19.5	14.5	131	42	0.062	2	4.5	1
179	19.6	10.6	164	41	0.062	2	5.5	1
180	20.0	10.0	141	47	0.062	2	7.0	1
181	20.2	13.6	119	37	0.05	2	3.4	1
182	20.4	12.5	262	82	0.215	2	5.0	1
183	20.4	14.0	159	39	0.05	2	1.2	1
184	20.6	5.4	102	32	0.095	2	7.5	1
185	20.6	7.7	212	38	0.062	2	3.5	1
186	21.0	10.0	317	45	0.14	2	3.5	3
187	21.4	6.1	198	30	0.05	2	4.5	1
188	21.5	11.4	187	46	0.05	2	4.4	1
189	21.6	2.5	198	43	0.075	2	4.5	1
190	22.0	8.9	128	57	0.14	2	2.5	1
191	22.0	10.2	178	62	0.05	2	3.3	1
192	22.0	2.1	116	90	0.075	1	3.3	1
193	22.3	12.5	187	49	0.062	2	6.0	1
194	22.6	13.0	124	41	0.075	1	4.4	1
195	23.5	5.3	216	53	0.075	1	2.5	1
196	24.0	13.4	247	51	0.095	2	6.0	1
197	24.0	2.5	77	77	0.075	1	5.0	1
198	24.0	4.0	259	81	0.14	1	10.0	1
199	24.4	2.5	84	42	0.05	1	5.0	1
200	24.5	13.4	258	44	0.075	2	4.5	1

**Fill	
Filled fracture	1
Partially filled fract.	2
Open fracture	3

*Morphology	
Planar	1
Sub-planar	2
Sinuous	3

Appendix B. Location 1

Fracture ID	Strike	Dip	Rotation to horizontal		Weighting factor (f_1)	Rotation about vertical Axis		obs. length	Weight factor (f_2)	f_1*f_2
			Strike	Dip		Strike	Dip			
1	270	63	90	58	1.18	155	58	6.56	1.84	2.17
2	270	69	92	52	1.27	157	52	6.46	1.87	2.37
3	270	47	88	73	1.05	153	73	6.67	1.81	1.89
4	271	53	90	68	1.08	155	68	6.56	1.84	1.98
5	271	88	99	33	1.84	164	33	6.19	1.95	3.58
6	271	48	89	73	1.05	154	73	6.61	1.82	1.91
7	272	41	88	80	1.02	153	80	6.67	1.81	1.84
8	272	37	88	84	1.01	153	84	6.67	1.81	1.82
9	273	68	95	53	1.25	160	53	6.33	1.91	2.39
10	273	48	90	73	1.05	155	73	6.56	1.84	1.92
11	275	61	95	60	1.15	160	60	6.33	1.91	2.20
12	277	81	105	42	1.49	170	42	6.04	2.00	2.99
13	278	84	108	40	1.56	173	40	5.99	2.01	3.13
14	278	88	111	36	1.70	176	36	5.96	2.02	3.44
15	279	63	100	60	1.15	165	60	6.16	1.96	2.26
16	280	63	101	60	1.15	166	60	6.13	1.97	2.27
17	281	85	113	40	1.56	178	40	5.95	2.03	3.15
18	281	52	98	71	1.06	163	71	6.22	1.94	2.05
19	282	51	98	72	1.05	163	72	6.22	1.94	2.04
20	283	56	101	67	1.09	166	67	6.13	1.97	2.14
21	283	72	108	52	1.27	173	52	5.99	2.01	2.56
22	284	52	100	71	1.06	165	71	6.16	1.96	2.07
23	288	87	124	42	1.49	189	42	6.03	2.00	2.99
24	288	60	107	65	1.10	172	65	6.01	2.01	2.22
25	289	80	119	48	1.35	184	48	5.97	2.02	2.72
26	292	66	113	62	1.13	178	62	5.95	2.03	2.30
27	292	87	128	44	1.44	193	44	6.11	1.98	2.84
28	294	75	121	55	1.22	186	55	5.98	2.02	2.46
29	295	72	120	58	1.18	185	58	5.97	2.02	2.38
30	296	78	125	54	1.24	190	54	6.04	2.00	2.47
31	296	56	111	72	1.05	176	72	5.96	2.02	2.13
32	297	54	111	74	1.04	176	74	5.96	2.02	2.11
33	297	53	110	75	1.04	175	75	5.97	2.02	2.09
34	298	61	115	69	1.07	180	69	5.95	2.03	2.17
35	298	57	113	72	1.05	178	72	5.95	2.03	2.13
36	298	47	108	81	1.01	173	81	5.99	2.01	2.04
37	298	57	113	72	1.05	178	72	5.95	2.03	2.13
38	298	51	110	77	1.03	175	77	5.97	2.02	2.07
39	298	64	117	66	1.09	182	66	5.95	2.03	2.22
40	301	78	130	57	1.19	195	57	6.16	1.96	2.34
41	302	87	138	51	1.29	203	51	6.47	1.87	2.40
42	302	83	135	54	1.24	200	54	6.34	1.91	2.35
43	302	58	117	73	1.05	182	73	5.95	2.03	2.12
44	302	74	127	61	1.14	192	61	6.08	1.98	2.27
45	303	59	118	73	1.05	183	73	5.96	2.03	2.12

Appendix B. Location 1 (continued)

Fracture ID	Strike	Dip	Rotation to horizontal		Weighting factor (f_1)	Rotation about vertical Axis		obs. length	Weight factor (f_2)	f_1*f_2
			Strike	Dip		Strike	Dip			
46	303	61	119	71	1.06	184	71	5.97	2.02	2.14
47	303	60	119	72	1.05	184	72	5.97	2.02	2.13
48	303	66	122	67	1.09	187	67	6.00	2.01	2.19
49	304	88	141	52	1.27	206	52	6.63	1.82	2.31
50	304	55	116	77	1.03	181	77	5.95	2.03	2.08
51	305	8	267	66	1.09	332	66	6.73	1.79	1.96
52	306	77	133	61	1.14	198	61	6.26	1.93	2.20
53	306	70	128	66	1.09	193	66	6.11	1.98	2.16
54	307	81	137	59	1.17	202	59	6.42	1.88	2.19
55	307	67	126	69	1.07	191	69	6.06	1.99	2.13
56	307	75	132	63	1.12	197	63	6.22	1.94	2.18
57	308	56	119	78	1.02	184	78	5.97	2.02	2.07
58	312	52	119	83	1.01	184	83	5.97	2.02	2.04
59	316	49	119	87	1.00	184	87	5.97	2.02	2.03
60	316	84	146	64	1.11	211	64	6.95	1.74	1.93
61	316	60	127	80	1.02	192	80	6.08	1.98	2.01
62	316	89	151	61	1.14	216	61	7.36	1.64	1.87
63	318	62	130	80	1.02	195	80	6.16	1.96	1.99
64	321	62	132	82	1.01	197	82	6.22	1.94	1.96
65	321	58	129	84	1.01	194	84	6.13	1.97	1.98
66	321	41	296	85	1.00	1	85	5.95	2.03	2.04
67	322	68	137	78	1.02	202	78	6.42	1.88	1.92
68	322	87	153	67	1.09	218	67	7.56	1.60	1.73
69	323	58	130	85	1.00	195	85	6.16	1.96	1.97
70	327	68	140	82	1.01	205	82	6.57	1.84	1.86
71	333	53	311	85	1.00	16	85	6.19	1.95	1.96
72	334	57	314	87	1.00	19	87	6.29	1.92	1.92
73	339	62	321	86	1.00	26	86	6.62	1.82	1.83
74	343	86	164	85	1.00	229	85	9.09	1.33	1.33
75	345	84	163	88	1.00	228	88	8.91	1.35	1.36
76	347	52	316	75	1.04	21	75	6.37	1.89	1.96
77	349	84	345	89	1.00	50	89	9.26	1.30	1.30
78	351	79	341	85	1.00	46	85	8.57	1.41	1.41
79	351	87	348	89	1.00	53	89	9.89	1.22	1.22
80	351	49	314	71	1.06	19	71	6.29	1.92	2.03
81	354	64	329	75	1.04	34	75	7.18	1.68	1.74
82	358	84	349	81	1.01	54	81	10.12	1.19	1.21
83	3	49	317	62	1.13	22	62	6.42	1.88	2.13
84	5	86	355	76	1.03	60	76	12.07	1.00	1.03
85	5	56	325	63	1.12	30	63	6.87	1.76	1.97
86	6	39	307	58	1.18	12	58	6.08	1.98	2.34
87	28	83	5	55	1.22	70	55	11.17	1.08	1.32
88	38	88	17	49	1.33	82	49	10.60	1.14	1.51
89	38	35	299	39	1.59	4	39	5.96	2.02	3.22
90	44	80	13	40	1.56	78	40	10.73	1.12	1.75

Appendix B. Location 1 (continued)

Fracture ID	Strike	Dip	Rotation to horizontal		Weighting factor (f_1)	Rotation about vertical Axis		obs. length	Weight factor (f_2)	f_1*f_2
			Strike	Dip		Strike	Dip			
91	67	84	49	27	2.20	114	27	11.50	1.05	2.31
92	81	84	81	24	2.46	146	24	7.17	1.68	4.14
93	81	89	81	29	2.06	146	29	7.17	1.68	3.47
94	82	83	84	23	2.56	149	23	6.93	1.74	4.45
95	83	90	85	30	2.00	150	30	6.86	1.76	3.52
96	85	46	249	14	4.13	314	14	8.54	1.41	5.84
97	88	86	97	27	2.20	162	27	6.25	1.93	4.25
98	92	85	106	27	2.20	171	27	6.02	2.00	4.41
99	112	86	135	39	1.59	200	39	6.34	1.91	3.03
100	118	87	141	44	1.44	206	44	6.63	1.82	2.62
101	122	83	149	45	1.41	214	45	7.18	1.68	2.38
102	127	89	146	52	1.27	211	52	6.95	1.74	2.20
103	127	84	151	49	1.33	216	49	7.36	1.64	2.17
104	132	86	153	55	1.22	218	55	7.56	1.60	1.95
105	137	69	175	51	1.29	240	51	12.07	1.00	1.29
106	137	69	175	51	1.29	240	51	11.59	1.04	1.34
107	138	85	158	59	1.17	223	59	8.15	1.48	1.73
108	145	75	172	60	1.15	237	60	10.95	1.10	1.27
109	148	84	165	67	1.09	230	67	9.27	1.30	1.41
110	148	64	185	58	1.18	250	58	10.69	1.13	1.33
111	149	76	173	64	1.11	238	64	11.26	1.07	1.19
112	156	86	167	75	1.04	232	75	9.68	1.25	1.29
113	159	83	171	76	1.03	236	76	10.67	1.13	1.17
114	160	64	189	68	1.08	254	68	10.45	1.16	1.25
115	160	64	189	68	1.08	254	68	10.45	1.16	1.25
116	167	75	182	79	1.02	247	79	10.91	1.11	1.13
117	167	80	178	82	1.01	243	82	11.27	1.07	1.08
118	168	64	193	75	1.04	258	75	10.27	1.18	1.22
119	176	61	199	80	1.02	264	80	10.10	1.19	1.21
120	177	72	190	86	1.00	255	86	10.40	1.16	1.16
121	178	78	185	90	1.00	250	90	10.69	1.13	1.13
122	180	84	1	85	1.00	66	85	11.49	1.05	1.05
123	182	75	9	88	1.00	74	88	10.92	1.11	1.11
124	186	78	9	83	1.01	74	83	10.92	1.11	1.11
125	193	78	13	78	1.02	78	78	10.73	1.12	1.15
126	194	70	20	82	1.01	85	82	10.54	1.15	1.16
127	197	40	225	82	1.01	290	82	10.70	1.13	1.14
128	201	50	39	89	1.00	104	89	10.82	1.12	1.12
129	203	78	19	70	1.06	84	70	10.56	1.14	1.22
130	208	33	235	82	1.01	300	82	11.83	1.02	1.03
131	219	88	22	51	1.29	87	51	10.51	1.15	1.48
132	220	74	35	61	1.14	100	61	10.66	1.13	1.29
133	222	88	25	49	1.33	90	49	10.50	1.15	1.52
134	225	89	27	46	1.39	92	46	10.51	1.15	1.60
135	230	88	33	44	1.44	98	44	10.60	1.14	1.64

Appendix B. Location 1 (continued)

Fracture ID	Strike	Dip	Rotation to horizontal		Weighting factor (f_1)	Rotation about vertical Axis		obs. length	Weight factor (f_2)	f_1*f_2
			Strike	Dip		Strike	Dip			
136	233	62	54	64	1.11	119	64	12.01	1.00	1.12
137	235	49	61	75	1.04	126	75	10.10	1.19	1.24
138	236	51	61	73	1.05	126	73	10.10	1.19	1.25
139	236	44	64	79	1.02	129	79	9.44	1.28	1.30
140	238	90	41	37	1.66	106	37	10.93	1.10	1.84
141	238	68	55	56	1.21	120	56	12.07	1.00	1.21
142	238	65	57	59	1.17	122	59	11.20	1.08	1.26
143	239	59	60	64	1.11	125	64	10.35	1.17	1.30
144	240	45	66	77	1.03	131	77	9.05	1.33	1.37
145	240	57	62	66	1.09	127	66	9.87	1.22	1.34
146	241	77	54	47	1.37	119	47	12.01	1.00	1.37
147	241	56	63	67	1.09	128	67	9.64	1.25	1.36
148	242	62	62	61	1.14	127	61	9.87	1.22	1.40
149	243	52	66	70	1.06	131	70	9.05	1.33	1.42
150	244	61	64	61	1.14	129	61	9.44	1.28	1.46
151	244	63	63	59	1.17	128	59	9.64	1.25	1.46
152	245	66	63	56	1.21	128	56	9.64	1.25	1.51
153	246	76	61	46	1.39	126	46	10.10	1.19	1.66
154	246	84	57	39	1.59	122	39	11.20	1.08	1.71
155	247	43	71	78	1.02	136	78	8.26	1.46	1.49
156	247	90	54	33	1.84	119	33	12.01	1.00	1.85
157	247	63	66	59	1.17	131	59	9.05	1.33	1.56
158	248	59	68	62	1.13	133	62	8.71	1.39	1.57
159	249	87	60	35	1.74	125	35	10.35	1.17	2.03
160	249	26	256	86	1.00	321	86	7.64	1.58	1.58
161	252	80	67	41	1.52	132	41	8.88	1.36	2.07
162	253	53	74	67	1.09	139	67	7.87	1.53	1.67
163	253	49	75	71	1.06	140	71	7.76	1.56	1.65
164	255	51	76	69	1.07	141	69	7.65	1.58	1.69
165	255	69	74	51	1.29	139	51	7.87	1.53	1.97
166	255	82	71	38	1.62	136	38	8.26	1.46	2.37
167	255	68	74	52	1.27	139	52	7.87	1.53	1.95
168	256	68	75	52	1.27	140	52	7.76	1.56	1.97
169	256	46	77	74	1.04	142	74	7.54	1.60	1.67
170	256	56	76	64	1.11	141	64	7.65	1.58	1.76
171	257	67	76	53	1.25	141	53	7.65	1.58	1.98
172	258	66	78	54	1.24	143	54	7.44	1.62	2.00
173	258	68	77	52	1.27	142	52	7.54	1.60	2.03
174	258	46	79	74	1.04	144	74	7.35	1.64	1.71
175	259	34	80	86	1.00	145	86	7.26	1.66	1.67
176	259	59	79	61	1.14	144	61	7.35	1.64	1.88
177	259	79	78	41	1.52	143	41	7.44	1.62	2.47
178	259	69	79	51	1.29	144	51	7.35	1.64	2.11
179	260	60	80	60	1.15	145	60	7.26	1.66	1.92
180	260	58	80	62	1.13	145	62	7.26	1.66	1.88

Appendix B. Location 1 (continued)

Fracture ID	Strike	Dip	Rotation to horizontal		Weighting factor (f_1)	Rotation about vertical Axis		obs. length	Weight factor (f_2)	f_1*f_2
			Strike	Dip		Strike	Dip			
181	261	66	81	54	1.24	146	54	7.17	1.68	2.08
182	261	59	81	61	1.14	146	61	7.17	1.68	1.92
183	261	62	81	58	1.18	146	58	7.17	1.68	1.99
184	261	76	81	44	1.44	146	44	7.17	1.68	2.42
185	261	86	81	34	1.79	146	34	7.17	1.68	3.01
186	261	43	81	77	1.03	146	77	7.17	1.68	1.73
187	261	46	81	74	1.04	146	74	7.17	1.68	1.75
188	261	64	81	56	1.21	146	56	7.17	1.68	2.03
189	261	43	81	77	1.03	146	77	7.17	1.68	1.73
190	262	70	82	50	1.31	147	50	7.09	1.70	2.22
191	262	78	82	42	1.49	147	42	7.09	1.70	2.55
192	262	51	82	69	1.07	147	69	7.09	1.70	1.82
193	263	44	82	76	1.03	147	76	7.09	1.70	1.76
194	264	67	84	53	1.25	149	53	6.93	1.74	2.18
195	265	86	88	34	1.79	153	34	6.67	1.81	3.23
196	266	57	86	63	1.12	151	63	6.80	1.78	1.99
197	267	43	85	77	1.03	150	77	6.86	1.76	1.80
198	267	82	91	38	1.62	156	38	6.51	1.85	3.01
199	267	63	87	57	1.19	152	57	6.73	1.79	2.14
200	267	75	89	45	1.41	154	45	6.61	1.82	2.58
201	268	77	91	44	1.44	156	44	6.51	1.85	2.67
202	268	61	88	59	1.17	153	59	6.67	1.81	2.11
203	268	52	87	68	1.08	152	68	6.73	1.79	1.93
204	269	77	92	44	1.44	157	44	6.46	1.87	2.69

Appendix B. Location 2

Fracture ID	Strike	Dip	Rotation to horizontal		Weighting factor (f_1)	Rotation about Vertical Axis		obs. length	Weight factor (f_2)	f_1*f_2
			Strike	Dip		Strike	Dip			
1	348	76	162	56	1.21	172	56	5.96	6.71	8.09
2	262	89	274	68	1.08	284	68	24.08	1.66	1.79
3	262	89	274	68	1.08	284	68	24.08	1.66	1.79
4	270	65	301	62	1.13	311	62	8.96	4.46	5.05
5	78	67	252	81	1.01	262	81	39.94	1.00	1.01
6	129	62	94	58	1.18	104	58	24.23	1.65	1.94
7	185	80	169	27	2.20	179	27	5.90	6.77	14.91
8	35	90	227	38	1.62	237	38	10.86	3.68	5.97
9	20	82	201	42	1.49	211	42	6.89	5.80	8.66
10	126	84	113	72	1.05	123	72	10.81	3.70	3.89
11	145	83	124	56	1.21	134	56	8.48	4.71	5.68
12	19	89	200	35	1.74	210	35	6.82	5.86	10.21
13	346	57	170	73	1.05	180	73	5.90	6.77	7.08
14	163	89	146	46	1.39	156	46	6.45	6.19	8.60
15	354	87	162	43	1.47	172	43	5.96	6.71	9.83
16	308	36	343	73	1.05	353	73	5.94	6.72	7.03
17	70	72	250	72	1.05	260	72	34.29	1.16	1.22
18	77	82	263	70	1.06	273	70	39.56	1.01	1.07
19	111	85	106	85	1.00	116	85	13.42	2.98	2.99
20	25	70	206	54	1.24	216	54	7.30	5.47	6.76
21	113	81	103	81	1.01	113	81	15.04	2.65	2.69
22	34	88	224	39	1.59	234	39	10.06	3.97	6.31
23	64	62	239	76	1.03	249	76	16.53	2.42	2.49
24	92	65	79	88	1.00	89	88	39.51	1.01	1.01
25	92	65	79	88	1.00	89	88	39.51	1.01	1.01
26	72	81	258	67	1.09	268	67	39.52	1.01	1.10
27	287	81	295	84	1.01	305	84	10.24	3.90	3.92
28	37	85	226	43	1.47	236	43	10.58	3.78	5.54
29	29	72	211	53	1.25	221	53	7.83	5.10	6.39
30	77	81	262	70	1.06	272	70	39.53	1.01	1.08
31	288	84	293	87	1.00	303	87	10.78	3.70	3.71
32	18	72	198	52	1.27	208	52	6.69	5.97	7.58
33	334	78	148	62	1.13	158	62	6.36	6.28	7.11
34	58	81	247	57	1.19	257	57	26.41	1.51	1.80
35	175	87	158	38	1.62	168	38	6.03	6.62	10.76
36	142	82	121	58	1.18	131	58	8.98	4.45	5.25
37	44	83	234	48	1.35	244	48	13.50	2.96	3.98
38	126	67	97	63	1.12	107	63	20.08	1.99	2.23
39	52	74	237	60	1.15	247	60	15.16	2.64	3.04
40	95	52	70	79	1.02	80	79	33.98	1.18	1.20
41	207	83	217	28	2.13	227	28	8.67	4.61	9.82
42	147	71	113	48	1.35	123	48	10.81	3.70	4.97
43	159	69	118	37	1.66	128	37	9.56	4.18	6.94
44	73	67	249	77	1.03	259	77	31.18	1.28	1.31
45	28	68	209	57	1.19	219	57	7.60	5.25	6.26

Appendix B. Location 2 (continued)

Fracture ID	Strike	Dip	Rotation to horizontal		Weighting factor (f_1)	Rotation about Vertical Axis		obs. length	Weight factor (f_2)	f_1*f_2
			Strike	Dip		Strike	Dip			
46	321	64	148	81	1.01	158	81	6.36	6.28	6.36
47	341	67	161	67	1.09	171	67	5.97	6.69	7.27
48	209	77	226	23	2.56	236	23	10.58	3.78	9.67
49	4	79	179	47	1.37	189	47	5.98	6.68	9.14
50	32	68	213	58	1.18	223	58	8.08	4.94	5.83
51	43	69	225	60	1.15	235	60	10.31	3.87	4.47
52	195	85	192	29	2.06	202	29	6.37	6.27	12.94
53	318	55	153	89	1.00	163	89	6.17	6.48	6.48
54	327	74	145	70	1.06	155	70	6.51	6.14	6.53
55	349	84	158	48	1.35	168	48	6.03	6.62	8.91
56	331	63	156	76	1.03	166	76	6.08	6.57	6.77
57	29	71	211	54	1.24	221	54	7.83	5.10	6.31
58	127	85	115	71	1.06	125	71	10.26	3.89	4.12
59	22	67	202	57	1.19	212	57	6.96	5.74	6.84
60	144	82	123	56	1.21	133	56	8.64	4.62	5.58
61	185	72	159	20	2.92	169	20	6.01	6.65	19.44
62	135	76	111	60	1.15	121	60	11.43	3.50	4.04
63	199	86	200	30	2.00	210	30	6.82	5.86	11.71
64	177	87	161	37	1.66	171	37	5.97	6.69	11.11
65	329	67	152	74	1.04	162	74	6.20	6.44	6.70
66	350	67	169	63	1.12	179	63	5.90	6.77	7.60
67	300	57	322	81	1.01	332	81	6.67	5.99	6.06
68	300	71	310	89	1.00	320	89	7.68	5.20	5.20
69	97	86	278	83	1.01	288	83	18.91	2.11	2.13
70	227	58	291	24	2.46	301	24	11.40	3.51	8.62
71	281	68	303	72	1.05	313	72	8.62	4.63	4.87
72	282	70	302	74	1.04	312	74	8.79	4.55	4.73
73	299	6	11	57	1.19	21	57	6.32	6.32	7.54
74	300	72	310	89	1.00	320	89	7.68	5.20	5.20
75	1	59	182	67	1.09	192	67	6.03	6.62	7.19
76	12	69	191	55	1.22	201	55	6.32	6.32	7.71
77	17	89	196	35	1.74	206	35	6.57	6.08	10.60
78	22	89	205	35	1.74	215	35	7.21	5.54	9.66
79	323	82	136	67	1.09	146	67	7.11	5.62	6.10
80	4	88	175	38	1.62	185	38	5.92	6.74	10.95
81	184	79	166	26	2.28	176	26	5.91	6.75	15.41
82	213	87	226	34	1.79	236	34	10.58	3.78	6.75
83	304	69	134	89	1.00	144	89	7.28	5.48	5.48
84	338	60	163	74	1.04	173	74	5.94	6.72	6.99
85	194	81	189	25	2.37	199	25	6.24	6.40	15.14
86	198	83	198	27	2.20	208	27	6.69	5.97	13.15
87	23	76	205	48	1.35	215	48	7.21	5.54	7.45
88	194	84	190	28	2.13	200	28	6.28	6.36	13.54
89	191	83	183	28	2.13	193	28	6.06	6.59	14.04

Appendix B. Location 2 (continued)

Fracture ID	Strike	Dip	Rotation to horizontal		Weighting factor (f_1)	Rotation about Vertical Axis		obs. length	Weight factor (f_2)	f_1*f_2
			Strike	Dip		Strike	Dip			
90	88	84	271	77	1.03	281	77	30.42	1.31	1.35
91	356	52	180	75	1.04	190	75	5.99	6.66	6.90
92	12	86	188	38	1.62	198	38	6.21	6.43	10.45
93	181	85	166	33	1.84	176	33	5.91	6.75	12.40
94	341	50	170	81	1.01	180	81	5.90	6.77	6.85
95	9	90	182	35	1.74	192	35	6.03	6.62	11.54
96	12	61	192	63	1.12	202	63	6.37	6.27	7.04
97	150	73	117	46	1.39	127	46	9.78	4.08	5.68
98	16	77	195	47	1.37	205	47	6.51	6.13	8.38
99	306	67	137	89	1.00	147	89	7.03	5.68	5.68
100	286	82	294	84	1.01	304	84	10.50	3.80	3.82
101	288	61	313	74	1.04	323	74	7.37	5.42	5.64
102	37	74	221	53	1.25	231	53	9.39	4.25	5.32
103	20	60	200	64	1.11	210	64	6.82	5.86	6.52
104	22	74	203	50	1.31	213	50	7.04	5.67	7.40
105	24	71	205	53	1.25	215	53	7.21	5.54	6.94
106	151	78	124	48	1.35	134	48	8.48	4.71	6.34
107	27	87	213	38	1.62	223	38	8.08	4.94	8.03
108	152	79	126	48	1.35	136	48	8.19	4.88	6.56
109	38	52	214	74	1.04	224	74	8.21	4.86	5.06
110	316	16	2	65	1.10	12	65	6.03	6.62	7.31
111	338	55	165	78	1.02	175	78	5.92	6.74	6.90
112	352	37	183	90	1.00	193	90	6.06	6.59	6.59
113	27	65	207	60	1.15	217	60	7.40	5.40	6.24
114	20	54	200	70	1.06	210	70	6.82	5.86	6.23
115	31	83	217	43	1.47	227	43	8.67	4.61	6.76
116	14	57	194	67	1.09	204	67	6.46	6.18	6.71
117	273	66	301	65	1.10	311	65	8.96	4.46	4.92
118	131	56	88	54	1.24	98	54	39.89	1.00	1.24
119	25	59	205	65	1.10	215	65	7.21	5.54	6.11
120	279	31	341	57	1.19	351	57	5.97	6.69	7.98
121	40	72	223	56	1.21	233	56	9.82	4.07	4.90
122	15	47	196	77	1.03	206	77	6.57	6.08	6.24
123	228	81	253	37	1.66	263	37	39.79	1.00	1.67
124	46	75	231	56	1.21	241	56	12.20	3.27	3.95
125	269	79	287	68	1.08	297	68	12.92	3.09	3.34
126	269	79	287	68	1.08	297	68	12.92	3.09	3.34
127	281	63	308	70	1.06	318	70	7.92	5.05	5.37
128	119	82	107	76	1.03	117	76	12.96	3.08	3.18
129	34	40	208	85	1.00	218	85	7.50	5.33	5.35
130	109	86	105	87	1.00	115	87	13.91	2.87	2.87
131	312	75	134	80	1.02	144	80	7.28	5.48	5.57
132	359	76	174	51	1.29	184	51	5.92	6.75	8.69
133	33	58	212	67	1.09	222	67	7.95	5.02	5.46

Appendix B. Location 2 (continued)

Fracture ID	Strike	Dip	Rotation to horizontal		Weighting factor (f_1)	Rotation about Vertical Axis		obs. length	Weight factor (f_2)	f_1*f_2
			Strike	Dip		Strike	Dip			
134	31	56	210	69	1.07	220	69	7.71	5.18	5.55
135	35	45	210	80	1.02	220	80	7.71	5.18	5.26
136	169	74	135	32	1.89	145	32	7.19	5.55	10.48
137	106	84	102	88	1.00	112	88	15.69	2.55	2.55
138	34	54	212	72	1.05	222	72	7.95	5.02	5.28
139	100	48	68	73	1.05	78	73	28.38	1.41	1.47
140	163	74	129	36	1.70	139	36	7.81	5.12	8.70
141	31	59	210	66	1.09	220	66	7.71	5.18	5.67
142	37	50	213	76	1.03	223	76	8.08	4.94	5.09
143	28	50	206	75	1.04	216	75	7.30	5.47	5.66
144	147	81	124	53	1.25	134	53	8.48	4.71	5.90
145	29	51	207	74	1.04	217	74	7.40	5.40	5.62
146	31	57	210	68	1.08	220	68	7.71	5.18	5.59
147	29	57	208	68	1.08	218	68	7.50	5.33	5.75
148	29	49	207	76	1.03	217	76	7.40	5.40	5.57
149	26	66	207	58	1.18	217	58	7.40	5.40	6.37
150	25	64	205	60	1.15	215	60	7.21	5.54	6.40
151	31	50	208	75	1.04	218	75	7.50	5.33	5.52
152	74	80	259	69	1.07	269	69	39.50	1.01	1.08
153	1	41	187	84	1.01	197	84	6.17	6.47	6.51
154	22	41	201	83	1.01	211	83	6.89	5.80	5.84
155	23	44	202	80	1.02	212	80	6.96	5.74	5.82
156	32	44	208	81	1.01	218	81	7.50	5.33	5.39
157	28	52	206	73	1.05	216	73	7.30	5.47	5.72
158	22	53	201	71	1.06	211	71	6.89	5.80	6.13
159	10	49	192	75	1.04	202	75	6.37	6.27	6.49
160	2	60	183	66	1.09	193	66	6.06	6.59	7.22
161	22	44	201	80	1.02	211	80	6.89	5.80	5.89
162	22	62	202	62	1.13	212	62	6.96	5.74	6.50
163	199	78	201	22	2.67	211	22	6.89	5.80	15.47
164	87	59	71	88	1.00	81	88	37.72	1.06	1.06
165	36	45	211	81	1.01	221	81	7.83	5.10	5.17
166	18	42	198	82	1.01	208	82	6.69	5.97	6.03
167	44	36	33	89	1.00	43	89	8.07	4.95	4.95
168	108	90	288	90	1.00	298	90	12.49	3.20	3.20
169	318	72	140	77	1.03	150	77	6.81	5.87	6.02
170	24	36	202	88	1.00	212	88	6.96	5.74	5.74
171	27	39	204	85	1.00	214	85	7.12	5.61	5.63
172	105	32	54	63	1.12	64	63	13.46	2.97	3.33
173	308	61	323	89	1.00	333	89	6.61	6.04	6.04
174	297	59	319	80	1.02	329	80	6.87	5.81	5.90
175	26	58	205	66	1.09	215	66	7.21	5.54	6.06
176	33	62	213	64	1.11	223	64	8.08	4.94	5.50
177	89	68	259	88	1.00	269	88	39.50	1.01	1.01
178	23	53	202	71	1.06	212	71	6.96	5.74	6.07

Appendix B. Location 2 (continued)

Fracture ID	Strike	Dip	Rotation to horizontal		Weighting factor (f_1)	Rotation about Vertical Axis		obs. length	Weight factor (f_2)	f_1*f_2
			Strike	Dip		Strike	Dip			
179	34	57	212	69	1.07	222	69	7.95	5.02	5.38
180	31	73	214	52	1.27	224	52	8.21	4.86	6.17
181	133	88	121	68	1.08	131	68	8.98	4.45	4.80
182	64	59	237	78	1.02	247	78	15.16	2.64	2.69
183	110	61	84	73	1.05	94	73	39.60	1.01	1.05
184	48	79	236	53	1.25	246	53	14.56	2.74	3.44
185	317	88	127	68	1.08	137	68	8.06	4.96	5.35
186	316	39	344	79	1.02	354	79	5.93	6.73	6.86
187	41	52	217	75	1.04	227	75	8.67	4.61	4.77
188	37	56	215	70	1.06	225	70	8.36	4.78	5.09
189	42	53	218	74	1.04	228	74	8.83	4.52	4.70
190	53	55	227	76	1.03	237	76	10.86	3.68	3.79
191	48	59	225	71	1.06	235	71	10.31	3.87	4.10
192	52	59	228	72	1.05	238	72	11.16	3.58	3.76
193	19	67	199	57	1.19	209	57	6.75	5.92	7.05
194	26	54	205	70	1.06	215	70	7.21	5.54	5.89
195	304	87	120	79	1.02	130	79	9.16	4.36	4.44
196	25	53	204	71	1.06	214	71	7.12	5.61	5.93
197	45	57	222	72	1.05	232	72	9.60	4.16	4.37
198	58	63	235	72	1.05	245	72	14.01	2.85	3.00
199	49	51	222	78	1.02	232	78	9.60	4.16	4.25
200	5	79	180	47	1.37	190	47	5.99	6.66	9.11
201	359	72	176	55	1.22	186	55	5.93	6.73	8.22
202	93	58	74	83	1.01	84	83	39.71	1.01	1.01
203	29	52	207	73	1.05	217	73	7.40	5.40	5.65
204	7	76	184	49	1.33	194	49	6.08	6.57	8.70
205	99	64	82	83	1.01	92	83	39.53	1.01	1.02
206	354	66	173	62	1.13	183	62	5.91	6.76	7.66
207	354	60	176	68	1.08	186	68	5.93	6.73	7.26
208	356	62	177	65	1.10	187	65	5.95	6.72	7.41
209	61	64	238	73	1.05	248	73	15.81	2.53	2.64
210	150	75	120	47	1.37	130	47	9.16	4.36	5.96
211	258	80	279	60	1.15	289	60	17.96	2.22	2.57
212	258	80	279	60	1.15	289	60	17.96	2.22	2.57
213	21	54	201	70	1.06	211	70	6.89	5.80	6.17
214	202	76	209	20	2.92	219	20	7.60	5.25	15.36
215	203	76	212	20	2.92	222	20	7.95	5.02	14.69

Appendix B. Location 3

Fracture ID	Strike	Dip	Rotation to horizontal		Weighting factor (f_1)	Rotation about Vertical Axis		obs. length	Weight factor (f_2)	f_1*f_2
			Strike	Dip		Strike	Dip			
1	273	89	296	51	1.29	249	51	13.67	4.58	5.89
2	273	69	321	43	1.47	274	43	62.56	1.00	1.47
3	277	71	319	47	1.37	272	47	62.44	1.00	1.37
4	337	83	152	74	1.04	271	74	62.41	1.00	1.04
5	356	48	191	81	1.01	268	81	62.43	1.00	1.02
6	119	50	93	86	1.00	276	86	45.50	1.38	1.38
7	122	57	101	87	1.00	278	87	34.43	1.82	1.82
8	139	80	128	83	1.01	98	83	35.21	1.78	1.79
9	118	36	81	80	1.02	99	80	31.32	2.00	2.03
10	49	19	47	84	1.01	119	84	10.11	6.19	6.23
11	73	45	245	74	1.04	105	74	18.93	3.31	3.44
12	133	49	97	76	1.03	107	76	16.76	3.73	3.85
13	140	73	122	79	1.02	116	79	11.18	5.60	5.70
14	119	50	93	86	1.00	133	86	7.18	8.71	8.73
15	343	68	168	77	1.03	121	77	9.51	6.58	6.75
16	343	88	150	67	1.09	103	67	21.78	2.87	3.12
17	343	90	148	66	1.09	101	66	25.68	2.44	2.67
18	344	86	153	67	1.09	106	67	17.78	3.52	3.82
19	345	87	152	65	1.10	105	65	18.93	3.31	3.65
20	346	87	153	65	1.10	106	65	17.78	3.52	3.88
21	140	81	129	83	1.01	133	83	7.18	8.71	8.78
22	329	85	146	80	1.02	129	80	7.79	8.04	8.16
23	326	85	145	83	1.01	135	83	6.93	9.03	9.10
24	346	55	180	83	1.01	135	83	6.93	9.03	9.10
25	347	88	152	63	1.12	105	63	18.93	3.31	3.71
26	347	54	182	83	1.01	135	83	6.93	9.03	9.10
27	347	84	156	65	1.10	109	65	15.05	4.16	4.59
28	146	66	117	72	1.05	126	72	8.34	7.51	7.89
29	350	67	173	72	1.05	126	72	8.34	7.51	7.89
30	144	74	125	76	1.03	131	76	7.47	8.38	8.64
31	147	87	138	79	1.02	136	79	6.81	9.19	9.36
32	163	79	137	61	1.14	115	61	11.59	5.40	6.17
33	139	87	135	86	1.00	146	86	5.91	10.59	10.62
34	102	53	268	81	1.01	144	81	6.06	10.33	10.46
35	358	74	172	62	1.13	125	62	8.54	7.33	8.30
36	122	52	96	85	1.00	153	85	5.50	11.38	11.42
37	123	53	97	85	1.00	153	85	5.50	11.38	11.42
38	139	89	136	87	1.00	155	87	5.41	11.58	11.59
39	163	49	102	54	1.24	124	54	8.76	7.14	8.83
40	9	51	197	73	1.05	150	73	5.66	11.06	11.57
41	337	80	154	76	1.03	156	76	5.36	11.67	12.03
42	16	28	32	90	1.00	345	90	5.07	12.35	12.35
43	193	86	164	38	1.62	131	38	7.47	8.38	13.61

Appendix B. Location 3 (continued)

Fracture ID	Strike	Dip	Rotation to horizontal		Weighting factor (f_1)	Rotation about Vertical Axis		obs. length	Weight factor (f_2)	f_1*f_2
			Strike	Dip		Strike	Dip			
44	350	67	173	72	1.05	163	72	5.12	12.22	12.84
45	24	46	210	72	1.05	163	72	5.12	12.22	12.84
46	78	28	60	89	1.00	171	89	4.96	12.62	12.62
47	29	49	212	68	1.08	165	68	5.07	12.34	13.31
48	33	64	211	53	1.25	164	53	5.10	12.28	15.37
49	36	49	218	67	1.09	171	67	4.96	12.62	13.71
50	351	61	178	76	1.03	172	76	4.95	12.65	13.04
51	37	52	218	64	1.11	171	64	4.96	12.62	14.04
52	38	48	220	67	1.09	173	67	4.94	12.68	13.77
53	40	47	221	68	1.08	174	68	4.93	12.70	13.70
54	42	56	222	59	1.17	175	59	4.92	12.72	14.85
55	43	62	223	53	1.25	176	53	4.91	12.74	15.96
56	44	78	223	37	1.66	176	37	4.91	12.74	21.17
57	47	73	227	42	1.49	180	42	4.90	12.77	19.09
58	47	44	227	71	1.06	180	71	4.90	12.77	13.51
59	48	59	228	56	1.21	181	56	4.90	12.77	15.41
60	138	79	127	84	1.01	0	84	4.90	12.77	12.84
61	50	55	230	60	1.15	183	60	4.91	12.76	14.73
62	51	45	230	70	1.06	183	70	4.91	12.76	13.57
63	51	45	230	70	1.06	183	70	4.91	12.76	13.57
64	335	66	166	84	1.01	182	84	4.90	12.77	12.84
65	346	60	176	80	1.02	183	80	4.91	12.76	12.95
66	159	90	146	69	1.07	184	69	4.91	12.74	13.65
67	56	76	241	40	1.56	194	40	5.05	12.39	19.28
68	56	49	234	67	1.09	187	67	4.94	12.68	13.77
69	57	87	248	30	2.00	201	30	5.25	11.93	23.85
70	3	39	200	85	1.00	186	85	4.93	12.70	12.75
71	59	69	242	48	1.35	195	48	5.07	12.34	16.60
72	59	80	247	37	1.66	200	37	5.21	12.00	19.94
73	159	27	76	58	1.18	194	58	5.05	12.39	14.61
74	62	67	245	50	1.31	198	50	5.15	12.15	15.86
75	62	51	240	66	1.09	193	66	5.03	12.45	13.62
76	3	39	200	85	1.00	188	85	4.95	12.65	12.70
77	64	69	248	49	1.33	201	49	5.25	11.93	15.80
78	64	69	248	49	1.33	201	49	5.25	11.93	15.80
79	125	41	87	78	1.02	190	78	4.98	12.58	12.86
80	64	39	237	78	1.02	190	78	4.98	12.58	12.86
81	64	65	247	53	1.25	200	53	5.21	12.00	15.03
82	64	53	242	64	1.11	195	64	5.07	12.34	13.73
83	338	71	163	79	1.02	192	79	5.01	12.49	12.73
84	67	56	246	62	1.13	199	62	5.18	12.08	13.68
85	13	45	203	76	1.03	193	76	5.03	12.45	12.83
86	68	66	251	53	1.25	205	53	5.41	11.58	14.50

Appendix B. Location 3 (continued)

Fracture ID	Strike	Dip	Rotation to horizontal		Weighting factor (f_1)	Rotation about Vertical Axis		obs. length	Weight factor (f_2)	f_1*f_2
			Strike	Dip		Strike	Dip			
87	68	67	252	53	1.25	204	53	5.36	11.67	14.61
88	69	60	249	59	1.17	202	59	5.28	11.84	13.82
89	69	52	246	67	1.09	199	67	5.18	12.08	13.12
90	71	58	250	62	1.13	203	62	5.32	11.76	13.32
91	71	53	248	66	1.09	201	66	5.25	11.93	13.05
92	72	69	257	52	1.27	210	52	5.66	11.06	14.04
93	86	51	257	74	1.04	198	74	5.15	12.15	12.64
94	61	59	241	58	1.18	211	58	5.72	10.95	12.91
95	76	75	265	50	1.31	218	50	6.22	10.07	13.14
96	53	46	231	69	1.07	205	69	5.41	11.58	12.40
97	3	36	202	87	1.00	195	87	5.07	12.34	12.36
98	78	84	275	44	1.44	228	44	7.32	8.55	12.30
99	78	52	252	70	1.06	205	70	5.41	11.58	12.32
100	92	33	69	89	1.00	13	89	5.03	12.45	12.45
101	79	55	255	68	1.08	208	68	5.55	11.28	12.16
102	81	61	260	64	1.11	213	64	5.84	10.71	11.92
103	81	70	266	56	1.21	219	56	6.31	9.93	11.97
104	81	52	255	71	1.06	208	71	5.55	11.28	11.93
105	81	79	274	50	1.31	227	50	7.18	8.71	11.37
106	82	60	260	65	1.10	213	65	5.84	10.71	11.82
107	64	39	237	78	1.02	204	78	5.36	11.67	11.93
108	24	46	210	72	1.05	209	72	5.60	11.17	11.75
109	84	59	261	67	1.09	214	67	5.91	10.59	11.50
110	83	52	256	72	1.05	210	72	5.66	11.06	11.63
111	84	58	260	68	1.08	213	68	5.84	10.71	11.55
112	82	44	251	78	1.02	207	78	5.50	11.38	11.64
113	85	46	254	78	1.02	207	78	5.50	11.38	11.64
114	85	46	254	78	1.02	207	78	5.50	11.38	11.64
115	92	55	264	74	1.04	210	74	5.66	11.06	11.51
116	86	71	271	59	1.17	224	59	6.81	9.19	10.72
117	86	71	271	59	1.17	224	59	6.81	9.19	10.72
118	86	66	267	62	1.13	220	62	6.40	9.79	11.08
119	87	55	261	71	1.06	214	71	5.91	10.59	11.20
120	87	71	272	59	1.17	226	59	7.05	8.87	10.35
121	87	67	269	62	1.13	222	62	6.59	9.49	10.75
122	87	72	273	59	1.17	225	59	6.93	9.03	10.54
123	88	62	266	67	1.09	219	67	6.31	9.93	10.78
124	159	33	83	57	1.19	229	57	7.47	8.38	9.99
125	159	40	91	57	1.19	230	57	7.62	8.21	9.79
126	89	62	267	67	1.09	220	67	6.40	9.79	10.63
127	84	52	257	72	1.05	216	72	6.06	10.33	10.87
128	77	52	252	69	1.07	220	69	6.40	9.79	10.48
129	91	74	278	60	1.15	231	60	7.79	8.04	9.28

Appendix B. Location 3 (continued)

Fracture ID	Strike	Dip	Rotation to horizontal		Weighting factor (f_1)	Rotation about Vertical Axis		obs. length	Weight factor (f_2)	f_1*f_2
			Strike	Dip		Strike	Dip			
130	91	68	273	64	1.11	226	64	7.05	8.87	9.87
131	78	32	242	87	1.00	205	87	5.41	11.58	11.59
132	127	69	113	89	1.00	22	89	5.28	11.84	11.85
133	101	63	275	74	1.04	217	74	6.14	10.20	10.61
134	93	52	262	77	1.03	215	77	5.98	10.46	10.74
135	93	77	282	60	1.15	235	60	8.54	7.33	8.46
136	94	67	274	67	1.09	227	67	7.18	8.71	9.46
137	36	40	219	76	1.03	219	76	6.31	9.93	10.23
138	351	55	183	79	1.02	216	79	6.06	10.33	10.53
139	96	68	276	68	1.08	229	68	7.47	8.38	9.04
140	97	71	279	66	1.09	232	66	7.96	7.86	8.61
141	99	80	289	62	1.13	242	62	10.44	6.00	6.79
142	99	75	284	65	1.10	237	65	9.00	6.96	7.68
143	302	81	318	74	1.04	228	74	7.32	8.55	8.89
144	104	55	271	81	1.01	221	81	6.49	9.64	9.76
145	347	54	182	83	1.01	219	83	6.31	9.93	10.00
146	102	40	258	90	1.00	211	90	5.72	10.95	10.95
147	104	74	286	70	1.06	239	70	9.51	6.58	7.00
148	132	77	123	88	1.00	215	88	5.98	10.46	10.47
149	123	83	304	81	1.01	224	81	6.81	9.19	9.30
150	347	54	182	83	1.01	223	83	6.70	9.34	9.41
151	89	56	263	72	1.05	238	72	9.25	6.77	7.12
152	53	35	230	80	1.02	229	80	7.47	8.38	8.51
153	107	77	291	71	1.06	244	71	11.18	5.60	5.92
154	109	82	296	70	1.06	249	70	13.67	4.58	4.87
155	106	60	276	80	1.02	233	80	8.14	7.69	7.81
156	91	61	267	69	1.07	251	69	15.05	4.16	4.45
157	92	38	252	87	1.00	224	87	6.81	9.19	9.20
158	137	87	134	88	1.00	224	88	6.81	9.19	9.19
159	85	46	254	78	1.02	240	78	9.80	6.39	6.53
160	52	31	229	84	1.01	231	84	7.79	8.04	8.08
161	67	41	240	76	1.03	251	76	15.05	4.16	4.29
162	59	31	233	85	1.00	237	85	9.00	6.96	6.98
163	117	56	278	90	1.00	231	90	7.79	8.04	8.04
164	109	63	280	80	1.02	34	80	5.91	10.59	10.75
165	118	83	302	77	1.03	255	77	18.93	3.31	3.39
166	28	27	218	89	1.00	234	89	8.34	7.51	7.51
167	343	53	180	86	1.00	46	86	7.05	8.87	8.89
168	354	43	193	86	1.00	46	86	7.05	8.87	8.89
169	95	55	266	76	1.03	263	76	40.21	1.56	1.60
170	121	82	302	80	1.02	255	80	18.93	3.31	3.36
171	64	31	235	85	1.00	49	85	7.47	8.38	8.41
172	122	63	286	90	1.00	239	90	9.51	6.58	6.58

Appendix B. Location 3 (continued)

Fracture ID	Strike	Dip	Rotation to horizontal		Weighting factor (f_1)	Rotation about Vertical Axis		obs. length	Weight factor (f_2)	f_1*f_2
			Strike	Dip		Strike	Dip			
173	110	52	271	87	1.00	54	87	8.34	7.51	7.52
174	122	83	304	80	1.02	257	80	21.78	2.87	2.92
175	116	64	284	85	1.00	50	85	7.62	8.21	8.24
176	308	87	315	81	1.01	257	81	21.78	2.87	2.91
177	137	87	134	88	1.00	244	88	11.18	5.60	5.60
178	123	76	298	85	1.00	251	85	15.05	4.16	4.17
179	124	83	304	82	1.01	257	82	21.78	2.87	2.90
180	124	72	295	87	1.00	248	87	13.08	4.79	4.79
181	111	70	287	78	1.02	40	78	6.40	9.79	10.00
182	126	78	301	86	1.00	254	86	17.78	3.52	3.53
183	126	77	300	87	1.00	253	87	16.76	3.73	3.74
184	102	50	266	83	1.01	260	83	28.22	2.22	2.23
185	119	59	281	89	1.00	66	89	12.05	5.20	5.20
186	104	44	262	88	1.00	76	88	20.25	3.09	3.09
187	132	90	314	86	1.00	267	86	62.48	1.00	1.00
188	115	80	298	76	1.03	50	76	7.62	8.21	8.46
189	111	51	271	88	1.00	87	88	62.48	1.00	1.00
190	123	68	291	88	1.00	87	88	62.48	1.00	1.00
191	112	59	278	84	1.01	80	84	28.22	2.22	2.23
192	317	81	325	87	1.00	89	87	62.41	1.00	1.00
193	315	82	323	86	1.00	88	86	62.44	1.00	1.00
194	105	54	270	83	1.01	81	83	31.32	2.00	2.01
195	67	38	239	79	1.02	75	79	18.93	3.31	3.37
196	126	85	307	83	1.01	82	83	35.21	1.78	1.79
197	121	90	310	76	1.03	78	76	23.57	2.66	2.74
198	105	72	285	72	1.05	70	72	14.33	4.37	4.59
199	95	51	263	79	1.02	91	79	62.41	1.00	1.02
200	88	75	276	57	1.19	36	57	6.06	10.33	12.32
201	76	65	258	58	1.18	29	58	5.60	11.17	13.17
202	109	84	298	69	1.07	99	69	31.32	2.00	2.14
203	88	76	277	57	1.19	44	57	6.81	9.19	10.96
204	353	82	162	61	1.14	90	61	62.40	1.00	1.15
205	4	80	171	54	1.24	55	54	8.54	7.33	9.06
206	19	88	178	38	1.62	117	38	10.79	5.80	9.42
207	249	68	313	21	2.79	266	21	62.59	1.00	2.79
208	257	82	291	34	1.79	244	34	11.18	5.60	10.01

Appendix B. Location 4

Fracture ID	Strike	Dip	Rotation to horizontal		Weighting factor (f_1)	Rotation about Vertical Axis		obs. length	Weight factor (f_2)	f_1*f_2
			Strike	Dip		Strike	Dip			
1	126	68	139	89	1.00	109	89	8.25	0.91	0.91
2	276	83	100	77	1.03	70	77	8.30	0.90	0.93
3	289	78	282	90	1.00	252	90	8.20	0.92	0.92
4	142	59	335	84	1.01	305	84	9.54	0.79	0.79
5	270	88	101	69	1.07	71	69	8.25	0.91	0.97
6	204	59	24	59	1.17	354	59	7.54	0.99	1.16
7	164	54	352	75	1.04	322	75	9.49	0.79	0.82
8	193	33	18	86	1.00	348	86	7.66	0.98	0.98
9	244	68	66	63	1.12	36	63	9.27	0.81	0.91
10	239	55	54	71	1.06	24	71	8.21	0.91	0.97
11	190	25	199	86	1.00	169	86	7.64	0.98	0.98
12	174	40	6	83	1.01	336	83	8.20	0.91	0.92
13	289	87	110	86	1.00	80	86	7.92	0.95	0.95
14	156	54	347	79	1.02	317	79	10.22	0.73	0.75
15	353	77	315	33	1.84	285	33	8.08	0.93	1.70
16	213	69	35	50	1.31	5	50	7.53	1.00	1.30
17	171	77	342	53	1.25	312	53	10.52	0.71	0.89
18	296	86	292	87	1.00	262	87	7.87	0.95	0.95
19	104	80	119	76	1.03	89	76	7.80	0.96	0.99
20	104	81	118	76	1.03	88	76	7.80	0.96	0.99
21	105	87	113	80	1.02	83	80	7.86	0.95	0.97
22	234	67	57	58	1.18	27	58	8.42	0.89	1.05
23	197	50	18	68	1.08	348	68	7.66	0.98	1.06
24	213	52	32	66	1.09	2	66	7.50	1.00	1.09
25	271	63	80	84	1.01	50	84	10.18	0.74	0.74
26	127	66	142	89	1.00	112	89	8.42	0.89	0.89
27	213	45	31	73	1.05	1	73	7.50	1.00	1.05
28	217	46	34	73	1.05	4	73	7.52	1.00	1.04
29	273	78	94	77	1.03	64	77	8.67	0.86	0.89
30	273	78	94	77	1.03	64	77	8.67	0.86	0.89
31	186	52	9	68	1.08	339	68	8.02	0.93	1.01
32	155	71	333	67	1.09	303	67	9.31	0.81	0.87
33	323	90	309	66	1.09	279	66	7.90	0.95	1.04
34	294	78	284	85	1.00	254	85	8.11	0.92	0.93
35	210	48	29	70	1.06	359	70	7.50	1.00	1.06
36	294	75	281	84	1.01	251	84	8.24	0.91	0.91
37	211	46	30	72	1.05	0	72	7.50	1.00	1.05
38	239	61	57	66	1.09	27	66	8.42	0.89	0.98
39	174	49	1	75	1.04	331	75	8.56	0.88	0.91
40	245	50	55	77	1.03	25	77	8.28	0.91	0.93
41	161	79	331	58	1.18	301	58	9.11	0.82	0.97

Appendix B. Location 4 (continued)

Fracture ID	Strike	Dip	Rotation to horizontal		Weighting factor (f_1)	Rotation about Vertical Axis		obs. length	Weight factor (f_2)	f_1*f_2
			Strike	Dip		Strike	Dip			
42	255	57	66	77	1.03	36	77	9.27	0.81	0.83
43	248	39	50	88	1.00	20	88	7.98	0.94	0.94
44	127	88	302	80	1.02	272	80	7.81	0.96	0.98
45	218	47	35	72	1.05	5	72	7.53	1.00	1.05
46	294	73	279	83	1.01	249	83	8.35	0.90	0.91
47	181	51	5	71	1.06	335	71	8.26	0.91	0.96
48	236	58	53	67	1.09	23	67	8.15	0.92	1.00
49	218	41	34	78	1.02	4	78	7.52	1.00	1.02
50	188	60	8	60	1.15	338	60	8.08	0.93	1.07
51	287	81	103	87	1.00	73	87	8.15	0.92	0.92
52	314	86	301	71	1.06	271	71	7.80	0.96	1.02
53	180	61	0	62	1.13	330	62	8.64	0.87	0.98
54	209	51	28	67	1.09	358	67	7.50	1.00	1.09
55	94	85	109	69	1.07	79	69	7.94	0.94	1.01
56	214	43	31	75	1.04	1	75	7.50	1.00	1.04
57	218	57	37	62	1.13	7	62	7.56	0.99	1.12
58	207	49	27	69	1.07	357	69	7.51	1.00	1.07
59	209	45	28	73	1.05	358	73	7.50	1.00	1.05
60	209	43	28	75	1.04	358	75	7.50	1.00	1.03
61	181	42	9	79	1.02	339	79	8.02	0.93	0.95
62	229	35	39	86	1.00	9	86	7.59	0.99	0.99
63	186	45	11	75	1.04	341	75	7.92	0.95	0.98
64	227	51	43	70	1.06	13	70	7.70	0.97	1.04
65	175	57	358	67	1.09	328	67	8.83	0.85	0.92
66	287	81	103	87	1.00	73	87	8.15	0.92	0.92
67	194	46	17	73	1.05	347	73	7.69	0.98	1.02
68	288	78	101	90	1.00	71	90	8.25	0.91	0.91
69	249	57	62	74	1.04	32	74	8.84	0.85	0.88
70	228	61	48	61	1.14	18	61	7.89	0.95	1.09
71	116	73	131	83	1.01	101	83	7.95	0.94	0.95
72	190	43	15	76	1.03	345	76	7.76	0.97	1.00
73	174	72	348	55	1.22	318	55	10.06	0.75	0.91
74	187	60	7	60	1.15	337	60	8.14	0.92	1.06
75	195	63	14	56	1.21	344	56	7.80	0.96	1.16
76	160	59	346	73	1.05	316	73	10.39	0.72	0.75
77	150	63	336	76	1.03	306	76	9.66	0.78	0.80
78	286	75	98	89	1.00	68	89	8.41	0.89	0.89
79	133	57	152	88	1.00	122	88	9.20	0.82	0.82
80	250	84	84	55	1.22	54	55	9.64	0.78	0.95
81	311	86	299	74	1.04	269	74	7.80	0.96	1.00
82	284	78	99	86	1.00	69	86	8.35	0.90	0.90

Appendix B. Location 4 (continued)

Fracture ID	Strike	Dip	Rotation to horizontal		Weighting factor (f_1)	Rotation about Vertical Axis		obs. length	Weight factor (f_2)	f_1*f_2
			Strike	Dip		Strike	Dip			
83	255	80	84	61	1.14	54	61	9.64	0.78	0.89
84	287	82	104	87	1.00	74	87	8.11	0.92	0.93
85	195	41	18	78	1.02	348	78	7.66	0.98	1.00
86	151	55	343	81	1.01	313	81	10.69	0.70	0.71
87	202	48	23	70	1.06	353	70	7.55	0.99	1.06
88	161	55	349	75	1.04	319	75	9.91	0.76	0.78
89	198	48	19	70	1.06	349	70	7.64	0.98	1.05
90	196	45	18	73	1.05	348	73	7.66	0.98	1.02
91	177	52	2	71	1.06	332	71	8.48	0.88	0.94
92	239	69	63	59	1.17	33	59	8.94	0.84	0.98
93	195	48	17	71	1.06	347	71	7.69	0.98	1.03
94	110	63	137	74	1.04	107	74	8.16	0.92	0.96
95	172	58	355	68	1.08	325	68	9.14	0.82	0.89
96	290	79	283	89	1.00	253	89	8.15	0.92	0.92
97	283	78	99	85	1.00	69	85	8.35	0.90	0.90
98	287	84	106	86	1.00	76	86	8.04	0.93	0.94
99	158	52	349	79	1.02	319	79	9.91	0.76	0.77
100	168	54	354	73	1.05	324	73	9.25	0.81	0.85
101	165	57	350	72	1.05	320	72	9.76	0.77	0.81
102	213	64	34	55	1.22	4	55	7.52	1.00	1.22
103	174	41	5	82	1.01	335	82	8.26	0.91	0.92
104	229	57	47	65	1.10	17	65	7.84	0.96	1.06
105	248	78	77	58	1.18	47	58	10.66	0.70	0.83
106	37	50	90	1.57		20	90	7.98	0.94	0.00
107	122	82	305	88	1.00	275	88	7.83	0.96	0.96
108	166	48	357	79	1.02	327	79	8.92	0.84	0.86
109	190	50	13	69	1.07	343	69	7.84	0.96	1.03
110	157	60	343	74	1.04	313	74	10.69	0.70	0.73
111	219	45	35	74	1.04	5	74	7.53	1.00	1.04
112	158	73	334	64	1.11	304	64	9.42	0.80	0.89
113	158	73	334	64	1.11	304	64	9.42	0.80	0.89
114	152	80	324	64	1.11	294	64	8.55	0.88	0.98
115	222	54	40	66	1.09	10	66	7.62	0.98	1.08
116	189	57	10	63	1.12	340	63	7.97	0.94	1.06
117	194	55	15	64	1.11	345	64	7.76	0.97	1.08
118	172	66	350	61	1.14	320	61	9.76	0.77	0.88
119	150	74	328	69	1.07	298	69	8.85	0.85	0.91
120	148	75	325	70	1.06	295	70	8.62	0.87	0.93
121	182	74	355	49	1.33	325	49	9.14	0.82	1.09
122	197	57	17	61	1.14	347	61	7.69	0.98	1.11
123	171	63	351	64	1.11	321	64	9.63	0.78	0.87

Appendix B. Location 4 (continued)

Fracture ID	Strike	Dip	Rotation to horizontal		Weighting factor (f_1)	Rotation about Vertical Axis		obs. length	Weight factor (f_2)	f_1*f_2
			Strike	Dip		Strike	Dip			
124	192	63	11	56	1.21	341	56	7.92	0.95	1.14
125	216	68	38	51	1.29	8	51	7.57	0.99	1.27
126	301	73	282	77	1.03	252	77	8.20	0.92	0.94
127	199	54	20	64	1.11	350	64	7.61	0.99	1.10
128	171	55	356	71	1.06	326	71	9.03	0.83	0.88
129	172	54	357	71	1.06	327	71	8.92	0.84	0.89
130	120	77	129	88	1.00	99	88	7.90	0.95	0.95
131	207	49	27	69	1.07	357	69	7.51	1.00	1.07
132	208	64	28	54	1.24	358	54	7.50	1.00	1.24
133	189	55	11	65	1.10	341	65	7.92	0.95	1.04
134	284	89	109	81	1.01	79	81	7.94	0.94	0.96
135	286	88	109	83	1.01	79	83	7.94	0.94	0.95
136	291	89	112	87	1.00	82	87	7.88	0.95	0.95
137	222	62	43	58	1.18	13	58	7.70	0.97	1.15
138	193	51	15	68	1.08	345	68	7.76	0.97	1.04
139	183	57	5	64	1.11	335	64	8.26	0.91	1.01
140	172	45	2	79	1.02	332	79	8.48	0.88	0.90
141	171	43	2	81	1.01	332	81	8.48	0.88	0.90
142	288	85	107	86	1.00	77	86	8.00	0.94	0.94
143	288	85	107	86	1.00	77	86	8.00	0.94	0.94
144	149	69	331	73	1.05	301	73	9.11	0.82	0.86
145	180	49	5	73	1.05	335	73	8.26	0.91	0.95
146	197	58	17	60	1.15	347	60	7.69	0.98	1.13
147	238	57	54	69	1.07	24	69	8.21	0.91	0.98
148	205	49	25	69	1.07	355	69	7.53	1.00	1.07
149	172	51	359	74	1.04	329	74	8.73	0.86	0.89
150	151	57	341	80	1.02	311	80	10.36	0.72	0.74
151	212	47	30	71	1.06	0	71	7.50	1.00	1.06
152	220	62	41	58	1.18	11	58	7.64	0.98	1.16
153	199	57	19	61	1.14	349	61	7.64	0.98	1.12
154	196	46	18	72	1.05	348	72	7.66	0.98	1.03
155	283	84	104	82	1.01	74	82	8.11	0.92	0.93
156	132	63	327	89	1.00	297	89	8.76	0.86	0.86
157	204	46	24	72	1.05	354	72	7.54	0.99	1.05
158	210	49	29	69	1.07	359	69	7.50	1.00	1.07
159	212	56	32	62	1.13	2	62	7.50	1.00	1.13
160	208	65	28	53	1.25	358	53	7.50	1.00	1.25
161	124	89	300	83	1.01	270	83	7.80	0.96	0.97
162	194	59	14	60	1.15	344	60	7.80	0.96	1.11
163	284	82	103	84	1.01	73	84	8.15	0.92	0.92
164	165	56	351	73	1.05	321	73	9.63	0.78	0.81

Appendix B. Location 4 (continued)

Fracture ID	Strike	Dip	Rotation to horizontal		Weighting factor (f_1)	Rotation about Vertical Axis		obs. length	Weight factor (f_2)	f_1*f_2
			Strike	Dip		Strike	Dip			
165	208	53	28	65	1.10	358	65	7.50	1.00	1.10
166	172	62	353	64	1.11	323	64	9.37	0.80	0.89
167	198	48	19	70	1.06	349	70	7.64	0.98	1.05
168	149	60	338	79	1.02	308	79	9.92	0.76	0.77
169	156	57	344	77	1.03	314	77	10.82	0.69	0.71
170	178	71	353	54	1.24	323	54	9.37	0.80	0.99
171	176	56	359	68	1.08	329	68	8.73	0.86	0.93
172	183	57	5	64	1.11	335	64	8.26	0.91	1.01
173	159	49	352	81	1.01	322	81	9.49	0.79	0.80
174	145	85	315	66	1.09	285	66	8.08	0.93	1.02
175	273	86	101	73	1.05	71	73	8.25	0.91	0.95
176	157	70	336	67	1.09	306	67	9.66	0.78	0.84
177	219	63	40	57	1.19	10	57	7.62	0.98	1.17
178	181	88	343	38	1.62	313	38	10.69	0.70	1.14
179	286	71	274	89	1.00	244	89	8.67	0.87	0.87
180	192	56	13	63	1.12	343	63	7.84	0.96	1.07
181	175	57	358	67	1.09	328	67	8.83	0.85	0.92
182	290	86	109	87	1.00	79	87	7.94	0.94	0.95
183	84	90	99	63	1.12	69	63	8.35	0.90	1.01
184	22	59	245	4	14.34	215	4	9.17	0.82	11.73
185	183	44	9	77	1.03	339	77	8.02	0.93	0.96
186	286	76	98	89	1.00	68	89	8.41	0.89	0.89
187	281	77	97	84	1.01	67	84	8.47	0.89	0.89
188	281	78	98	84	1.01	68	84	8.41	0.89	0.90
189	191	71	7	49	1.33	337	49	8.14	0.92	1.22
190	197	68	15	51	1.29	345	51	7.76	0.97	1.24
191	179	51	4	71	1.06	334	71	8.33	0.90	0.95
192	167	48	357	78	1.02	327	78	8.92	0.84	0.86
193	173	49	1	75	1.04	331	75	8.56	0.88	0.91
194	177	63	356	61	1.14	326	61	9.03	0.83	0.95
195	147	63	334	78	1.02	304	78	9.42	0.80	0.81
196	152	62	338	76	1.03	308	76	9.92	0.76	0.78
197	178	56	1	67	1.09	331	67	8.56	0.88	0.95
198	153	60	340	76	1.03	310	76	10.20	0.74	0.76
199	152	75	328	67	1.09	298	67	8.85	0.85	0.92
200	168	65	348	64	1.11	318	64	10.06	0.75	0.83
201	174	53	359	71	1.06	329	71	8.73	0.86	0.91
202	176	60	357	64	1.11	327	64	8.92	0.84	0.94
203	289	72	276	87	1.00	246	87	8.53	0.88	0.88
204	189	58	10	62	1.13	340	62	7.97	0.94	1.07
205	250	73	75	63	1.12	45	63	10.61	0.71	0.79

Appendix B. Location 5

Fracture ID	Strike	Dip	Rotation to horizontal		Weighting factor (f_1)	Rotation about Vertical Axis		obs. length	Weight factor (f_2)	f_1*f_2
			Strike	Dip		Strike	Dip			
1	**302**	**90**	147	41	1.52	151	90	8.35	1.76	2.68
2	332	90	167	66	1.09	181	90	7.30	2.01	2.20
3	344	84	167	80	1.02	193	84	7.49	1.96	1.99
4	347	77	162	86	1.00	196	77	7.59	1.93	1.94
5	348	87	171	82	1.01	197	87	7.63	1.92	1.94
6	352	86	172	86	1.00	201	86	7.82	1.88	1.88
7	353	52	321	79	1.02	202	52	7.87	1.87	1.90
8	354	42	312	75	1.04	203	42	7.93	1.85	1.92
9	357	51	321	76	1.03	206	51	8.12	1.81	1.86
10	0	70	340	80	1.02	209	70	8.35	1.76	1.79
11	1	68	339	79	1.02	210	68	8.43	1.74	1.78
12	3	78	349	81	1.01	212	78	8.61	1.71	1.73
13	4	70	342	77	1.03	213	70	8.70	1.69	1.73
14	7	50	323	68	1.08	216	50	9.02	1.63	1.76
15	8	70	343	73	1.05	217	70	9.14	1.61	1.68
16	9	59	332	69	1.07	218	59	9.26	1.59	1.70
17	10	69	343	71	1.06	219	69	9.39	1.56	1.65
18	12	47	320	64	1.11	221	47	9.67	1.52	1.69
19	12	32	303	62	1.13	221	32	9.67	1.52	1.72
20	13	78	353	72	1.05	222	78	9.82	1.50	1.57
21	14	57	331	64	1.11	223	57	9.98	1.47	1.64
22	16	67	343	65	1.10	225	67	10.32	1.42	1.57
23	16	86	2	72	1.05	225	86	10.32	1.42	1.50
24	18	57	332	61	1.14	227	57	10.70	1.37	1.57
25	19	75	352	65	1.10	228	75	10.91	1.35	1.49
26	22	75	353	62	1.13	231	75	11.60	1.27	1.43
27	22	54	329	57	1.19	231	54	11.60	1.27	1.51
28	23	51	326	56	1.21	232	51	11.86	1.24	1.49
29	25	50	325	55	1.22	234	50	12.42	1.18	1.44
30	25	49	324	55	1.22	234	49	12.42	1.18	1.44
31	25	43	316	55	1.22	234	43	12.42	1.18	1.44
32	25	69	347	58	1.18	234	69	12.42	1.18	1.39
33	25	41	314	55	1.22	234	41	12.42	1.18	1.44
34	26	46	320	54	1.24	235	46	12.73	1.15	1.43
35	26	90	10	65	1.10	235	90	12.73	1.15	1.27
36	27	57	334	54	1.24	236	57	13.05	1.13	1.39
37	29	65	344	53	1.25	238	65	13.78	1.07	1.34
38	29	45	319	52	1.27	238	45	13.78	1.07	1.35
39	29	37	309	53	1.25	238	37	13.78	1.07	1.34
40	32	54	330	49	1.33	241	54	14.56	1.01	1.34
41	33	53	329	48	1.35	242	53	14.42	1.02	1.37
42	33	38	309	50	1.31	242	38	14.42	1.02	1.33
43	33	58	336	49	1.33	242	58	14.42	1.02	1.35

Appendix B. Location 5 (continued)

Fracture ID	Strike	Dip	Rotation to horizontal		Weighting factor (f_1)	Rotation about Vertical Axis		obs. length	Weight factor (f_2)	f_1*f_2
			Strike	Dip		Strike	Dip			
44	33	53	329	48	1.35	242	53	14.42	1.02	1.37
45	34	58	336	48	1.35	243	58	14.29	1.03	1.38
46	34	41	313	49	1.33	243	41	14.29	1.03	1.36
47	35	53	329	47	1.37	244	53	14.17	1.04	1.42
48	35	42	314	48	1.35	244	42	14.17	1.04	1.40
49	35	62	341	47	1.37	244	62	14.17	1.04	1.42
50	36	48	322	46	1.39	245	48	14.05	1.05	1.45
51	37	59	337	45	1.41	246	59	13.94	1.05	1.49
52	37	40	311	47	1.37	246	40	13.94	1.05	1.44
53	38	71	354	47	1.37	247	71	13.84	1.06	1.45
54	38	57	335	44	1.44	247	57	13.84	1.06	1.53
55	39	60	339	44	1.44	248	60	13.74	1.07	1.54
56	40	50	324	43	1.47	249	50	13.64	1.08	1.58
57	41	48	321	43	1.47	250	48	13.56	1.08	1.59
58	41	42	313	44	1.44	250	42	13.56	1.08	1.56
59	42	35	303	46	1.39	251	35	13.47	1.09	1.52
60	42	45	317	43	1.47	251	45	13.47	1.09	1.60
61	44	59	338	39	1.59	253	59	13.32	1.10	1.75
62	44	29	295	48	1.35	253	29	13.32	1.10	1.48
63	44	84	14	46	1.39	253	84	13.32	1.10	1.53
64	44	47	319	41	1.52	253	47	13.32	1.10	1.68
65	44	75	2	42	1.49	253	75	13.32	1.10	1.65
66	47	46	317	39	1.59	256	46	13.13	1.12	1.78
67	47	44	314	40	1.56	256	44	13.13	1.12	1.74
68	47	37	304	42	1.49	256	37	13.13	1.12	1.67
69	48	41	309	40	1.56	257	41	13.08	1.12	1.75
70	48	83	15	42	1.49	257	83	13.08	1.12	1.68
71	48	48	320	38	1.62	257	48	13.08	1.12	1.82
72	50	49	320	36	1.70	259	49	12.98	1.13	1.93
73	51	47	317	36	1.70	260	47	12.94	1.14	1.93
74	52	43	310	37	1.66	261	43	12.90	1.14	1.89
75	55	44	310	34	1.79	264	44	12.82	1.15	2.05
76	57	48	315	31	1.94	266	48	12.78	1.15	2.23
77	57	49	317	31	1.94	266	49	12.78	1.15	2.23
78	59	44	307	32	1.89	268	44	12.76	1.15	2.17
79	62	39	298	34	1.79	271	39	12.75	1.15	2.06
80	62	39	298	34	1.79	271	39	12.75	1.15	2.06
81	64	51	316	25	2.37	273	51	12.77	1.15	2.72
82	65	50	313	25	2.37	274	50	12.78	1.15	2.72
83	66	46	305	27	2.20	275	46	12.80	1.15	2.53
84	68	48	306	24	2.46	277	48	12.85	1.14	2.81
85	69	42	295	28	2.13	278	42	12.88	1.14	2.43
86	69	39	292	31	1.94	278	39	12.88	1.14	2.21

Appendix B. Location 5 (continued)

Fracture ID	Strike	Dip	Rotation to horizontal		Weighting factor (f_1)	Rotation about Vertical Axis		obs. length	Weight factor (f_2)	f_1*f_2
			Strike	Dip		Strike	Dip			
87	70	56	321	19	3.07	279	56	12.91	1.14	3.49
88	72	47	299	23	2.56	281	47	12.99	1.13	2.89
89	72	34	284	34	1.79	281	34	12.99	1.13	2.02
90	74	56	315	16	3.63	283	56	13.09	1.12	4.07
91	74	41	288	27	2.20	283	41	13.09	1.12	2.47
92	75	61	332	13	4.45	284	61	13.15	1.12	4.97
93	78	43	285	24	2.46	287	43	13.34	1.10	2.71
94	78	85	60	21	2.79	287	85	13.34	1.10	3.07
95	79	59	315	11	5.24	288	59	13.42	1.09	5.74
96	79	61	324	9	6.39	288	61	13.42	1.09	7.00
97	79	52	295	16	3.63	288	52	13.42	1.09	3.97
98	79	36	278	31	1.94	288	36	13.42	1.09	2.13
99	81	49	285	18	3.24	290	49	13.58	1.08	3.50
100	81	82	64	17	3.42	290	82	13.58	1.08	3.70
101	81	45	281	22	2.67	290	45	13.58	1.08	2.89
102	82	40	277	26	2.28	291	40	13.67	1.07	2.45
103	83	53	285	14	4.13	292	53	13.76	1.07	4.41
104	84	47	277	19	3.07	293	47	13.87	1.06	3.25
105	86	65	329	2	28.65	295	65	14.08	1.04	29.89
106	86	43	271	23	2.56	295	43	14.08	1.04	2.67
107	87	86	85	20	2.92	296	86	14.20	1.03	3.02
108	87	35	269	31	1.94	296	35	14.20	1.03	2.01
109	87	39	269	27	2.20	296	39	14.20	1.03	2.28
110	87	31	269	35	1.74	296	31	14.20	1.03	1.80
111	87	58	274	8	7.19	296	58	14.20	1.03	7.43
112	87	48	270	18	3.24	296	48	14.20	1.03	3.35
113	88	44	268	22	2.67	297	44	14.33	1.03	2.74
114	88	62	268	4	14.34	297	62	14.33	1.03	14.70
115	89	71	99	5	11.47	298	71	14.46	1.02	11.66
116	89	37	267	29	2.06	298	37	14.46	1.02	2.10
117	91	58	250	8	7.19	300	58	7.30	2.01	14.46
118	91	44	262	22	2.67	300	44	7.30	2.01	5.37
119	91	44	262	22	2.67	300	44	7.30	2.01	5.37
120	93	82	105	17	3.42	302	82	13.71	1.07	3.67
121	93	52	252	15	3.86	302	52	13.71	1.07	4.14
122	97	46	250	21	2.79	306	46	12.37	1.19	3.31
123	97	49	246	19	3.07	306	49	12.37	1.19	3.65
124	99	52	237	17	3.42	308	52	11.81	1.24	4.25
125	101	57	219	15	3.86	310	57	11.31	1.30	5.02
126	101	37	253	31	1.94	310	37	11.31	1.30	2.52
127	105	43	242	27	2.20	314	43	10.47	1.40	3.09
128	106	43	240	27	2.20	315	43	10.29	1.43	3.14
129	107	53	221	21	2.79	316	53	10.12	1.45	4.05

Appendix B. Location 5 (continued)

Fracture ID	Strike	Dip	Rotation to horizontal		Weighting factor (f_1)	Rotation about Vertical Axis		obs. length	Weight factor (f_2)	$f_1 * f_2$
			Strike	Dip		Strike	Dip			
130	108	30	252	39	1.59	317	30	9.95	1.48	2.35
131	108	43	238	28	2.13	317	43	9.95	1.48	3.14
132	112	25	254	44	1.44	321	25	9.37	1.57	2.26
133	113	58	204	23	2.56	322	58	9.24	1.59	4.07
134	114	57	205	24	2.46	323	57	9.12	1.61	3.96
135	115	71	172	26	2.28	324	71	9.00	1.63	3.72
136	115	32	246	39	1.59	324	32	9.00	1.63	2.59
137	117	53	212	28	2.13	326	53	8.79	1.67	3.56
138	117	52	214	28	2.13	326	52	8.79	1.67	3.56
139	117	57	204	27	2.20	326	57	8.79	1.67	3.68
140	119	59	199	28	2.13	328	59	8.59	1.71	3.64
141	119	69	178	29	2.06	328	69	8.59	1.71	3.53
142	120	46	223	33	1.84	329	46	8.50	1.73	3.17
143	121	61	195	30	2.00	330	61	8.41	1.75	3.49
144	122	34	239	40	1.56	331	34	8.33	1.76	2.74
145	122	38	234	38	1.62	331	38	8.33	1.76	2.86
146	123	45	223	35	1.74	332	45	8.25	1.78	3.10
147	126	31	241	44	1.44	335	31	8.04	1.83	2.63
148	126	67	184	35	1.74	335	67	8.04	1.83	3.18
149	126	53	209	35	1.74	335	53	8.04	1.83	3.18
150	129	54	207	37	1.66	338	54	7.86	1.87	3.10
151	129	40	228	41	1.52	338	40	7.86	1.87	2.85
152	129	41	227	41	1.52	338	41	7.86	1.87	2.85
153	132	38	230	44	1.44	341	38	7.71	1.90	2.74
154	132	62	194	40	1.56	341	62	7.71	1.90	2.96
155	136	62	194	43	1.47	345	62	7.55	1.95	2.85
156	137	40	225	46	1.39	346	40	7.52	1.95	2.72
157	145	59	199	51	1.29	354	59	7.34	2.00	2.58
158	145	55	205	50	1.31	354	55	7.34	2.00	2.61
159	146	67	189	53	1.25	355	67	7.33	2.01	2.51
160	146	33	233	53	1.25	355	33	7.33	2.01	2.51
161	147	61	197	53	1.25	356	61	7.32	2.01	2.51
162	147	44	219	52	1.27	356	44	7.32	2.01	2.55
163	147	68	189	54	1.24	356	68	7.32	2.01	2.48
164	147	60	198	52	1.27	356	60	7.32	2.01	2.55
165	148	73	183	56	1.21	357	73	7.31	2.01	2.42
166	148	53	207	52	1.27	357	53	7.31	2.01	2.55
167	153	62	197	58	1.18	2	62	7.30	2.01	2.37
168	154	70	188	61	1.14	3	70	7.31	2.01	2.30
169	155	71	188	62	1.13	4	71	7.32	2.01	2.27
170	157	51	210	59	1.17	6	51	7.34	2.00	2.33
171	158	58	203	61	1.14	7	58	7.35	2.00	2.28
172	158	62	198	62	1.13	7	62	7.35	2.00	2.26

Appendix B. Location 5 (continued)

Fracture ID	Strike	Dip	Rotation to horizontal		Weighting factor (f_1)	Rotation about Vertical Axis		obs. length	Weight factor (f_2)	f_1*f_2
			Strike	Dip		Strike	Dip			
173	158	47	215	60	1.15	7	47	7.35	2.00	2.31
174	160	67	193	65	1.10	9	67	7.39	1.99	2.19
175	161	58	203	64	1.11	10	58	7.41	1.98	2.20
176	162	73	188	69	1.07	11	73	7.44	1.98	2.12
177	162	51	211	63	1.12	11	51	7.44	1.98	2.22
178	163	79	182	72	1.05	12	79	7.46	1.97	2.07
179	163	79	182	72	1.05	12	79	7.46	1.97	2.07
180	166	53	210	67	1.09	15	53	7.56	1.94	2.11
181	168	31	234	65	1.10	17	31	7.63	1.92	2.12
182	168	75	188	75	1.04	17	75	7.63	1.92	1.99
183	168	77	186	76	1.03	17	77	7.63	1.92	1.98
184	168	44	220	66	1.09	17	44	7.63	1.92	2.11
185	168	44	220	66	1.09	17	44	7.63	1.92	2.11
186	169	50	213	68	1.08	18	50	7.68	1.91	2.06
187	169	81	183	78	1.02	18	81	7.68	1.91	1.96
188	172	80	185	81	1.01	21	80	7.82	1.88	1.90
189	172	58	206	73	1.05	21	58	7.82	1.88	1.96
190	172	82	183	81	1.01	21	82	7.82	1.88	1.90
191	174	59	206	75	1.04	23	59	7.93	1.85	1.92
192	177	85	182	87	1.00	26	85	8.12	1.81	1.81
193	181	76	192	87	1.00	30	76	8.43	1.74	1.75
194	181	76	192	87	1.00	30	76	8.43	1.74	1.75
195	181	76	192	87	1.00	30	76	8.43	1.74	1.75
196	181	83	186	90	1.00	30	83	8.43	1.74	1.74
197	186	84	7	85	1.00	35	84	8.91	1.65	1.65
198	187	49	219	81	1.01	36	49	9.02	1.63	1.65
199	188	89	3	81	1.01	37	89	9.14	1.61	1.63
200	189	89	3	80	1.02	38	89	9.26	1.59	1.61
201	193	86	8	78	1.02	42	86	9.82	1.50	1.53
202	206	88	12	66	1.09	55	88	12.73	1.15	1.26
203	213	41	55	88	1.00	62	41	14.43	1.02	1.02
204	217	79	27	61	1.14	66	79	13.95	1.05	1.20
205	227	45	60	78	1.02	76	45	13.14	1.12	1.14